BIOGEOCHEMICAL DYNAMICS IN POROUS MEDIA:

FORMULATING MICROBIAL METABOLISM IN REACTION TRANSPORT MODELS

by

ERIC LEE KING

(Under the Direction of Christof Meile)

ABSTRACT

The goal of this work is to investigate biogeochemical dynamics in porous media, including ways to formulate microbial metabolism and its implementation into reaction transport models.

First, elemental cycling in a contaminated groundwater setting is assessed using model descriptions that differ in the range of reactions taken into account and in whether microbial population dynamics are considered. Results from simulations using different reaction networks show that a relatively simple network can provide an accurate prediction of the observed distribution of dissolved substances in a contaminant plume. However, depending on the complexity of the reaction network used, distinct differences can exist in individual process rates affecting these pools. When dynamics of microbial functional groups are accounted for, our simulations show the importance of the interplay between reaction energetics and nutrient limitations.

Microbial activity is also investigated in a freshwater marsh, and a set of reactions is developed describing the hydrolysis and fermentation of organic matter and terminal metabolic processes. Rates of reactions involved in organic matter breakdown were quantified with two

complimentary approaches. Since the two approaches rely on different types of data, they allow for independent methods to determine process rates in the sediment. Results show that the methodologies are consistent in some predicted rates but differ significantly in others, highlighting the importance of the description of reaction kinetics used for organic matter breakdown.

Explicit formulations of microbial metabolism and its implementation in reaction transport models were also investigated. A kinetic representation of *Geobacter sulfurreducens* central metabolism was developed which successfully reproduced measured growth efficiencies with iron as terminal electron acceptor over a wide range of extracellular acetate concentrations.

Analysis of experimentally validated *in silico* cell models were also utilized to predict phenotypic plasticity. When environmental conditions vary, an organism adjusts its enzymatic machinery. Results show the potential importance of investigating multiple phenotypes for an organism, not only including those that are optimal under a set of environmental conditions, but also those that may be slightly less efficient under static settings. These can be better adapted to settings in which the physic-chemical environment the microbe experiences fluctuates, requiring adaptation of its metabolic machinery.

INDEX WORDS: Reactive transport, Flux balance analysis, Elementary flux mode analysis, Kinetic cell model, *Geobacter sulfurreducens*, RTM, FBA, EFMA, EMFA, Pore scale heterogeneity, Microbial population dynamics

BIOGEOCHEMICAL DYNAMICS IN POROUS MEDIA:

FORMULATING MICROBIAL METABOLISM IN REACTION TRANSPORT MODELS

by

ERIC KING

B.S., The University of Illinois at Urbana-Champaign, 2004

M.S., Georgia College and State University, 2006

A Dissertation Submitted to the Graduate Faculty of The University of Georgia in Partial Fulfillment of the Requirements for the Degree

DOCTOR OF PHILOSOPHY

ATHENS, GEORGIA

2013

BIOGEOCHEMICAL DYNAMICS IN POROUS MEDIA:

FORMULATING MICROBIAL METABOLISM IN REACTION TRANSPORT MODELS

by

ERIC KING

Major Professor:	Christof Meile
Committee:	Samantha Joye Mary Ann Moran Adrian Burd Andrew Sornborger

Electronic Version Approved:

Maureen Grasso
Dean of the Graduate School
The University of Georgia
August 2013

DEDICATION

To Terry King, a whale of a mom.

ACKNOWLEDGEMENTS

I, first, would like to thank my advisor, Christof Meile, for all of the help he has provided me over the years. His guidance has been instrumental to my success. I would also like to thank my committee, for providing assistance and direction for my work over the years.

I also acknowledge Sarah, shade of my heart.

I am thankful to Wei-Jen Huang for the walking and discussions about the little TV. Also, thanks for offering to buy Sarah and I a marriage certificate.

I would like to apologize to Grandma for not being able to write her prescriptions.

To Hendrix, the best cat ever.

To Drs. Kate and Wei-jen, without whom grad school would have been much less fun.

To Dustin, I feel like this is our Ph.D. Our combined efforts on the N64 SC2 was instrumental for our success.

TABLE OF CONTENTS

Page

APPENDICES

LIST OF TABLES

Page

LIST OF FIGURES

Page

CHAPTER 1

INTRODUCTION AND LITERATURE REVIEW

The role of microbes in porous media

Microbially meditated reactions drive all major biogeochemical cycles on Earth (Falkowski et al., 2008), and are key to a range of issues ranging from antibiotic resistance (Mah, 2012) to alternative energy production (Rabaey et al., 2003), bioremediation (Wall and Krumholz, 2006) and global climate change (Bardgett et al., 2008). Thus, understanding their metabolic functioning, as well as their adaptations to physico-chemical changes in their surroundings and feedbacks between microbes and their environments are central research themes in a wide range of fields.

Modeling biogeochemical dynamics

Many studies of elemental cycling in porous media either focus directly or indirectly on the breakdown of organic compounds and the associated use of electron acceptors. This is based upon the central role that organics play as energy sources for subsurface microbial life. Organic matter mineralization reflects the fermentation and hydrolysis of high molecular weight compounds producing low molecular weight substances such as acetate and other volatile fatty acids as well as H_2, which then gets respired through terminal metabolism, consuming electron acceptors such as O_2, nitrate, metal oxides and sulfate (Jakobsen et al., 1998; Lovley and Goodwin, 1988).

To better understand elemental cycling and the persistence and fates of nutrients, as well as contaminants, in groundwater settings, knowledge of the transport processes and biogeochemical reactions is needed. Reactive transport models are often employed for this purpose. They are based on mass balance equations, and for a single fluid phase, the governing equation is of the form (e.g. Miller et al., 1998):

$$\frac{\partial}{\partial t}(\theta \rho c_i) = -\nabla \cdot (j + \mathbf{v}\theta \rho c_i) + \sum R \qquad (1)$$

where θ is fluid volume fraction, ρ is density, c_i is mass fraction of entity i, $\mathbf{v}$ is the advection velocity vector, ΣR is the net impact of reactions R, and j denotes non-advective transport fluxes, which are typically described as a diffusive term with a diffusion tensor $\mathbf{D}$ so that $j = -\theta \rho \mathbf{D} \nabla c$.

The evolution of reactive transport modeling to elucidate the dynamics of elemental cycling has involved an increase in the complexity of reaction descriptions and formulations. For example, McNab and Narasimhan (1994; 1995) developed a model to simulate the attenuation and breakdown of petroleum hydrocarbons in an aquifer, employing a partial equilibrium approach, while Jakobsen and Postma (1999) used this approach to study iron oxide reduction, sulfate reduction, and methanogenesis in a shallow aquifer. Mayer et al. (2001) presented a fully kinetic model to describe contaminant dynamics along flow lines in a contaminant plume over an ~50 year period utilizing reactions involved in the degradation of phenol coupled to terminal electron accepting processes. Emphasizing the importance of a comprehensive reaction network, a fully kinetic model was developed by Hunter et al. (1998) that included mineral precipitation and a suite of secondary reactions describing the reoxidation of reduced metabolites produced in the breakdown of organic matter in an aquifer, similar to the work of Boudreau (1996), Soetaert et al. (1996), and Van Cappellen and Wang (1996) on early diagenesis in marine sediments. More recent studies have also taken into account thermodynamic constraints on both abiotic and

microbially mediated reactions or focused on improving representations of microbial activity. For example, Jakobsen and Cold (2007) implemented energy constraints on reactions in a sandy aquifer while Jin and Bethke (2003), based on the work of Boudart (1976), developed a reaction rate expression which accounts for the energy available in the microbe's environment through a dependency on the Gibbs free energy of reaction. Numerous studies have quantified the effect of pore scale substrate heterogeneity on reaction rates in reactive flows in soil columns (e.g. Gramling et al., 2002; Raje and Kapoor, 2000) and at stationary reaction fronts (e.g. Meile and Tuncay, 2006), or on mineral dissolution under a variety of environmental conditions (e.g. Li et al., 2006; Li et al., 2008). Also, Jakobsen (2007) found that the co-occurance of sulfate reduction and methanogenesis was possible in the presence of anoxic microniches formed in the presence of fast organic matter decomposition, and Sochaczewski et al. (2008) describes sulfide production in organic matter aggregates of greater than 1 mm diameter within the oxic top cm of sediment.

Formulating a model of microbial metabolism

To predict the feedbacks between microbes and their environments, knowledge on how bacteria affect their surroundings at the cell and process level is beneficial. However, a problem seen in many reactive transport models is that microbes are treated in a very rudimentary fashion. Even though they mediate a large part of the biogeochemical processes occurring, the details of microbial metabolism are generally not resolved explicitly. With the recent developments in genetics and microbial ecology, knowledge of microbial processes have been elucidated, which can be used to develop cell based models.

To predict how bacteria regulate their activity and grow *in situ*, it is necessary to quantitatively understand the complex and dynamic interactions between the numerous concurrent biogeochemical processes involved, which requires the use of mathematical models. While subsurface reactive transport models generally contain a comparatively sound description of the physical transport processes (Bear, 1972; Rockhold et al., 2004), they often do not explicitly account for the dynamics of microbial populations that are responsible for the majority of biogeochemical processes (Hunter et al., 1998; Watson et al., 2003). When included, microbes are typically represented as functional groups, with growth dynamics depending linearly on substrate availability or following Monod kinetics (Mauclaire et al., 2003; Seki et al., 2004; Thullner et al., 2007), an approach that has been successful in describing geochemical contaminant plume dynamics (Brun et al., 2002). However, lacking a realistic representation of microbial metabolism, such models are limited in their capability of reflecting microbial dynamics and forecasting the response to changing environmental conditions, which restricts their predictive power at the macro-scale and usefulness, for example, in the assessment of conditions that optimize *in situ* bioremediation (Lovley, 2003).

Genome sequencing has led to the characterization of cellular metabolic networks and to the development of mathematical models at the cell scale (Stelling, 2004), ranging from descriptions of network topology (Jeong et al., 2000; Tong et al., 2004) to constraint-based models for different organisms (Forster et al., 2003; Reed et al., 2003; Stelling et al., 2002) and fully kinetic approaches (e.g. Bakker et al., 1997; Navid and Ortoleva, 2004; Weitzke and Ortoleva, 2003). Integration of such models of environmentally important groups of bacteria in reaction-transport simulations would clearly benefit forecasting biogeochemical responses to changing macroscopic conditions.

Structure and purpose of dissertation

The purpose of this study is to investigate biogeochemical dynamics in porous media, including ways to formulate microbial metabolism and its implementation into reaction transport models. One application of reaction transport models is to simulate contaminated groundwater settings, where microbes play a role through their application in bioremediation efforts. With ~30% of the global freshwater pool residing in groundwater (Gleick, 1996), its quality is of great importance. Therefore in Chapter 2, models that structurally differ in the way reactions and microbes are taken into account, which allows for a determination of the importance of accounting for microbial population dynamics, are investigated in a contaminated groundwater setting. In addition, the impact of factors that may limit the applicability of reaction-transport models in low-temperature subsurface environments is assessed. These include pore scale heterogeneity in substrate distribution and its effect on microbial processes and the impact of the scope of the reaction network considered on predicted metabolite distributions and process dynamics in a reactive transport model describing the breakdown of a phenolic plume.

In Chapter 3, to better elucidate microbially mediated carbon cycling in anoxic sediments, process rates detailing organic matter breakdown are parameterized and determined. These microbial processes can influence global climate change, such as through the production of methane, which has seen its atmospheric concentration increasing (Canfield et al., 2005). Though present at a concentration approximately 200 times less than carbon dioxide, methane serves as an important greenhouse gas due to it having approximately 25 times the radiative forcing of CO_2 (Lelieveld et al., 1998). Methane can be produced through terminal metabolic processes coupled to the breakdown of organic matter in anoxic sediments. Freshwater wetlands are therefore an important methane source, and have been estimated to account for ~20% of

global emissions (Aselmann and Crutzen, 1989). Due to its potentially significant impact on climate change, detailed information on methane cycling, including an investigation into the biological controls and processes affecting its production in freshwater systems is needed. Therefore, a model representing organic matter breakdown is formulated with data taken from a detailed analysis of benthic anaerobic organic carbon breakdown carried out on sediments collected in freshwater habitats in Georgia. The data obtained contain a wealth of information on the step-wise breakdown of organic matter at the process level, including a time series of pore water constituents in sediment slurries and radiotracer incubations using methanogenic precursors, used to delineate the process rates involved in anaerobic metabolism.

To address the need for comprehensive descriptions of microbial dynamics, cell-scale models of *Geobacter sulfurreducens,* an organism potentially useful in contaminated groundwater settings, are developed in chapters 4 and 5. *Geobacteracea*, a γ-proteobacteria, constitute an abundant and environmentally important group in both pristine and contaminated sediment environments (Lovley, 2003). *Geobacter* species are metabolically diverse and can grow with numerous electron donors and acceptors, including acetate or H_2 and Fe(III), fumarate, or malate, respectively (Caccavo et al., 1994; Lovley, 1993). *Geobacter* shape biogeochemical cycling directly through their metabolic activity, e.g. such as via the effect of iron (hydro)oxide reduction on the motility of sorbed trace metals and on pH. They have been shown to be enriched when Fe(III) reduction was promoted in a petroleum-contaminated sandy aquifer (Snoeyenbos-West et al., 2000) and can mediate the reduction of U(VI) to U(IV) (Lovley et al., 1991), converting the soluble form to the insoluble form and effectively removing the uranium from groundwater (Wilkins et al., 2006).

In Chapter 4, a kinetic reaction-mechanism based model for *Geobacter sulfurreducens* is developed to elucidate the feedbacks between environmental conditions, cellular processes, and metabolite concentrations. Knowledge of the enzymatic reactions occurring within the cell is utilized to develop a kinetic based model of the organism that is applied to a simulation of a subsurface contaminant plume. In addition, growth efficiencies are quantified as well as the sensitivity of model results to the parameterization of the enzymatic reactions of the TCA cycle and gluconeogenesis considered. Finally, coupling between cell metabolic expressions and macroscopic reactive transport models is used to assess the potential and limits of models that parameterize microscopic intracellular processes.

In Chapter 5, phenotypic plasticity in microbes is studied in environmental settings where conditions may fluctuate over time. Specifically one can investigate the importance of near optimal phenotypes, or those metabolic networks that do not e.g. maximize growth, but can become relevant in variable environmental conditions where minimization of the reorganization of the metabolic machinery is beneficial. To this end, elementary flux mode analysis was used to develop a model of *Geobacter*. Unlike the commonly used flux balance analysis, which determines one realized phenotype through optimization of a goal function, e.g., maximizing cellular growth or ATP production, elementary flux mode analysis returns all feasible steady state realizations of the intracellular reaction network. These phenotypes were investigated to determine metabolic networks that were most optimal for growth while minimizing the transition cost occurred when adjusting the metabolic machinery in response to changing environmental conditions.

Finally, in Chapter 6, a summary of the results of these chapters is provided.

References

Aselmann, I. and Crutzen, P.J., 1989. Global Distribution of Natural Fresh-Water Wetlands and Rice Paddies, Their Net Primary Productivity, Seasonality and Possible Methane Emissions. Journal of Atmospheric Chemistry, 8(4): 307-358.

Bakker, B.M., Michels, P.A.M., Opperdoes, F.R. and Westerhoff, H.V., 1997. Glycolysis in bloodstream form Trypanosoma brucei can be understood in terms of the kinetics of the glycolytic enzymes. J. Biol. Chem., 272(6): 3207-3215.

Bardgett, R.D., Freeman, C. and Ostle, N.J., 2008. Microbial contributions to climate change through carbon cycle feedbacks. Isme Journal, 2(8): 805-814.

Bear, J., 1972. Dynamics of fluids in porous media. Environmental Science Series. American Elsevier Publishing Company, Inc., New York, 764 pp.

Boudart, M., 1976. Consistency between Kinetics and Thermodynamics. Journal of Physical Chemistry, 80(26): 2869-2870.

Boudreau, B.P., 1996. A method-of-lines code for carbon and nutrient diagenesis in aquatic sediments. Computers Geosci., 22(5): 479-496.

Brun, A., Engesgaard, P., Christensen, T.H. and Rosbjerg, D., 2002. Modeling of transport and biogeochemical processes in pollution plumes: Vejen landfill, Denmark. J. Hydrol., 256: 228-247.

Caccavo, F.J. et al., 1994. Geobacter sulfurreducens sp. nov., a hydrogen- and acetate-oxidizing dissimilatory metal-reducing microorganism. Appl. Environ. Microbiol., 60(10): 3752-3759.

Canfield, D.E., Kristensen, E. and Thamdrup, B., 2005. Aquatic geomicrobiology. Elsevier Academic Press, 640 pp.

Falkowski, P.G., Fenchel, T. and Delong, E.F., 2008. The microbial engines that drive Earth's biogeochemical cycles. Science, 320(5879): 1034-1039.

Forster, J., Famili, I., Fu, P., Palsson, B.O. and Nielsen, J., 2003. Genome-scale reconstruction of the Saccharomyces cerevisiae metabolic network. Genome Res., 13(2): 244-253.

Gleick, P.H., 1996. Water resources. In: S.H. Schneider (Editor), Encyclopedia of Climate and Weather. Oxford University Press, New York, pp. 817-823.

Gramling, C.M., Harvey, C.F. and Meigs, L.C., 2002. Reactive transport in porous media: A comparison of model prediction with laboratory visualization. Environ. Sci. Technol., 36(11): 2508-2514.

Hunter, K.S., Wang, Y. and Van Cappellen, P., 1998. Kinetic modeling of microbially-driven redox chemistry in subsurface environments: coupling transport, microbial metabolism and geochemistry. J. Hydrol., 209: 53-58.

Jakobsen, R., 2007. Redox microniches in groundwater: A model study on the geometric and kinetic conditions required for concomitant Fe oxide reduction, sulfate reduction, and methanogenesis. Water Resources Research, 43, W12S12.

Jakobsen, R. et al., 1998. H-2 concentrations in a landfill leachate plume (Grindsted, Denmark): In situ energetics of terminal electron acceptor processes. Environmental Science & Technology, 32(14): 2142-2148.

Jakobsen, R. and Cold, L., 2007. Geochemistry at the sulfate reduction-methanogenesis transition zone in an anoxic aquifer - A partial equilibrium interpretation using 2D reactive transport modeling. Geochimica Et Cosmochimica Acta, 71(8): 1949-1966.

Jakobsen, R. and Postma, D., 1999. Redox zoning, rates of sulfate reduction and interactions with Fe-reduction and methanogenesis in a shallow sandy aquifer, Romo, Denmark. Geochimica Et Cosmochimica Acta, 63(1): 137-151.

Jeong, H., Tombor, B., Albert, R., Oltavai, Z.N. and Barbasi, A.-L., 2000. The large-scale organization of metabolic networks. Nature, 407: 651-654.

Jin, Q. and Bethke, C.M., 2003. A new rate law describing microbial respiration. Appl. Env. Microb., 69(4): 2340-2348.

Lelieveld, J., Crutzen, P.J. and Dentener, F.J., 1998. Changing concentration, lifetime and climate forcing of atmospheric methane. Tellus Series B-Chemical and Physical Meteorology, 50(2): 128-150.

Li, L., Peters, C.A. and Celia, M.A., 2006. Upscaling geochemical reaction rates using pore-scale network modeling. Advances in Water Resources, 29(9): 1351-1370.

Li, L., Steefel, C.I. and Yang, L., 2008. Scale dependence of mineral dissolution rates within single pores and fractures. Geochimica Et Cosmochimica Acta, 72(2): 360-377.

Lovley, D.R., 1993. Dissimilatory metal reduction Annu. Rev. Microbiol., 47: 263-290.

Lovley, D.R., 2003. Cleaning up with genomics: applying molecular biology to bioremediation. Nat. Rev. Microbiol., 1: 35-44.

Lovley, D.R. and Goodwin, S., 1988. Hydrogen Concentrations as an Indicator of the Predominant Terminal Electron-Accepting Reactions in Aquatic Sediments. Geochimica Et Cosmochimica Acta, 52(12): 2993-3003.

Lovley, D.R., Phillips, E.J.P., Gorby, Y.A. and Landa, E.R., 1991. Microbial Reduction of Uranium. Nature, 350(6317): 413-416.

Mah, T.F., 2012. Biofilm-specific antibiotic resistance. Future Microbiology, 7(9): 1061-1072.

Mauclaire, L., Pelz, O., Thullner, M., Abraham, W.R. and Zeyer, J., 2003. Assimilation of toluene carbon along a bacteria-protist food chain determined by C-13-enrichment of biomarker fatty acids. J. Microbiol. Methods., 55(3): 635-649.

Mayer, K.U., Benner, S.G., Frind, E.O., Thornton, S.F. and Lerner, D.N., 2001. Reactive transport modeling of processes controlling the distribution and natural attenuation of phonlic compounds in a deep sandstonee aquifer. Journal of Contaminant Hydrology, 53: 341-368.

McNab, W.W. and Narasimhan, T.N., 1994. Modeling Reactive Transport of Organic-Compounds in Groundwater Using a Partial Redox Disequilibrium Approach. Water Resources Research, 30(9): 2619-2635.

McNab, W.W. and Narasimhan, T.N., 1995. Reactive Transport of Petroleum Hydrocarbon Constituents in a Shallow Aquifer - Modeling Geochemical Interactions between Organic and Inorganic Species. Water Resources Research, 31(8): 2027-2033.

Meile, C. and Tuncay, K., 2006. Scale dependence of reaction rates in porous media. Adv. Water Resources, 29: 62-71.

Miller, C.T. et al., 1998. Multiphase flow and transport modeling in heterogeneous porous media: challenges and approaches. Advances in Water Resources, 21(2): 77-120.

Navid, A. and Ortoleva, P.J., 2004. Simulated complex dynamics of glycolysis in the protozoan parasite Trypanosoma brucei. J. Theor. Biol., 228: 449-458.

Rabaey, K., Lissens, G., Siciliano, S.D. and Verstraete, W., 2003. A microbial fuel cell capable of converting glucose to electricity at high rate and efficiency. Biotechnology Letters, 25(18): 1531-1535.

Raje, D.S. and Kapoor, V., 2000. Experimental study of bimolecular reaction kinetics in porous media. Environ. Sci. Technol., 34(7): 1234-1239.

Reed, J.L., Vo, T.D., Schilling, C.H. and Palsson, B.O., 2003. An expanded genome-scale model of Escherichia coli K-12 (iJR904 GSM/GPR). Genome Bio., 4(9): R54.

Rockhold, M.L., Yarwood, R.R. and Selker, J.S., 2004. Coupled microbial and transport processes in soils. Vadose Zone J., 3: 368-383.

Seki, K., Thullner, M. and Baveye, P., 2004. Nutrient uptake kinetics of filamentous microorganisms: Comparison of cubic, exponential, and Monod models. Ann. Microbiol., 54(2): 181-188.

Snoeyenbos-West, O.L., Nevin, K.P., Anderson, R.T. and Lovley, D.R., 2000. Enrichment of Geobacter species in response to stimulation of Fe(III) reduction in sandy aquifer sediments. Microb. Ecol., 39: 153-167.

Sochaczewski, L., Stockdale, A., Davison, W., Tych, W. and Zhang, H., 2008. A three-dimensional reactive transport model for sediments, incorporating microniches. Environmental Chemistry, 5(3): 218-225.

Soetaert, K., Herman, P.M.J. and Middelburg, J.J., 1996. A model of early diagenetic processes from the shelf to abyssal depths. Geochim. Cosmochim. Acta, 60(6): 1019-1040.

Stelling, J., 2004. Mathematical models in microbial systems biology. Curr. Opin. Microbiol., 7(5): 513-518.

Stelling, J., Klamt, S., Bettenbrock, K., Schuster, S. and Gilles, E.D., 2002. Metabolic network structure determines key aspects of functionality and regulation. Nature, 420(6912): 190-193.

Thullner, M., Regnier, P. and Van Cappellen, P., 2007. Modeling microbially induced carbon degradation in redox-stratified subsurface environments: concepts and open questions. Geomicrobiol. J., 24(3-4): 139-155.

Tong, A.H.Y. et al., 2004. Global mapping of the yeast genetic interaction network. Science, 303(5659): 808-813.

Van Cappellen, P. and Wang, Y., 1996. Cycling of iron and manganese in surface sediments: A general theory for the coupled transport and reaction of carbon, oxygen, nitrogen, sulfur, iron and manganese. Am. J. Sci., 296: 197-243.

Wall, J.D. and Krumholz, L.R., 2006. Uranium reduction. Annual Review of Microbiology, 60: 149-166.

Watson, I.A., Oswald, S.E., Mayer, K.U., Youxian, W. and Banwart, S.A., 2003. Modeling kinetic processes controlling hydrogen and acetate concentrations in an aquifer-derived microcosm. Environ. Sci. Technol., 37: 3910-3919.

Weitzke, E.L. and Ortoleva, P.J., 2003. Simulating cellular dynamics through a coupled transcription, translation, metabolic model. Comput. Biol. Chem., 27(4-5): 469-481.

Wilkins, M.J., Livens, F.R., Vaughan, D.J. and Lloyd, J.R., 2006. The impact of Fe(III)-reducing bacteria on uranium mobility. Biogeochemistry, 78(2): 125-150.

CHAPTER 2

MODELING BIOGEOCHEMICAL DYNAMICS IN POROUS MEDIA: PRACTICAL CONSIDERATIONS OF PORE SCALE VARIABILITY, REACTION NETWORKS, AND MICROBIAL POPULATION DYNAMICS IN A SANDY AQUIFER[1]

[1] Eric Lee King, Kagan Tuncay, Peter Ortoleva, and Christof Meile. 2010. *Journal of Contaminant Hydrology*. 112:130-140. Reprinted here with permission of the publisher.

Abstract

Prediction of the fate and environmental impacts of groundwater contaminants requires the identification of relevant biogeochemical processes and necessitates the macroscopic representation of microbial activity occurring at the microscale. Using a well-studied sandy aquifer environment, we evaluate the importance of pore distribution on organic matter respiration in a porous medium environment by performing spatially explicit simulations of microbial metabolism at the sub-millimeter scale. Model results using an idealized porous medium under non-biofilm forming conditions indicate that while some heterogeneity is observed for flow rates, distributions of microbes and dissolved organic substrates remain relatively homogenous at the grain scale. At the macroscale in the same environment, we assess the impact of a comprehensive reaction network description for a phenolic contaminant plume, and compare the findings to a setting describing organic matter breakdown in a coastal marine sediment. This comparison reveals the importance of reactions recycling reduced metabolites at redox interfaces, leading to a competition for oxidants. When the spatio-temporal dynamics of microbial groups are accounted for, our simulations show the importance of the interplay between reaction energetics and nutrient limitations such as microbial nitrogen demands.

Introduction

To assess the persistence and fate of nutrients, contaminants, and pathogens in aquifers, it is necessary to understand their biogeochemical and transport behavior. Their spatio-temporal distribution depends on sorption and transport characteristics and chemical transformations, many of which are microbially mediated. Challenged by sparse observational data in subsurface environments, predictions of the fate of these substances typically rely on computational

approaches. Models that couple transport processes with reactions result in tight interactions between a multitude of chemical species. They are commonly used to quantitatively assess biogeochemical dynamics in aquifers and have provided significant insight into contaminant transport and decision making support (e.g. Cygan et al. 2007). While a comprehensive treatment of reactive transport relies on conservation of mass, momentum, and energy (Steefel et al. 2005), in practice most models are based only on mass balance equations. For a single fluid phase, the governing equations for the various constituents are of the form (e.g. Miller et al. 1998):

$$\frac{\partial}{\partial t}\left(\theta\rho c_i\right) = -\nabla\cdot\left(j + \mathbf{v}\theta\rho c_i\right) + \sum R \qquad (1)$$

where θ is fluid volume fraction, ρ is density, c_i is mass fraction of entity i, $\mathbf{v}$ is the advection velocity vector, ΣR is the net impact of reactions R, and j denotes non-advective transport fluxes, which are typically described as a diffusive term with a diffusion tensor $\mathbf{D}$ so that $j = -\theta\rho\mathbf{D}\nabla c$.

Some features in such reactive transport models can pose limits to their applicability. First, they rely on bulk properties that are averages over a representative elementary volume (REV; Zhang et al. 2000). In porous media, REVs must encompass several grains, implying that heterogeneity below that scale can be properly parameterized or has a negligible impact on reaction rate estimates (e.g. Szecsody et al. 1998, Wood et al. 2007). Second, description of transport processes via the use of a diffusion tensor assumes that non-Fickian transport is of minor importance (Hassanizadeh 1995, Levy and Berkowitz 2003). Third, use of Equation 1 implies that the reaction network can be identified and parameterized. In order to do so, a set of reactions needs to be selected to represent a system of tremendous natural complexity, involving not only transformations in solution, surface catalysis, and precipitation and dissolution of mineral phases, but also the activity and dynamics of microbial populations. Volumetric reaction rates vary with abundance, distribution, metabolic capability, and cell-specific activity of

microbial populations. The microbial community has the potential to both modify and adjust to environmental conditions through changes in community composition, alterations of activity levels, chemotactic movement and metabolic plasticity (e.g. Ginn et al. 2002, Pett-Ridge and Firestone 2005).

Due to the central role of organics as energy sources for subsurface microbial life and the importance of redox conditions for the fate of contaminants, many studies of elemental cycling in porous media either focus directly or indirectly on the breakdown of organic compounds and the associated use of electron acceptors. Organic matter mineralization can be conceptualized as fermentation and hydrolysis of high molecular weight compounds producing low molecular weight substances such as acetate and other volatile fatty acids as well as H_2, which then gets respired through terminal metabolism, consuming electron acceptors such as O_2, nitrate, metal oxides and sulfate (Lovley and Goodwin 1988, Jakobsen et al. 1998). The evolution of reactive transport modeling to elucidate the dynamics of elemental cycling has involved an increase in the complexity of the reactions. For example, McNab and Narasimhan (1994, 1995) developed a model to simulate the attenuation and breakdown of petroleum hydrocarbons in an aquifer, employing a partial equilibrium approach where fermentation controls the rate of organic matter degradation with terminal electron accepting processes occurring close to equilibrium. Jakobsen and Postma (1999) used this approach to study iron oxide reduction, sulfate reduction, and methanogenesis in a shallow aquifer. Mayer et al. (2001) presented a fully kinetic model to describe contaminant dynamics along flow lines in a contaminant plume over an ~50 year period utilizing reactions involved in the degradation of phenol coupled to terminal electron accepting processes. Emphasizing the importance of a comprehensive reaction network, Hunter et al. (1998) developed a fully kinetic model that included mineral precipitation and a suite of

secondary reactions describing the reoxidation of reduced metabolites produced in the breakdown of organic matter in an aquifer, similar to the work of Boudreau (1996), Soetaert et al. (1996), and Van Cappellen and Wang (1996) on early diagenesis in marine sediments. Recent studies have also taken into account thermodynamic constraints on both abiotic and microbially mediated reactions or focused on improving representations of microbial activity. For example, Jakobsen and Cold (2007) implemented energy constraints on reactions in a sandy aquifer while Jin and Bethke (2003), based on the work of Boudart (1976), developed a reaction rate expression which accounts for the energy available in the microbe's environment through a dependency on the Gibbs free energy of reaction. The effect of microniches—i.e. scales typically not resolved explicitly—on redox processes has been investigated (e.g., Jakobsen et al. 2007, Sochaczewski et al. 2008), and numerous studies have quantified the effect of pore scale substrate heterogeneity on reaction rates in reactive flows in soil columns (e.g., Raje and Kapoor 2000, Gramling et al. 2002), at stationary reaction fronts (e.g., Meile and Tuncay 2006), or on mineral dissolution under a variety of environmental conditions (e.g., Li et al. 2006, 2008).

In this study we assess the impact of three factors that may limit the applicability of reactive transport models in low-temperature subsurface environments: (i) pore scale heterogeneity in substrate distribution and its effect on microbial processes, (ii) impact of the scope of the reaction network used on predicted metabolite distributions and process dynamics, and (iii) role of constraints on microbial population dynamics. We address these issues using data taken from a sandstone aquifer (Sherwood aquifer, West Midlands, UK) with a phenolic contaminant plume that has been documented extensively in the literature (Thornton et al. 2001a,b, Mayer et al. 2001, Watson et al. 2005). First, we focus on flow fields and substrate availability at the grain scale. Simulations of flow and reaction are performed in a two-

dimensional representation of a porous medium taken from the Sherwood aquifer to assess if pore scale heterogeneity in substrate and biomass distributions is likely to occur under conditions that are representative for the metabolism of dissolved organic matter. Second, macroscopic reaction transport simulations are performed that extend the work of Watson et al. (2005), who modeled the contaminants originating from a coal tar distillation plant which have been penetrating into the aquifer since the early 1950s. The effect of the comprehensiveness of the reaction network is evaluated by assessing the impact of additional reoxidation reactions and mineral precipitation. The findings are then compared to the roles of these additional reactions in early diagenesis in a coastal marine sediment. Controls on microbial populations and their interactions with the geochemical environment are considered by integration of explicit descriptions of functional microbial groups into reactive transport models.

2. Methods and Applications

2.1. Pore scale model

To investigate the interplay between transport of chemicals and microbial dynamics, simulations at the pore scale were performed. The flow field is required in the mass conservation equations for chemical and biological constituents and is solved using the incompressible Navier-Stokes equations:

$$\rho\frac{\partial \mathbf{u}}{\partial t} - \eta\nabla^2\mathbf{u} + \rho(\mathbf{u}\cdot\nabla)\mathbf{u} + \nabla p = 0$$
$$\nabla\cdot\mathbf{u} = \mathbf{0} \qquad (2)$$

where ρ is fluid density (1000 kg m^{-3}), $\mathbf{u}$ is the velocity vector, p is pressure, and η is the dynamic viscosity (0.001 Pa·s). The domain is derived from a 2D image of a porous medium depicting grains and pore space (see below) and is established by flipping the image horizontally

and/or vertically. The resulting four components are joined together so that the pore structures match up at all boundaries forming a toroidal domain. Fluid flow is produced by an imposed horizontal macroscopic pressure gradient and no flow conditions are imposed at grain surfaces. Periodic boundary conditions for flow velocities are imposed between the left (inflow) and right (outflow) sides and the top and bottom of the domain (in Fig. 2.1).

The biogeochemistry considered is simplified and is represented by concentrations of acetate (C) and biomass in solution (B) and on the grain surfaces (B_{sfc}, expressed per area) only. The governing equations take into account advection, diffusion and reaction:

$$\frac{\partial C}{\partial t} = \nabla \cdot (D_C \nabla C) - \mathbf{u} \cdot \nabla C - R_{\mathrm{ac}} B + R_{prod} \tag{3}$$

$$\frac{\partial B}{\partial t} = \nabla \cdot (D_B \nabla B) - \mathbf{u} \cdot \nabla B + g R_{ac} B - \mu_B B \tag{4}$$

$$\frac{\partial B_{sfc}}{\partial t} = g R_{ac} B_{sfc} - \mu_B B_{sfc} + R_{ex} \tag{5}$$

where D_C and D_B are the diffusion coefficients for acetate and biomass in solution, R_{prod} is the volumetric acetate production rate through fermentation, R_{ac} is the cell specific rate of acetate consumption, g is the growth efficiency, R_{ex} is the net exchange rate due to adsorption and desorption of bacteria to and from grain surfaces (see Eq. 6 below), and μ_B describes the rate of cell death (see next paragraph). Acetate uptake by surface attached bacteria is accounted for via a flux condition at the grain surface, $\mathbf{n} \cdot \left(-D_C \nabla C + \mathbf{u} C\right) = -R_{\mathrm{ac}} B_{sfc}$, where $\mathbf{n}$ is the outward normal vector to the grain surface. Continuity across connected interfaces is ensured. Boundary conditions for biomass concentrations are established in the same fashion, except that at the grain surface, the flux is set equal to the net rate of attachment and detachment (R_{ex}), i.e. $\mathbf{n} \cdot \left(-D_B \nabla B + \mathbf{u} B\right) = R_{\mathrm{ex}}$. Two-dimensional representations of grain geometries are implemented

in the finite element simulation environment COMSOL. Pore space is discretized into ~135,000 triangular finite elements. Fluid flow is computed using a direct solver (UMFPACK; Davis and Duff, 1999). Subsequently, steady state distributions of the remaining state variables (C, B, B_{sfc}) are solved for using constant initial conditions ($1x10^{-4}$ M acetate; 0.04 grams dry weight (gdw) m^{-3} biomass) and employing UMFPACK.

Pore scale simulations are performed for a grain arrangement from the Sherwood sandstone aquifer using an image from Scott and Barker (2005) of size 2.3 by 1.76 mm. Porosity (θ) is 0.44, and the pore volume to grain surface area s_{VA} is approximately $5.4x10^{-5}$ m. The macroscopic pressure gradients are chosen so that mean flow velocities computed are consistent with that seen in the phenol contaminant plume (Watson et al. 2005), on the order of $2x10^{-7}$ m s^{-1}. The diffusion coefficient for acetate, D_C, is set to 10^{-9} m^2 s^{-1} (Boudreau, 1996) and for biomass (D_B) is set to 10^{-10} m^2 s^{-1}. Acetate production is set to $R_{prod} = 10^{-8}$ mol m^{-3} s^{-1} to be consistent with phenol breakdown rates seen in Watson et al. (2005), and is distributed evenly throughout the domain. Acetate consumption is defined using Monod kinetics, $R_{ac} = k_{ac} \frac{C}{K_{mac} + C}$, with the half saturation constant K_{mac} set to 10 μM and a maximum rate k_{ac} = 20 mmol (gram dry weight, g_{dw})$^{-1}$ hr^{-1} (Esteve-Núñez et al. 2005). The growth efficiency, g (Eq. 5), is defined as a function of the acetate concentration based on cell model results and reaches about 4.4 g_{dw} $mol_{acetate}^{-1}$ under replete substrate conditions and approaches 0 at approximately 0.5 μM acetate levels (King et al. 2009). Acetate concentrations below this threshold are not sufficient to sustain growth as cell maintenance requirements exceed ATP production (King et al. 2009), and cell death occurs at a rate of 1% of the maximum growth rate. Following Murphy and Ginn (2000) and Saiers and Hornberger et al. (1996), microbial surface attachment and detachment (R_{ex}) are given by:

$$R_{ex} = s_{VA} k_{ads} \frac{(\Gamma_{\max} - B_{sfc})}{\Gamma_{\max}} B - k_{des} B_{sfc} \quad (6)$$

where Γ_{max} is the maximum surface coverage of microbes on the grains (0.04 g_{dw} m^{-2}) calculated from monolayer coverage assuming a rectangular bacterial shape of size 0.4 μm x 2.5 μm (Seeliger et al. 1998) and a cell dry weight of 40 fg, k_{ads} is the cell surface attachment rate of 2.1×10^{-3} s^{-1}, and k_{des} is the cell surface detachment rate of 1.2×10^{-5} s^{-1} (Bradford et al. 2002). This simplified representation limits surface attached bacteria to a monolayer with no significant feedback on fluid flow. Hence, it cannot represent the formation of biofilms that can lead to heterogeneity at the pore scale (e.g. Davison et al. 1997, Suchomel et al. 1998). Also, while there is no independent observation validating the flow field, by computing hydraulic conductivity from pore scale simulations and comparing them to experimentally determined values in larger scale experiments, Narsilio et al. (2009) showed the validity of Navier-Stokes pore scale simulations in a comparable setting. Finally, our pore scale model does not account for bimodal porosity distributions, which have been shown to lead to preferential flow paths that can result in patchy distributions of substrate and biomass at the cm scale (Copolla et al. 2009). This is juxtaposed by considering only two rather than the physical three spatial dimensions, which tends to underestimate the connectivity of the pore network and hence promote patchy distributions.

2.2. Large scale models

The macroscale reactive transport simulations are based on the work by Watson et al. (2005) who studied the fate of a contaminant plume using a 2D vertical aquifer cross section. Their description included phenol breakdown as a two-step process. The first step involved fermentative reactions producing acetate, inorganic carbon, and H_2 and the second step

considered the subsequent breakdown of these intermediates. The reaction network also included sorption reactions involving iron phases and took into account the precipitation of iron sulfides. In our approach, we adapted the reactive transport model presented in Spiteri et al. (2007, 2008) to simulate the spatio-temporal evolution of this phenol plume. In brief, based on conservation of mass, the concentration field of a solute (C_k, in mass per pore volume) is given by

$$\frac{\partial \theta C_k}{\partial t} = \nabla \cdot (\mathbf{D}^* \nabla C_k) - \nabla \cdot (\theta \mathbf{v} C_k) + \theta R_k \qquad (7)$$

where θ is porosity, $\mathbf{v}$ is the flow velocity, and R_k is the net reaction rate of species k in mass per time and pore volume. The diffusion-dispersion tensor $\mathbf{D}^*$ is defined as

$$D_{ij}^* = \theta D^m \delta_{ij} + (\alpha_L - \alpha_T) \frac{v_i v_j}{|v|} + \alpha_T |v| \delta_{ij}, \qquad (8)$$

where $v = (v_i, v_j)$ and D^m, δ_{ij}, α_L and α_T are tortuosity corrected *in situ* molecular diffusion coefficient, Kronecker symbol, and longitudinal and transverse dispersivities, respectively (Scheidegger 1961). Solids and surface attached microorganisms are assumed to be immobile, so that

$$\frac{d(1-\theta)c_k}{dt} = (1-\theta) r_k \qquad (9)$$

where c_k is the concentration of compound k in mass per solid volume, and r_k is the net reaction rate of species k in mass per time and solid volume.

The governing equations are discretized using a Galerkin finite element formulation and forward Euler time stepping. Transport and reaction operators are split (Steefel and MacQuarrie 1996) and in each timestep, the transport of the solutes is first computed using a diagonally preconditioned conjugate gradient solver (Reddy 1993, Meile and Tuncay 2006). Subsequently, the set of coupled ordinary differential equations representing the reaction network is solved at

each node using the VODE solver, employing backward differentiation and full Jacobian settings (Brown et al. 1989).

Equilibrium reactions describing the speciation and surface adsorption of reactants are computed at the end of each timestep through mass-action expressions that are simplifications of these complex reactions. Mass action is expressed as $a_j = K_j \prod_i^{nc} a_i^{q_{ji}}$, where *a* denote activities, K_j is the equilibrium constant, q_{ji} are the stoichiometric coefficients and *nc* is the number of components. Mass conservation is ensured (to within a tolerance of 1×10^{-10} mol m^{-3}) by matching the total imposed mass of a component *i* (T_i) with the summed contributions from all species (*S*) in which that element is speciated, $T_i = \sum_j^m q_{ji}[S_j]$, where *m* is the number of species. Activities and concentrations are linked via activity coefficients assuming an ionic strength of 0.1 and computed using the Davies (1962) equation. Mass action laws are linearized by a log transformation, and the system $a_i \leftarrow a_i - \mathbf{J}^{-1} Y_i$, where $Y_i = T_i - \sum_j^m q_{ji}[S_j]$, [$S_j$] is the concentration of species *j* in the last iteration, and **J** denotes the Jacobian matrix $J_{ij} = \frac{\partial Y_i}{\partial a_j}$, is solved iteratively using a Newton-Raphson root finding procedure (Tadanier and Eick 2002). In this manner, pH is computed at each timestep from the local solution composition, taking into account the acid-base equilibrium of the dissolved inorganic carbon and sulfide species, precipitation and dissolution of iron sulfides, as well as fast surface exchange reactions.

Simulations are performed representative of a well-characterized site contaminated with phenolic compounds in the West Midlands, England (e.g. Thornton et al. 2001a,b, Mayer et al. 2001), with a uniform horizontal plume propagation speed (v_i) on the order of 10 m yr^{-1}. We

compare simulations for a number of reaction networks that differ in their complexity, ranging from a set that only includes the oxidation of high molecular weight organic matter and subsequent terminal metabolism to a description that encompasses chemotrophic and abiotic oxidation reactions that compete with the heterotrophic respiration for electron acceptors, precipitation reactions and microbial dynamics. The baseline reaction network for the contaminant plume simulations follows Watson et al. (2005), with the exception that their work employs different reaction rate constants (k_{max} values, Table 2.1) inside and outside of the plume while we employ one single value for each reaction. The baseline network considers the fermentation of phenol, and the subsequent respiration of H_2, precipitation of iron sulfides, as well as sorption reactions involving iron phases ("baseline" network, consisting of primary (P) and equilibrium (E) reactions given in Table 2.1). The complexity of the "baseline" network is increased by including the oxidation of reduced species (secondary reactions (S) in Table 2.1) and further expanded by taking carbonate mineral precipitation and dissolution reactions into account (mineral reactions (M) in Table 2.1). Parameters for secondary reactions were taken from Hunter et al. (1998), except that the rate constants for iron oxidation with O_2 and methane oxidation with sulfate were lowered by approximately 3 orders of magnitude to provide results that were consistent with the field data shown in Thornton et al. (2001b).

In the above formulations, the microbial populations are not represented explicitly, even though they catalyze the majority of the processes considered. To take into account microbial dynamics, "microbial" model simulations were performed that included three key functional groups of microbes that promote the breakdown of phenol and consumption of H_2 (phenol fermenting, phenol respiring, and H_2 respiring organisms; Table 2.1). The microbial groups are described by

$$\frac{\partial \theta B_i}{\partial t} = \nabla \cdot (\mathbf{D}^* \nabla B_i) - \nabla \cdot (\theta \mathbf{v} B_i) + \theta \left(g \delta R_i - \mu_i B_i \right) \quad (10)$$

where μ_i is the death rate of microbial group i (Table 2.2) and δ denotes the ammonium availability ($\delta = 1$ if NH_4^+ is present and 0 otherwise). Ammonium is subject to oxidation as well as biological uptake and recycling through cell death. Biological uptake of ammonium is dependent on cell growth by assuming a cell carbon content of 0.22 g_C ml^{-1} (Bratbak and Dundas 1984) and a Redfield C:N ratio. Upon death, ammonium is released from the cells in the same proportions as incorporated during growth. Ammonium was not accounted for in Watson et al. (2005) and boundary conditions are implemented based upon well data (Williams et al. 2001). Reaction rates are formulated as in the simulations without microbial dynamics (i.e. the kinetic expressions F_{kin} given in Table 2.1) except that they also contain a dependency on thermodynamic conditions (F_{thd}) and biomass abundance:

$$R_i = F_{kin} \cdot F_{thd} \cdot B \quad (11)$$

where B reflects the biomass concentration of the microbial population performing the reaction. The thermodynamic factor F_{thd} accounts for the energy available in the microbe's environment through a dependency on the Gibbs free energy of reaction (Boudart 1976, Jin and Bethke 2003), and reflects that catabolic processes will ultimately shut down under conditions that do not allow for ATP production. This factor is defined as $\max\left[0, 1 - \exp\left(\frac{-\Delta G_{rxn} - m\Delta G_{ATP}}{\chi RT}\right)\right]$, where ΔG_{rxn} is the Gibbs free energy of reaction, ΔG_{ATP} is the phosphorylation potential and m and χ are reaction specific parameters (Jin and Bethke (2005); Table 2.2).

Additional *s*imulations are performed at a coastal marine site (station S4) in the eastern Skagerrak between Denmark and Norway. The 1D reactive transport model STEADYSED, calibrated for this site (Wang and Van Cappellen 1996), was employed to analyze the effects of

using simplified reaction networks describing sedimentary early diagenesis. Similar to the contaminant plume setting, the model takes into account the decomposition of organic matter, which includes oxic respiration, denitrification, manganese and iron oxide reduction, sulfate reduction, and methanogenesis, but it does not explicitly account for the intermediates of terminal electron accepting processes (e.g. H_2 and acetate). Reduced species are subject to secondary redox reactions and to mineral precipitation and adsorption, leading to a reaction network similar to that considered in the contaminant plume simulations, not including explicit microbial dynamics. The results of the simulations are compared for a reaction network that considers the secondary reactions versus one that ignores them (reactions I-7 to I-18 in Wang and Van Cappellen 1996).

3. Results and Discussion

3.1 Pore scale simulations

Using our simple approximation to microbial respiration, simulations show the existence of preferential flow paths (Fig. 2.1). However, pore scale heterogeneity in biomass and substrate concentrations is small. Steady state distributions of acetate and biomass in solution computed from Eqns. (3)-(5) for the Sherwood aquifer setting show virtually no variation at the pore scale (Fig. 2.1; the quartile ranges of concentrations in the fluid phase, determined from simulations results interpolated onto 10^8 evenly spaced points creating a regular 0.46 μm by 0.35 μm grid, are 0.48-0.49 μM and 0.22 and 0.24 mg_{dw} m^{-3}, respectively). Homogeneity in concentrations stems from diffusion as a dominant process at this scale (Peclet and Damköhler numbers are less than 0.1 for a length scale of 100 μm). Acetate concentrations have reached the point where its uptake is limiting growth. Sorption/desorption occurs at a sufficient rate to cause a near-

equilibrium distribution between mobile and immobile biomass, with the majority of the cells (>98%) being surface-associated.

To elucidate the conditions under which either the flow regime or reaction dynamics vary significantly at the grain scale, the parameterization of the baseline simulations was altered systematically. A ten-fold increase in the substrate production rate R_{prod} from 10^{-8} to 10^{-7} mol m^{-3} s^{-1} or a spatially uneven distribution of acetate production (e.g. production via breakdown of particulate organic matter, modeled as a source term associated with grain surfaces or constrained to a single quadrant of the domain) did not lead not lead to patchy concentration fields. Substantial spatial variations in substrate and biomass concentrations are seen only when R_{prod} is increased by two orders of magnitude. Under this condition, quartile ranges for the aquifer are 0.46 – 0.63 μM acetate and 0.023 – 0.029 g_{dw} m^{-3} biomass, respectively. Similarly, increasing the pressure gradient by an order of magnitude in our simulations did not lead to spatial heterogeneity, because the advective timescale (L/average velocity) exceeds that of diffusion (L^2/D) at the scale of the domain (L), and even more so at pore level. For heterogeneity in substrate and biomass concentrations to become significant in our simulations, advective or reactive processes must occur on a shorter timescale than diffusion as observed by Raje and Kapoor (2000) and Gramling et al. (2002) in soil columns at a high Péclet number. The reactive timescale (estimated by the ratio of the average substrate concentration to the acetate consumption rate) of the simulations becomes shorter than the diffusional timescale when substrate production rates are increased by 2 orders of magnitude. This indicates that heterogeneity can potentially become dominant in environmental conditions that promote fast reactions, albeit at rates that likely exceeds microbial respiration.

3.2 Macroscopic redox zonation

All implementations of the contaminant plume reaction network are subject to the same rate laws characterizing the phenol breakdown and the resulting acetate and H_2 production, with the exception of the simulations in which the microbial populations are accounted for explicitly. With only a fraction of the inflowing phenol being degraded, and due to the similarity in rate laws in all simulations, the phenol plume (Fig. 2.2A) is nearly identical in shape and magnitude in all simulations, matching the observations closely (see comparison of model results to the measured well profile in Fig. 2.2C). However, because of the dependency of aerobic phenol breakdown and denitrification (P1 and P2 in Table 2.1) on O_2 and NO_3^- concentrations, the competition for oxidants by introduction of secondary reactions leads to a drop in the aerobic respiration rate. Taking into account use of O_2 in the oxidation of reduced inorganics leads to an ~40% lower phenol breakdown over the course of the 47 years studied compared to the baseline network alone, and the contribution of aerobic to total phenol degradation is reduced from ~48 to ~14% (Table 2.3).

Rate laws of acetate and total H_2 consumption via methanogenesis and the reduction of sulfate and iron and manganese oxides are identical for the above networks, and both acetate and H_2 contours roughly follow the plume outline for the reaction networks analyzed (Fig. 2.2A, B). Following the implementation in Watson et al. (2005), H_2 respiration is only modeled in suboxic and anoxic conditions. This is consistent with the absence of any overlap between O_2 and H_2 in field measurements (Thornton et al. 2001b), as well as in our model simulations. Therefore, in contrast to the impact of secondary reactions on phenol degradation, little to no effect from secondary reactions on H_2 dynamics is observed. The impact of the further addition of carbonate

mineral precipitation on DIC concentrations is small, so that the DIC plume in Figure 2.2B is representative for all reaction networks.

Redox sensitive products of the organic matter breakdown reactions reveal differences between reaction networks. Simulations only accounting for primary reactions match measured Mn(II) levels fairly well (Thornton et al. 2001b; not shown), but lead to dissolved iron concentrations exceeding those observed (Table 2.3; simulated Fe^{2+} levels at well BH60 after 47 years are approximately 3 fold higher than the measured values shown in Figure 3 of Thornton et al. 2001b). In all reaction networks investigated, the total concentration of iron oxides was virtually unaffected by the different reaction networks because of the large pool size. In addition, the total reduced iron pool (Fe^{2+} + >Fe + FeS + $FeCO_3$; where >Fe represents surface adsorbed iron) varies by less than a factor of 3 (Table 2.3); however, the speciation of the iron can differ substantially. Taking into account secondary reactions results in an increase of Fe^{2+} by ~10% and an ~75% decrease in the amount of FeS. The inclusion of mineral precipitation reactions tends to lower the Fe^{2+}, >Fe, and FeS pools since the iron is precipitated as $FeCO_3$, which constitutes the largest sink for reduced iron (~60%).

As for the contaminant plume, inclusion of secondary reactions in sediment simulations results in the lowering of the importance of the aerobic degradation of organic matter from ~32 to 11% (Table 2.3). The effect of network complexity on iron speciation has a greater impact in the marine sediment than in the contaminant plume setting. For example, iron oxide levels are ~3.5 times more prevalent considering the full reaction network than in simulations not accounting for the secondary reactions. Inclusion of secondary reactions also impacts reduced iron pools, doubling the integrated Fe^{2+} concentrations while FeS decreases by ~39%. In comparison, addition of the secondary reactions in the contaminant plume results in a 10%

increase in Fe^{2+} levels. Overall, total reduced iron levels are increased by ~12% upon accounting for secondary reactions (Table 2.3).

Aside from these highlighted differences in iron pools, our results show that changes in the reaction network have relatively little impact on pool sizes for most chemicals, but can affect reaction pathways. This is consistent with the results of Hunter et al. (1998) who assessed the importance of secondary reactions in simulations of a pristine aquifer contaminated by a landfill leachate. They found that the concentrations of organic matter were unaffected by the inclusion of secondary reactions, but that consistent with the effects on aerobic oxidation of phenol, the competition for O_2 by secondary reactions altered the pathways of organic matter decomposition. Thullner et al. (2005) determined that manganese reduction was completely controlled by secondary reactions in a coastal marine setting, although it was more pronounced than the impact of secondary reactions on iron cycling presented here. These results highlight the fact that not taking into account all of the relevant reactions can lead to improper conclusions about the importance of biodegradation pathways. They also show that the specific environment plays a role in the extent of the effect of secondary reactions. Inclusion of secondary reactions has a greater effect in the sediment environment, where redox interfaces are more prevalent and O_2 consumption via secondary reactions plays a greater role than in the contaminant plume simulation.

3.3 Plume scale microbial distributions

The addition of explicit descriptions of phenol fermenting, phenol respiring, and hydrogen respiring microbial populations lead to little spatial variability in modeled cell densities. Phenol fermenters were estimated to be present predominantly within the plume at ~$8x10^6$ cells ml^{-1},

while computed phenol respiring organisms were found near the plume edge in similar concentrations; H_2 oxidizers were similar in spatial extent to the phenol fermenters but present at higher concentrations of ~$2x10^7$ cells ml^{-1} (not shown). . Inclusion of microbial populations leads to geochemical distribution patterns consistent with the observations (Fig. 2.2). Our parameterization slightly underpredicted dissolved inorganic carbon production (Fig. 2.2D), concurring with a higher estimate of acetate than the non-biotic reaction networks which in part is also caused by a slightly higher phenol breakdown. While total iron levels are consistent with non-biotic simulations, there is an approximate doubling of the $FeCO_3$ and increased dissimilatory iron reduction (Table 2.3).

Our simulations show relatively little spatial variation in total bacterial numbers (not shown). Consistent with our findings, Thullner et al. (2005), who introduced microbial groups into a reactive transport model describing a marine sediment, determined that bacteria were distributed homogenously. Similarly, Dale et al. (2006), who accounted for bacterial groups and energetic limitation in coastal sediment, also found little variation in bacterial biomass concentrations over time. Our simulations also indicate that the regulation of biomass levels depends on nitrogen limitations and thermodynamic constraints (Fig. 2.3). This finding in our carbon rich environment contrasts starkly with dissolved organic carbon limited microbial populations in a groundwater setting described by Lensing et al. (1994). Simulations that did not take in to account nitrogen limitation demonstrated unrestrained bacterial growth due to the virtually unlimited availability of phenol, while simulations with no thermodynamic constraints resulted in lower H_2 concentration throughout the domain (not shown). Nitrogen is abundant within approximately the first 75 m of the domain and does not inhibit microbial growth, while the remainder of the plume is nitrogen limited (Fig. 3B). An analysis of bacterial growth

dynamics within nitrogen limited regions shows a steady state existence of the bacterial groups with cell death and nitrogen release being balanced by subsequent growth. Abundant energy is available for bacteria respiring O_2 and NO_3^-, but for organisms fermenting high molecular weight organic compounds, F_{thd} varies from ~0.6 to 1 with the strongest thermodynamic constraints in areas of the plume with the highest acetate concentrations (Fig. 2.3A). The bacterial group respiring H_2 shows an F_{thd} term that varies between ~0.5 and 0.7 (Fig. 2.3B), suggesting that energetic constraints contribute to shaping in situ microbial activity.

4. Conclusions

This study, focusing on conditions in a sandy aquifer, assesses two aspects that may pose limitations to reactive transport modeling: pore scale variability and the comprehensiveness of the (micro-)biogeochemical processes considered.

First, simulations of flow and concentration fields subject to (idealized) biogeochemical dynamics suggest little spatial variability in substrate and biomass distributions at the grain scale, at least under conditions that do not favor the formation of biofilms. Second, results from simulations using different reaction networks show that a relatively simple reaction network can provide an accurate prediction of the observed distribution of dissolved substances in a contaminant plume. However, depending on the complexity of the reaction network used, distinct differences can exist in individual process rates affecting these pools. Simulations of the breakdown of organics in groundwater highlights the importance of reoxidation reactions in settings characterized by strong redox gradients over a large part of the model domain; a finding supported by the assessment of their impact on process dynamics in coastal marine surface sediments. This is notable, because while concentration fields only denote snapshots compared to

transient model simulations, they are typically used for model validation. Our results emphasize the need for comparison of modeled process dynamics with measured rates, which are difficult to obtain and hence are not readily available.

Consistent with the results of Wang and Papenguth (2001), we found that a description of subsurface process may not always require an explicit representation of microbial biomass, particularly in settings characterized by minimal microbial activity. However, accounting for growth of microbes and associated reaction rates requires going beyond implementation of a kinetic substrate dependency of biomass alone. Notably, inclusion of nitrogen limitations appeared necessary in a setting fueled by carbohydrates to avoid excessive microbial growth due to abundant C-substrate. The need to account for a range of feedback mechanisms between microbial activity and environmental conditions suggests that understanding microbial requirements (which may extend well beyond the factors and chemical substances encompassed in current reactive transport models) may be central to quantify controls on bioremediation in the field.

Acknowledgments

We thank Harlan Miller III for his help with the pore scale simulations and Philippe Van Cappellen for use of STEADYSED. This work was supported by the Office of Science of the United States Department of Energy (DE-FG02-05ER25676), and it benefited substantially from the constructive criticism and insightful comments of 3 anonymous reviewers.[2]

[2] Per the committees request, minimal edits were made to this chapter including an error in eq. 6.

References

Boudart, M. 1976. Consistency between Kinetics and Thermodynamics. J. Phys. Chem. 80, 2869-2870.

Boudreau, B.P. 1996. A method-of-lines code for carbon and nutrient diagenesis in aquatic sediments. Comput. Geosci. 22(5), 479-496.

Bradford, S.A., Yates, S.R., Bettahar, M. and Simunek, J. 2002. Physical factors affecting the transport and fate of colloids in saturated porous media. Water Resour. Res. 38, 1327-1339.

Bratbak, G. and Dundas, I. 1984. Bacterial dry-matter content and biomass estimations. Appl. Environ. Microbiol. 48, 755-757.

Brown, P.N., Byrne, G.D. and Hindmarsh, A.C. 1989. VODE: A variable-coefficient ODE solver. SIAM J. Sci. Comput. 10, 1038-1051.

Coppola, A., Comegna, V., Basile, A., Lamaddalena, N., Severino, G. 2009. Darcian preferential water flow and solute transport through bimodal porous systems: Experiments and modeling. J. Contam. Hydrol. 104, 74-83.

Cygan, R.T., Stevens, C.T., Puls, R.W., Yabusaki, S.B., Wauchope, R.D., McGrath, C.J., Curtis, G.P., Siegel, M.D., Veblen, L.A. and Turner, D.R. 2007. Research activities at U.S. government agencies in subsurface reactive transport Modeling. Vadose Zone J. 6, 805-822.

Dale, A.W., Regnier, P. and Van Cappellen, P. 2006. Bioenergetic controls on anaerobic oxidation of methane (AOM) in coastal marine sediments: A theoretical analysis. Am. J. Sci. 306, 246-294.

Davies, C. W. 1962. Ion Association. Butterworths, London.

Davis, T.A. and Duff, I.S. 1999. A combined unifrontal/multifrontal method for unsymmetric sparse matrices, ACM Trans. Math. Softw. 25, 1-20.

Davison, W., Fones, G.R., and Grime, G.W. 1997. Dissolved metals in surface sediment and a microbial mat at 100-μm resolution. Nature. 387, 885-888.

Esteve-Núñez, A., Rothermich, M., Sharma, M. and Lovley, D.R. 2005. Growth of Geobacter sulfurreducens under nutrient-limiting conditions in continuous culture. Environ. Microbiol. 7, 641-648.

Ginn, T.R., Wood, B.D., Nelson, K.E., Scheibe, T.D., Murphy, E.M. and Clement, T.P. 2002. Processes in microbial transport in the natural subsurface. Adv. Water Res. 25, 1017-1042.

Gramling, C.M., Harvey, C.F. and Meigs, L.C. 2002. Reactive transport in porous media: A comparison of model prediction with laboratory visualization. Environ. Sci. Technol. 36, 2508-2514.

Hassanizadeh, S.M. 1995. On the transient non-Fickian dispersion theory. Transp. Porous Media. 23, 107-124.

Hornberger, G.M., Mills, A.L. and Herman, J.S. 1992. Bacterial transport in porous-media - evaluation of a model using laboratory observations. Water Resour. Res. 28(3), 915-923.

Hunter, K.S., Wang, Y. and Van Cappellen, P. 1998. Kinetic modeling of microbially-driven redox chemistry in subsurface environments: coupling transport, microbial metabolism and geochemistry. J. Hydrol. 209, 53-58.

Jakobsen, R., Albrechtsen, H.J., Rasmussen, M., Bay, H., Bjerg, P.L. and Christensen, T.H. 1998. H_2 concentrations in a landfill leachate plume (Grinsted, Denmark): in situ energetics of terminal electron acceptor processes. Environ. Sci. Technol. 32, 2142-2148.

Jakobsen, R. and Postma, D. 1999. Redox zoning, rates of sulfate reduction and interactions with Fe-reduction and methanogenesis in a shallow sandy aquifer, Romo, Denmark. Geochim. Cosmochim. Acta 63,137-151.

Jakobsen, R. 2007. Redox microniches in groundwater: A model study on the geometric and kinetic conditions required for concomitant Fe oxide reduction, sulfate reduction, and methanogenesis. Water Resour. Res. 43(12), W12S12.

Jakobsen, R. and Cold, L. 2007. Geochemistry at the sulfate reduction-methanogenesis transition zone in an anoxic aquifer : A partial equilibrium interpretation using 2D reactive transport modeling. Geochim. Cosmochim. Acta 71, 1949-1966.

Jin, Q. and Bethke, C.M. 2003. A new rate law describing microbial respiration. Appl. Environ. Microbiol. 69, 2340-2348.

Jin, Q.S. and Bethke, C.M. 2005. Predicting the rate of microbial respiration in geochemical environments. Geochim. Cosmochim. Acta 69(5): 1133-1143.

King, E.L., Tuncay, K., Ortoleva, P. and Meile, C. 2009. In silico microbial metabolism of Geobacter sulfurreducens and its representation in reactive transport models. Appl. Environ. Microbiol. *doi:10.1128/AEM.01799-08*

Lensing, H.J., Vogt, M. and Herrling, B. 1994. Modeling of biologically mediated redox processes in the subsurface. J. Hydrol. 159, 125-143.

Levy, M. and Berkowitz, B. 2003. Measurement and analysis of non-Fickian dispersion in heterogeneous porous media. J. Contam. Hydrol. 64, 203-226.

Li, D., Velde, B. and Zhan, T. 2004. Observations of pores and aggregates during aggregation in some clay-rich agricultural soils as seen in 2D image analysis. Geoderma. 118, 191-207.

Li, L., Peters, C.A. and Celia, M.A. 2006. Upscaling geochemical reaction rates using pore-scale network modeling. Adv. Water Res. 29, 1351-1370.

Li, L., Steefel, C.I. and Yang, L. 2008. Scale dependence of mineral dissolution rates within single pores and fractures. Geochim. Cosmochim. Acta 72, 360-377.

Lovley, D.R. and Goodwin, S. 1988. Hydrogen concentrations as an indicator of the predominant terminal electron-accepting reactions in aquatic sediments. Geochim. Cosmochim. Acta 52, 2993-3003.

Mayer, K.U., Benner, S.G., Frind, E.O., Thornton, S.F. and Lerner, D.N. 2001. Reactive transport modeling of processes controlling the distribution and natural attenuation of phenolic compounds in a deep sandstone aquifer. J. Contam. Hydrol. 53, 341-368.

McNab, W.W. and Narasimhan, T.N. 1994. Modeling reactive transport of organic-compounds in groundwater using a partial redox disequilibrium approach. Water Resour. Res. 30, 2619-2635.

McNab, W.W. and Narasimhan, T.N. 1995. Reactive transport of petroleum hydrocarbon constituents in a shallow aquifer : modeling geochemical interactions between organic and inorganic species. Water Resour. Res. 31, 2027-2033.

Meile, C. and Tuncay, K. 2006. Scale dependence of reaction rates in porous media. Adv. Water Res. 29, 62-71.

Miller, C.T., Christakos, G., Imhoff, P.T., McBride, J.F., Pedit, J.A. and Trangenstein, J.A. 1998. Multiphase Flow and Transport Modeling in Heterogeneous Porous Media: Challenges and Approaches. Adv. Water Res. 21, 77-120.

Murphy, E.M. and Ginn, T.R. 2000. Modeling microbial processes in porous media. Hydrogeol. J. 9, 142-158.

Narsilio, G.A., Buzzi, O., Fityus, S., Yun, T.S., Smith, D.W. 2009. Upscaling of Navier-Stokes equations in porous media: Theoretical, numerical and experimental approach. Comput. and Geotech. 36(7), 1200-1206.

Pett-Ridge, J. and Firestone, M.K. 2005. Redox fluctuation structures microbial communities in a wet tropical soil. Appl. Environ. Microbiol. 71, 6998-7007.

Raje, D.S. and Kapoor, V. 2000. Experimental study of bimolecular reaction kinetics in porous media. Environ. Sci. Technol. 34, 1234-1239.

Reddy, J. 1993. An introduction to the finite element method. 2nd ed. New York: McGraw-Hill, Inc. 684p.

Roden, E.E. and Scheibe, T.D. 2005. Conceptual and numerical model of uranium(VI) reductive immobilization in fractured subsurface sediments. Chemosphere 59, 617-628.

Rotter, B.E., Barry, D.A., Gerhard, J.I. and Small, J.S. 2008. Modeling U(VI) biomineralization in single- and dual-porosity porous media. Water Resour. Res. 44, W08437, doi:10.1029/2007WR006301.

Saiers, J.E. and Hornberger, G.M. 1996. Migration of Cs-137 through quartz sand: Experimental results and modeling approaches. J. Contam. Hydrol. 22(3-4), 255-270.

Scheidegger, A. 1961. General theory of dispersion in porous media. J. Geophys. Res. 66, 3273-3278.

Scott, J.B.T. and Barker, R.D. 2005. Characterization of sandstone by electrical spectroscopy for stratigraphical and hydrogeological investigations. Q. J. Eng. Geol.Hydrogeol. 38, 143-154.

Seeliger, S., Cord-Ruwisch, R. and Schink, B. 1998. A periplasmic and extracellular c-type cytochrome of Geobacter sulfurreducens acts as a ferric iron reductase and as an electron carrier to other acceptors or to partner bacteria. J. Bacteriol. 180(14), 3686-3691.

Sochaczewski L., Stockdale A., Davison W., Tych W., and Zhang H. 2008. A three-dimensional reactive transport model for sediments, incorporating microniches. Environ. Chem., 5(3), 218-225.

Soetaert, K., Herman, P.M.J. and Middelburg, J.J., 1996. A model of early diagenetic processes from the shelf to abyssal depths. Geochim. Cosmochim. Acta 60(6), 1019-1040.

Spiteri, C., Slomp, C.P., Regnier, P., Meile, C. and Van Cappellen, P. 2007. Modeling the geochemical fate and transport of wastewater-derived phosphorus in two contrasting shallow aquifers. J. Contam. Hydrol. 71, 2240-2249.

Spiteri, C., Slomp, C., Tuncay, K. and Meile, C. 2008. Modeling biogeochemical processes in subterranean estuaries: The effect of flow dynamics and redox conditions on submarine groundwater discharge of nutrients. Water Resour. Res. 44, doi:10.1029/2007WR006071.

Steefel, C. and MacQuarrie, K. 1996. Approaches to modeling of reactive transport in porous media, p. 83-130. In: Lichtner, P., Steefel, C. and Oelkers, E. [Eds.] Reactive transport in porous media Vol. 34. Mineralogical Society of America.

Steefel, C.I., DePaolo, D.J. and Lichtner, P.C. 2005. Reactive transport modeling: An essential tool and a new research approach for the Earth sciences. Earth Planet. Sci. Lett. 240, 539-558.

Stumm, W. and Morgan, J.J. 1996. Aquatic Chemistry. John Wiley& Sons, Inc. 1022p.

Suchomel, B.J., Chen, B.M., Allen, M.B. 1998. Network model of flow, transport and biofilm effects in porous media. Transp. Porous Media. 30(10), 1-23.

Szecsody, J.E., Zachara, J.M., Chilakapati, A., Jardine, P.M. and Ferrency, A.S. 1998. Importance of flow and particle-scale heterogeneity on CoII/III EDTA reactive transport. J. Hydrol. 209, 112-136.

Tadanier, C.J. and Eick, M.J. 2002. Formulating the charge-distribution multisite surface complexation model using FITEQL. Soil Sci. Soc. Am. J. 66, 1505-1517.

Thullner, M., Van Cappellen, P. and Regnier, P. 2005. Modeling the impact of microbial activity on redox dynamics in porous media. Geochim. Cosmochim. Acta. 69, 5005-5019.

Thornton, S.F., Lerner, D.N. and Banwart, S.A. 2001.[a] Assessing the natural attenuation of organic contaminants in aquifers using plume-scale electron and carbon balances: model development with analysis of uncertainty and parameter sensitivity. J. Contam. Hydrol. 53, 199-232.

Thornton, S.F., Quigley, S., Spence, M.J., Banwart, S.A., Bottrell, S. and Lerner, D.N. 2001.[b] Processes controlling the distribution and natural attenuation of dissolved phenolic compounds in a deep sandstone aquifer. J. Contam. Hydrol. 53, 233-267.

Van Cappellen, P. and Wang, Y. 1996. Cycling of iron and manganese in surface sediments: A general theory for the coupled transport and reaction of carbon, oxygen, nitrogen, sulfur, iron and manganese. Am. J. Sci. 296, 197-243.

Varma, A. and Palsson, B. O. 1994. Stoichiometric flux balance models quantitatively predict growth and metabolic by-product secretion in wild-Type Escherichia-coli W3110. Appl. Environ. Microbiol. 60, 3724-3731.

Wang, Y. and Van Cappellen, P. 1996. A multicomponent reactive transport model of early diagenesis: Application to redox cycling in coastal marine sediments. Geochim. Cosmochim. Acta 60, 2993-3014.

Wang, Y. and Papenguth, H.W. 2001. Kinetic modeling of microbially-driven redox chemistry of radionuclides in subsurface environments: coupling transport, microbial metabolism and geochemistry. J. Contam. Hydrol. 47, 297-309.

Watson, I.A., Oswald, S.E., Banwart, S.A., Crouch, R.S. and Thornton, S.F. 2005. Modeling the dynamics of fermentation and respiratory processes in a groundwater plume of phenolic contaminants interpreted from laboratory- to field-scale. Environ. Sci. Technol. 39, 8829-8839.

Williams, G.M., Pickup, R.W., Thornton, S.F., Lerner, D.N., Mallinson, H.E.H., Moore, Y. and White, C. 2001. Biogeochemical characterization of a coal tar distillate plume. J. Contam. Hydrol. 53, 175-197.

Wood, B.D., Radakovich, K., and Golfier, F. 2007. Effective reaction at a fluid–solid interface: Applications to biotransformation in porous media. Adv. Water Res. 30, 1630-1647.

Zhang, D., Zhang, R., Chen, S. and Soll, W.E. 2000. Pore scale study of flow in porous media: Scale dependency, REV, and statistical REV. Geophys. Res. Lett. 27, 1195-1198.

Table 2.1: Reactions included in the model.

Reactions	*Stoichiometry*	*Rate law (F_{kin})**	*#*
Primary Reactions (P) **			
Aerobic Degradation	$C_6H_5OH + 7O_2 + 3H_2O \rightarrow 6HCO_3^- + 6H^+$	$k_{maxP1} \cdot M_{1,phenol} \cdot M_{1,O2}$	P1
Denitrification	$C_6H_5OH + 5.6NO_3^- + 0.2H_2O \rightarrow 6HCO_3^- + 0.4H^+ + 2.8N_2$	$k_{maxP2} \cdot M_{2,phenol} \cdot M_{2,NO3} \cdot I_{2,O2}$	P2
Fermentation	$C_6H_5OH + 5H_2O \rightarrow 3CH_3COOH + 2H_2$	$k_{maxP3} \cdot M_{3,phenol} \cdot I_{3,O2} \cdot I_{3,NO3} \cdot I_{3,phenol}$	P3
Fermentation	$C_6H_5OH + 17H_2O \rightarrow 6HCO_3^- + 6H^+ + 14H_2$	$k_{maxP4} \cdot M_{4,phenol} \cdot I_{4,O2} \cdot I_{4,NO3} \cdot I_{4,phenol}$	P4
Manganese Reduction	$H_2 + MnO_2 + 2H^+ \rightarrow 2H_2O + Mn^{2+}$	$k_{maxP5} \cdot M_{5,H2} \cdot I_{5,O2} \cdot I_{5,NO3} \cdot I_{5,phenol}$	P5
Iron Reduction	$H_2 + 2FeOOH + 4H^+ \rightarrow 4H_2O + 2Fe^{2+}$	$k_{maxP6} \cdot M_{6,H2} \cdot I_{6,O2} \cdot I_{6,NO3} \cdot I_{6,phenol}$	P6
Sulfate Reduction	$H_2 + 0.25SO_4^{2-} + 0.25H^+ \rightarrow H_2O + 0.25HS^-$	$k_{maxP7} \cdot M_{7,H2} \cdot M_{7,SO4} \cdot I_{7,O2} \cdot I_{7,NO3} \cdot I_{7,phenol}$	P7
Methanogenesis	$H_2 + 0.25HCO_3^- + 0.25H^+ \rightarrow 0.75H_2O + 0.25CH_4$	$k_{maxP8} \cdot M_{8,H2} \cdot I_{8,O2} \cdot I_{8,NO3} \cdot I_{8,phenol}$	P8
Secondary Reactions (S)			
Manganese Oxidation	$Mn^{2+} + 0.5O_2 + H_2O \rightarrow MnO_2 + 2H^+$	$k_{maxS1} \cdot [Mn^{2+}] \cdot [O_2]$	S1
Iron Oxidation	$Fe^{2+} + 0.25O_2 + 1.5H_2O \rightarrow FeOOH + 2H^+$	$k_{maxS2} \cdot [Fe^{2+}] \cdot [O_2]$	S2
Iron Oxidation by MnO_2	$2Fe^{2+} + MnO_2 + 2H_2O \rightarrow 2FeOOH + Mn^{2+} + 2H^+$	$k_{maxS3} \cdot [Fe^{2+}] \cdot [MnO_2]$	S3
Sulfide Oxidation	$H_2S + 2O_2 \rightarrow SO_4^{2-} + 2H^+$	$k_{maxS4} \cdot [TS] \cdot [O_2]$	S4
Sulfide Oxidation by MnO_2	$H_2S + MnO_2 + 2H^+ \rightarrow Mn^{2+} + S^0 + 2H_2O$	$k_{maxS5} \cdot [TS] \cdot [MnO_2]$	S5
Sulfide Ox. via FeOOH	$H_2S + 2FeOOH + 4H^+ \rightarrow 2Fe^{2+} + S^0 + 4H_2O$	$k_{maxS6} \cdot [TS] \cdot [FeOOH]$	S6
FeS oxidation	$FeS + 2O_2 \rightarrow Fe^{2+} + SO_4^{2-}$	$k_{maxS7} \cdot [FeS] \cdot [O_2]$	S7
Methane Oxidation	$CH_4 + 2O_2 \rightarrow CO_2 + 2H_2O$	$k_{maxS8} \cdot [CH_4] \cdot [O_2]$	S8
Methane Ox with Sulfate	$CH_4 + SO_4^{2-} + H^+ \rightarrow H_2S + HCO_3^- + H_2O$	$k_{maxS9} \cdot [CH_4] \cdot [SO_4^{2-}]$	S9
Nitrification	$NH_4^+ + 2O_2 \rightarrow NO_3^- + 2H^+ + H_2O$	$k_{maxS10} \cdot [NH_4^+] \cdot [O_2]$	S10
Mineral Dissolution/Precipitation Reactions (M)			
$MnCO_3$ precip/dissolution	$Mn^{2+} + HCO_3^- \rightarrow MnCO_3 + H^+$	$(\delta_p \cdot k_{p,MnCO3} + \delta_d \cdot k_{d,MnCO3} \cdot [MnCO_3]) \cdot (\Omega_{MnCO3} - 1)$	M1
$FeCO_3$ precip/dissolution	$Fe^{2+} + HCO_3^- \rightarrow FeCO_3 + H^+$	$(\delta_p \cdot k_{p,FeCO3} + \delta_d \cdot k_{d,FeCO3} \cdot [FeCO_3]) \cdot (\Omega_{FeCO3} - 1)$	M2
Equilibrium Reactions (E)			

$>FeOH + Mn^{2+} = >FeOMn^{+} + H^{+}$	E1	$HCO_3^- = H^+ + CO_3^{2-}$	E6
$>FeOH + H^{+} = >FeOH_2$	E2	$H_2CO_3 = H^+ + HCO_3^-$	E7
$>FeOH = >FeO^- + H^+$	E3	$H_2O = H^+ + OH^-$	E8
$>FeOH + Fe^{2+} = >FeOFe^{+} + H^{+}$	E4	$FeS + H^+ = Fe^{2+} + HS^-$	E9
$>FeOH + Fe^{2+} + H_2O = >FeOFeOH + 2H^{+}$	E5	$H_2S = HS^- + H^+$	E10

*Monod and inhibition terms are defined as $M_{j,C} = [C]/(K_{m,j}+[C])$ and $I_{j,C} = K_{I,j}/(K_{I,j}+[C])$, respectively. Values for the reaction parameters are given in Table 2.2. For the mineral precipitation reactions/dissolution reactions, $\delta_p = 1$ and $\delta_d = 0$ if $\Omega < 1$ and $\delta_p = 0$ and $\delta_d = 1$ if $\Omega \geq 1$. Saturation states Ω_{XCO3} are defined as $[X^{2+}][HCO_3^-]/(K_{XCO3}\,[H^+])$, where X=Mn or Fe.

** In the "microbial" simulations, the kinetic expressions F_{kin} in P1-8 are divided by typical biomass concentrations, B_i^0, set to 0.8 g_{dw} m^{-3}. Phenol respiring organisms are responsible for reactions P1 and P2, phenol fermenters for P3 and P4, and H_2 utilizing organisms for P5-P8.

Table 2.2: Model parameters (sources provided as leading superscripts).

Parameter	Value	Parameter	Value
Rate constants			
$^{a}k_{maxP1}$	4.00×10^{-10} mol L^{-1} s^{-1}	$^{c}k_{maxS2}$	3.17×10^{-1} L mol^{-1} s^{-1}
$^{a}k_{maxP2}$	4.00×10^{-11} mol L^{-1} s^{-1}	$^{f}k_{maxS3}$	3.17×10^{-8} L mol^{-1} s^{-1}
$^{a}k_{maxP3}$	8.40×10^{-13} mol L^{-1} s^{-1}	$^{c}k_{maxS4}$	5.07×10^{-3} L mol^{-1} s^{-1}
$^{a}k_{maxP4}$	2.30×10^{-13} mol L^{-1} s^{-1}	$^{c}k_{maxS5}$	6.34×10^{-4} L mol^{-1} s^{-1}
$^{a}k_{maxP5}$	9.80×10^{-12} mol L^{-1} s^{-1}	$^{c}k_{maxS6}$	2.54×10^{-4} L mol^{-1} s^{-1}
$^{a}k_{maxP6}$	2.20×10^{-11} mol L^{-1} s^{-1}	$^{c}k_{maxS7}$	9.51×10^{-3} L mol^{-1} s^{-1}
$^{a}k_{maxP7}$	8.40×10^{-11} mol L^{-1} s^{-1}	$^{c}k_{maxS8}$	3.17×10^{2} L mol^{-1} s^{-1}
$^{a}k_{maxP8}$	4.34×10^{-10} mol L^{-1} s^{-1}	$^{f}k_{maxS9}$	3.17×10^{-7} L mol^{-1} s^{-1}
$^{c}k_{maxS1}$	3.17×10^{-1} L mol^{-1} s^{-1}	$^{c}k_{maxS10}$	1.59×10^{-1} L mol^{-1} s^{-1}
Monod and inhibition constants			
$^{a}K_{m,1\text{-}4(phenol)}$	1.10×10^{-4} mol L^{-1}	$^{a}K_{I,2(O2)}$	6.20×10^{-6} mol L^{-1}
$^{a}K_{m,5\text{-}6(H2)}$	5.00×10^{-7} mol L^{-1}	$^{a}K_{I,3\text{-}4(O2)}$	3.10×10^{-5} mol L^{-1}
$^{a}K_{m,7(H2)}$	1.00×10^{-6} mol L^{-1}	$^{a}K_{I,3\text{-}4(NO3)}$	1.60×10^{-5} mol L^{-1}
$^{a}K_{m,8(H2)}$	5.00×10^{-6} mol L^{-1}	$^{a}K_{I,3\text{-}4(phenol)}$	6.00×10^{-2} mol L^{-1}
$^{a}K_{m,1(O2)}$	3.10×10^{-6} mol L^{-1}	$^{a}K_{I,5\text{-}8(O2)}$	3.10×10^{-5} mol L^{-1}
$^{a}K_{m,2(NO3)}$	8.10×10^{-6} mol L^{-1}	$^{a}K_{I,5\text{-}8(NO3)}$	1.60×10^{-5} mol L^{-1}
$^{a}K_{m,7(SO4)}$	1.60×10^{-3} mol L^{-1}	$^{a}K_{I,5\text{-}8(phenol)}$	4.00×10^{-2} mol L^{-1}
Mineral reactions			
$^{c}k_{p,MnCO3}$	3.17×10^{-6} mol dm^{-3} s^{-1}	$^{c}k_{p,FeCO3}$	1.59×10^{-6} mol dm^{-3} s^{-1}
$^{c}k_{d,MnCO3}$	3.17×10^{-12} s^{-1}	$^{c}k_{d,FeCO3}$	1.59×10^{-12} s^{-1}
$^{b}K_{MnCO3}$	0.8690	$^{b}K_{FeCO3}$	0.2748
Microbial growth and thermodynamics			
$^{d}\chi_{1}$	56	$^{d}m_{5\text{-}6}$	2/3
$^{d}\chi_{2}$	28	$^{d}m_{7}$	1/3
$^{d}\chi_{3\text{-}8}$	2	$^{d}m_{8}$	2/9
$^{d}m_{1}$	28	$^{d}\Delta G_{ATP}$	50 kJ mol^{-1}
$^{d}m_{2}$	28/3	$^{e}\mu_{1}$	3.3×10^{-10} s^{-1}
$^{d}m_{3}$	2/3	$^{e}\mu_{2}$	1.65×10^{-11} s^{-1}
$^{d}m_{4}$	1	$^{e}\mu_{3}$	7.01×10^{-11} s^{-1}
Transport parameters			
$^{a}\alpha_{L}$	1 m	D^{m}	10^{-9} m^{2} s^{-1}
$^{a}\alpha_{T}$	4×10^{-4} m		

[a] Watson et al. (2005) (note that in contrast to Watson et al. (2005), no spatial variation in rate constants is considered here).

[b] Stumm and Morgan (1996).

[c] Hunter et al. (1998).

[d] Jin and Bethke (2005): note that the values for m and χ given there have been adjusted for the number of electrons transferred per reaction.

[e] Death rates are calculated as 1% of their respective maximum achieved growth rates.

[f] Inferred from simulations.

Table 2.3: Concentrations (mol m^{-1}) and reaction rates (mol m^{-1} s^{-1}) for the contaminant plume simulations under different reaction network formulations integrated over space. Percentages of total reduced iron (i.e. excluding iron oxyhydroxides for the contaminant plume) for each species are given in parentheses. For organic matter oxidation by oxygen, the percentage of total organic matter degradation is given in parentheses.

	[a] *Contaminant Plume*				[b] *Sediment*	
	P,E	*P,E,S*	[c] *P,E,S,M*	*P,E,S,M,B*	*Full - S*	*Full*
$\int_x FeOx$	$3.4\text{x}10^{6}$	$3.4\text{x}10^{6}$	$3.4\text{x}10^{6}$	$3.4\text{x}10^{6}$	$2.71\text{x}10^{1}$ (3.6)	$9.43\text{x}10^{1}$ (11.2)
$\int_x Fe^{2+}$	$8.1\text{x}10^{2}$ (21.4)	$9.0\text{x}10^{2}$ (19.2)	$2.2\text{x}10^{2}$ (10.0)	$1.8\text{x}10^{2}$ (4.3)	$1.0\text{x}10^{0}$ (0.1)	$2.4\text{x}10^{0}$ (0.3)
$\int_x > Fe$	$2.8\text{x}10^{3}$ (73.2)	$3.7\text{x}10^{3}$ (79.6)	$6.2\text{x}10^{2}$ (27.6)	$8.3\text{x}10^{2}$ (19.4)	$3.68\text{x}10^{1}$ (4.9)	$8.44\text{x}10^{1}$ (10.1)
$\int_x FeCO_3$	---	---	$1.4\text{x}10^{3}$ (60.0)	$3.2\text{x}10^{3}$ (74.9)	0 (0)	$2.35\text{x}10^{2}$ (28.0)
$\int_x FeS$	$2.1\text{x}10^{2}$ (5.4)	$5.8\text{x}10^{1}$ (1.2)	$5.4\text{x}10^{1}$ (2.4)	$6.0\text{x}10^{1}$ (1.4)	$6.80\ \text{x}10^{2}$ (90.9)	$4.15\ \text{x}10^{2}$ (49.5)
$\int_x Fe_{tot}^{red}$	$3.8\text{x}10^{3}$	$4.7\text{x}10^{3}$	$2.2\text{x}10^{3}$	$4.3\text{x}10^{3}$	$7.48\ \text{x}10^{2}$	$8.38\ \text{x}10^{2}$
[d] $\int_x R_{resp}(O_2)$	$1.0\text{x}10^{-6}$ (47.7)	$2.0\text{x}10^{-7}$ (14.4)	$2.1\text{x}10^{-7}$ (15.0)	$6.8\text{x}10^{-7}$ (35.5)	$5.9\text{x}10^{-6}$ (32.2)	$2.1\text{x}10^{-6}$ (11.3)
[e] $\int_x R_{resp}(FeOx)$	$9.1\text{x}10^{-7}$	$9.1\text{x}10^{-7}$	$9.1\text{x}10^{-7}$	$2.3\text{x}10^{-6}$	$5.8\text{x}10^{-7}$	$3.8\text{x}10^{-6}$

[a] "P,E" refers to the baseline simulation, "S" to inclusion of secondary reactions, "M" to mineral precipitation/dissolution reactions, and "B" to explicit descriptions of microbial functional groups. See Table 2.1 for the reactions part of each set.

[b] "*FulI"* refers to the complete set of reactions in Wang and Van Cappellen (1996), "*Full - S*" to the removal of the secondary reactions.

[c] Note that, following the work of Watson et al. (2005), precipitation/dissolution of FeS is in the primary reaction network "P,E" even

before additional precipitation/dissolution reactions are added in “P,E,S,M”

[d] Organic matter degradation coupled to oxygen.

[e] Organic matter degradation coupled to iron hydroxides

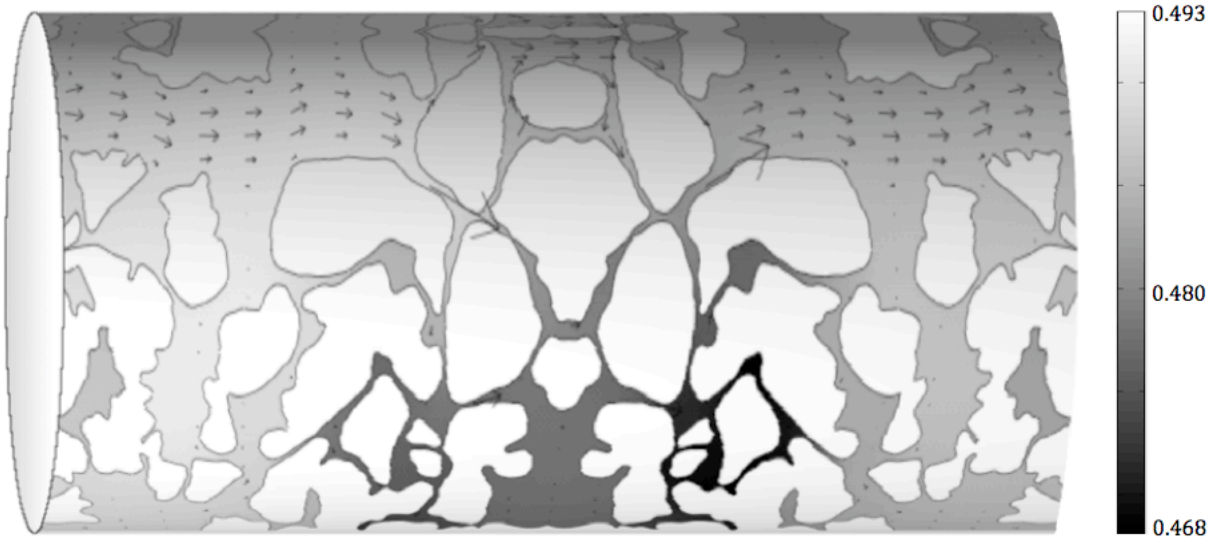

Figure 2.1: Porous media represented as a cylinder by folding the top and bottom of the domain together. Modeled acetate concentration in the pore scale simulation (μM) is depicted in the shaded regions. Arrows represent fluid flow with arrow size proportional to the velocity in the pores.

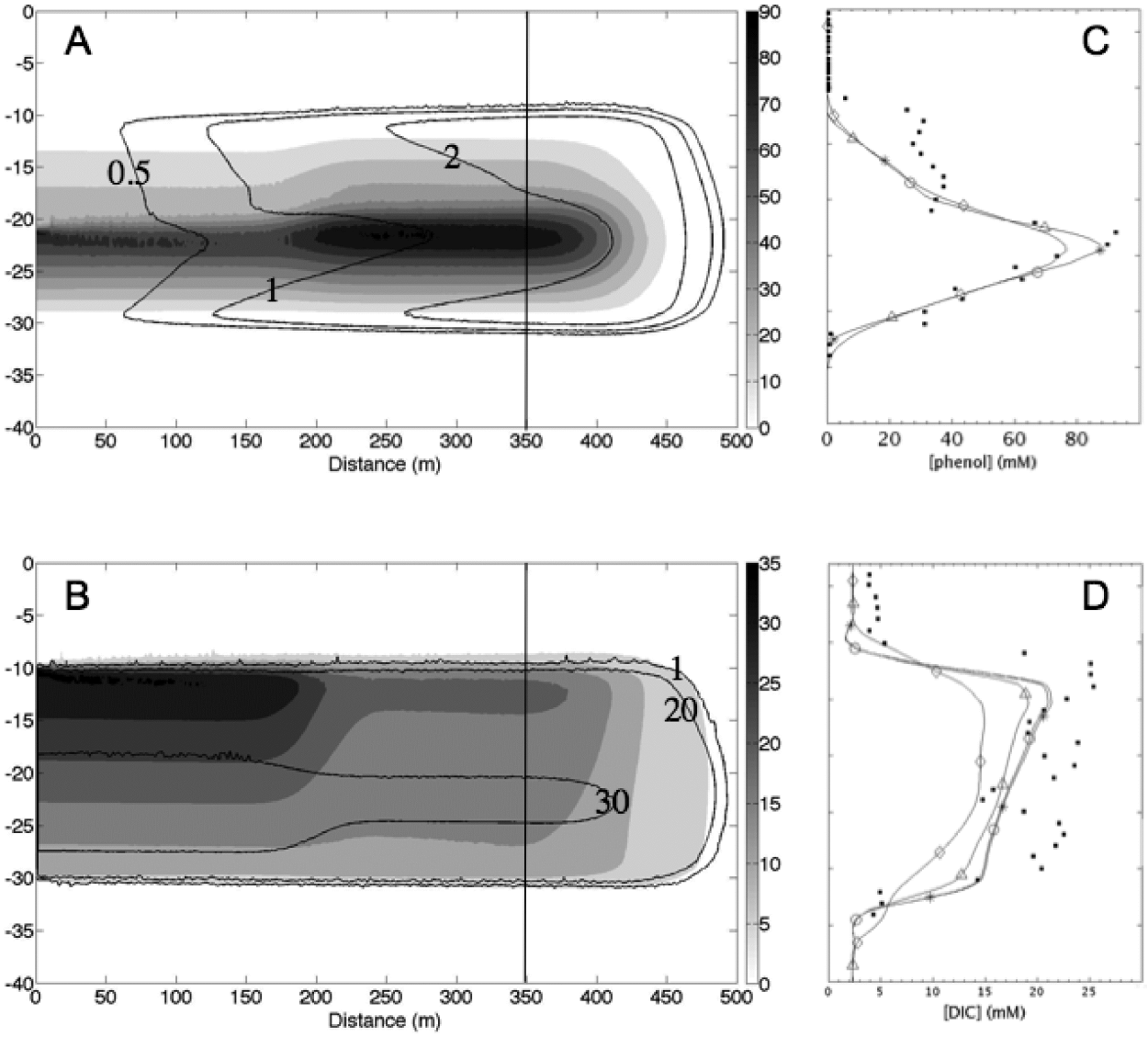

Figure 2.2: (A) Contaminant plume after 47 years. Shaded regions in panels (A) and (B) show phenol and DIC in mM, respectively, while the contour lines denote acetate (mM, A) and H_2 concentrations (nM, B), respectively. The vertical bar indicates the position of a well for which panels (C) and (D) show a comparison of the measurements represented by filled circles (dots; Thornton et al. 2001b) and the model results (lines). For panels (C) and (D), open circles denote reaction network P,E; asterisks denote P,E,S; triangles denote P,E,S,M; and diamonds denote P,E,S,M,B.

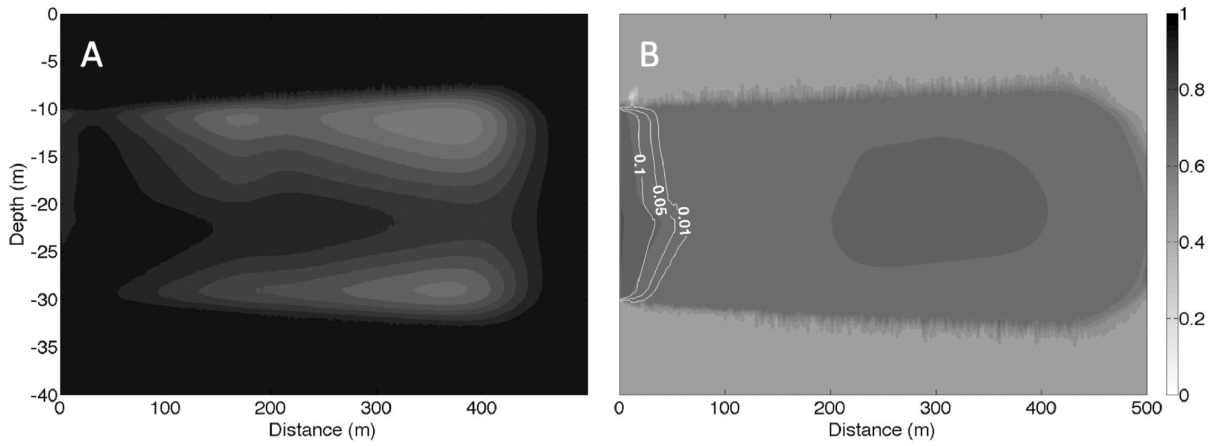

Figure 2.3: Bacterial nitrogen and thermodynamic limitations for phenol fermenting (panel A) and H_2 oxidizing bacteria (panel B). Filled regions indicate the value of the thermodynamic constraint, computed as $\sum R_i F_{thd,i} \Big/ \sum R_i$, where R_i denote the relevant kinetic reaction rates, B^*F_{kin} (P3 and P4 in panel A, P5, P6, P7, and P8 in panel B) and $F_{thd,i}$ the corresponding thermodynamic factors. The contours (panel b) represent the concentration of available ammonium (mM), indicating that in most of the plume, NH_4^+ requirements are met only via recycling of biomass.

CHAPTER 3

METHANOGENSIS IN FRESHWATER COASTAL SEDIMENTS: APPROACHES TO QUANTIFY RATES OF ORGANIC MATTER BREAKDOWN[3]

[3] Eric Lee King, Katherine Segarra, Vladimir Samarkin, Samantha Joye, and Christof Meile. To be submitted to *Biogeosciences*

Abstract

Methane is an important greenhouse gas that is produced through the decomposition of organic matter in many productive systems, including coastal freshwater sediments. To elucidate microbially mediated carbon cycling in anoxic sediments, process rates detailing organic matter breakdown were parameterized and determined. A set of reactions was developed describing the hydrolysis and fermentation of organic matter through terminal metabolic processes and was used to quantify rates of processes involved in organic matter breakdown. In particular, reaction rates that are not easily accessible through direct measurement were determined. Two complimentary approaches, parameter optimization employing differential evolution and a novel network analysis based on elementary flux mode analysis, were used. Since the two approaches rely on different available data types, this exercise permitted a comparison of independent methods to determine process rates in the sediment. Results show that the methodologies differ significantly in some of the rates predicted, highlighting the need for descriptive reaction kinetics when evaluating organic matter breakdown.

1. Introduction

Microorganisms obtain energy from the breakdown of organic matter, a process in which biopolymers are broken down into monomers by microbially catalyzed hydrolytic reactions (Wetzel, 1992). In anaerobic environments, fermentative reactions transform the monomers into low molecular weight substances such as volatile fatty acids (VFA) and amino acids, which are then used by microorganisms to produce carbon dioxide (Megonigal, 2004). When external terminal electron acceptors (TEA) are low, methane is produced, a potent greenhouse estimated to account for ~20% of the total greenhouse gas forcings (IPCC, 2001).

Freshwater wetlands are natural sources of atmospheric methane (Aselmann and Crutzen, 1989), motivating this study of the breakdown of organic matter in anoxic freshwater marsh sediments. In such a setting, organic matter is broken down into carbon dioxide, H_2, acetate, and other volatile fatty acids such as lactate, formate, and isobutyrate. Carbon dioxide can be incorporated into cell biomass, converted to acetate through homoacetogenesis (Drake, 1995), or transformed into methane through hydrogenotrophic methanogenesis. Acetate can be used to produce methane through acetoclastic methanogenesis (Schink, 1997). Alternatively, it can be oxidized to inorganic carbon, which can then be potentially utilized by hydrogenotrophic methanotrophs to indirectly produce methane (Zinder and Koch, 1984). Volatile fatty acids (VFA) can be utilized subsequently to produce inorganic carbon, acetate, or some directly into methane (Boone et al., 1989). Therefore, an understanding of methane production necessitates knowledge on a complex set of biochemical reactions.

Building on a detailed investigation of organic matter breakdown in freshwater sediments on the east coast of the United States (Segarra et al., 2013), we quantify benthic carbon cycling by mining measured radiotracer data and the accumulation or depletion of metabolites in slurry experiments for a site in coastal Georgia, which has been previously shown to have significant methane production from organic matter degradation (Weston et al., 2006a). In contrast to most studies (Phelps and Zeikus, 1984) that focus on the quantification of a single process (e.g. methanogenesis), we simultaneously analyze sequential and parallel pathways in the benthic carbon cycle. Two different approaches were developed. The first utilizes the global optimization approach differential evolution (DE; Storn and Price, 1997) to determine a set of kinetic parameters while the second characterizes all feasible network realizations using elementary flux mode analysis (EFMA) that are consistent with the observational data. These approaches both

elucidate the rates for the various processes involved in the conversion of organic macromolecules to CO_2 and CH_4.

2. Methods[4]

2.1 Sample collection

The study site was located at Hammersmith creek, a tidal freshwater creek, within the Georgia Coastal Ecosystems LTER (31°20'23.36" N, 81°29'05.00" W) domain. Sediment samples were collected from an unvegetated creek bank in January 2008. Forty cm long cores (7.5 cm diameter) were extracted, stored at *in situ* temperature, and processed within 36 hours. The 2-12 cm region of the cores was sectioned for analysis in slurry and radiotracer incubations. Please see Segarra et al. (2013) for a more detailed description of the site and sampling methods.

2.2 Slurry incubations

Sediment from the 2-12 cm region of the core was mixed with equal parts artificial porewater (Weston and Joye, 2005; Weston et al., 2006b) in anaerobic chambers. Incubations were run at approximately in situ temperature (20° C) for ~12.6 days and subsampled at 5 times over the incubations. Analysis of pore water constituents over the time series included CH_4, CO_2, acetate, alternative VFAs, H_2, and dissolved iron. For each subsample, the slurry bottles were shaken, with gas samples for H_2, CO_2, and CH_4 measurements made on the headspace. Dissolved organic carbon, VFAs, and dissolved Fe^{2+} measurements were conducted on the aqueous phase. CH_4 and CO_2 concentrations were determined through injection of 0.5 ml of headspace into a Shimadzu GC-14A with a Carbosphere® column, methanizer, and flame ionation detector. H_2

[4] E.L. King assisted in sample collection with lab work performed by K. Segarra and V. Samarkin

concentrations were determined using a reduction gas analyzer (Hoehler et al., 1994). An aqueous sample was filtered (0.2 μm filter) and Fe^{2+} determined. VFAs were determined through analysis on an HPLC by quantification of 2-nitrophenyl derivatives at three time points over the incubations.

2.3. Radiotracer incubations

Additional slurry incubations utilizing radiotracers were run in parallel to determine rates of hydrogenotrophic ($H^{14}CO_3^-$) and acetoclastic ($^{14}CH_3COOH$) methanogensis. 25 ml glass incubations tubes (Orcutt et al., 2005) were used to hold 10 ml of slurry at in situ temperature. Slurries were incubated for three days prior to addition of 5 μCi of tracer. Triplicate samples at time zero were killed before tracer was added. Samples were incubated for 36 hours. Activities were determined through addition of NaOH to halt activity and subsequent recovery of radioactive product through combustion and distillation (Orcutt et al., 2005). HPLC and a fraction collector were used to recover ^{14}C-acetate. Rates were determined by calculating the accumulation of product over time.

2.4 Reaction network

Organic matter breakdown reflects the transformation of particulate organic matter into a biodegradable dissolved organic matter pool (DOM, represented as $C_6H_{12}O_6$). The network is visualized in Figure 3.1 and represents the following reactions:

POM → DOM (1)

DOM is then broken down into low molecular weight chemicals, including acetate (Thauer et al., 1977) and volatile fatty acids (VFA).

$C_6H_{12}O_6 + 4\ H_2O \rightarrow 2\ CH_3COO^- + 4\ H_2 + 2\ HCO_3^- + 4\ H^+$ (2)

VFAs measured in the slurry experiments consisted of lactate, isobutyrate, and formate, with a molar ratio of 1.29 : 1 : 0.73; all other VFAs were below the detection limit. A weighted average of the individual reactions that produce VFAs (Boone et al., 1989; Megonigal, 2004):

$C_6H_{12}O_6 \rightarrow 2\ CH_3CHOHCOO^- + 2\ H^+$ (3.i)

$C_6H_{12}O_6 + 2\ H_2O \rightarrow (CH_3)_2CHCOO^- + 2\ HCO_3^- + 3\ H^+ + 2\ H_2$ (3.ii)

$C_6H_{12}O_6 + 2\ H_2O \rightarrow 2\ CH_3COO^- + 2\ HCOO^- + 4\ H^+ + 2\ H_2$ (3.iii)

was used to represent the VFA composition (1.29 * (3.i) + (3.ii) + 0.73*(3.iii)) / (1.29+1+0.73)):

$C_6H_{12}O_6 + 1.15\ H_2O \rightarrow 4.37\ C_{VFA} + 0.48\ CH_3COO^- + 1.15\ H_2 + 2.81\ H^+ + 0.66\ HCO_3^-$ (3)

where C_{VFA} denotes carbon atoms contained in VFA, represented as $CH_{1.6}O_{1.0}$. Methane production from VFAs follows Boone et al. (1989) for formate and accounts for methyl groups in lactate and isobutyrate:

$CH_3CHOHCOO^- + 1\ H_2O + H^+ \rightarrow CH_4 + 2\ CO_2 + 2\ H_2$ (4.i)

$(CH_3)_2CHCOO^- + 2\ H_2O + H^+ \rightarrow 2\ CH_4 + 2\ CO_2 + 2\ H_2$ (4.ii)

$4\ HCOO^- + 4\ H^+ \rightarrow CH_4 + 3\ CO_2 + 2\ H_2O$ (4.iii)

such that (1.29 * (4.i) + (4.ii) + 0.73*(4.iii)) / (1.29+1+0.73)):

$3.57\ C_{VFA} + 0.61\ H_2O + 1.73\ H^+ \rightarrow 1.33\ CH_4 + 1.52\ H_2 + 2.24\ CO_2$ (4)

Acetate production from VFAs is described for lactate and isobutyrate (Kotsyurbenko et al., 2004) only, as formate is not converted to acetate:

$(CH_3)_2CHCOO^- + 2\ H_2O \rightarrow 2\ CH_3COO^- + H^+ + 2H_2$ (5.i)

$CH_3CHOHCOO^- + 2\ H_2O \rightarrow CH_3COO^- + HCO_3^- + 2\ H_2 + H^+$ (5.ii)

Combining these reactions results in the following (1.29 * (5.i) + (5.ii) / (1.29+1)):

$2.70\ C_{VFA} + 1.52\ H_2O \rightarrow 1.19\ CH_3COO^- + 1.52\ H_2 + 0.33\ HCO_3^- + 0.75\ H^+$ (5)

Hydrogenotrophic and acetoclastic methanogenesis (Megonigal, 2004) are described by:

$4\ H_2 + CO_2 \rightarrow CH_4 + 2\ H_2O$ (6)

$CH_3COO^- + H^+ \rightarrow CO_2 + CH_4$ (7)

Acetate oxidation (Nusslein et al., 2001) is represented as:

$CH_3COO^- + H^+ + 2\ H_2O \rightarrow 2\ CO_2 + 4\ H_2$ (8)

DIC incorporation into biomass is given by:

$CO_2 \rightarrow$ Biomass (9)

Homoacetogenesis (Megonigal, 2004) is described by:

$4\ H_2 + 2\ CO_2 \rightarrow CH_3COO^- + H^+ + 2\ H_2O$ (10)

Two potential iron oxidation routes are investigated including through reduction of acetate (Lovley, 1991) or H_2 (Watson et al., 2005):

$CH_3COO^- + 8\ Fe(III) + 4\ H_2O \rightarrow 2\ HCO_3^- + 8\ Fe(II) + 9\ H^+$ (11)

$H_2 + 2\ Fe(III) + 4\ H^+ \rightarrow 4\ H_2O + 2\ Fe^{2+}$ (12)

Finally, acetate incorporation into biomass is given by:

$CH_3COO^- \rightarrow$ Biomass (13)

Note that the above representation of VFA consumption reactions somewhat arbitrarily assumes that the individual rates depend linearly on the substrate concentrations and that the rate constant for the consumption of the smaller formate molecule is 4 times faster than for the other VFAs.

2.5 Reaction Kinetics

The rate of change of each species is modeled as:

$$\frac{d\vec{C}}{dt} = \mathbf{S} \cdot \vec{R}_i \quad (14)$$

where $\mathbf{S}$ is the stoichiometric matrix and $\vec{R}_i$ denotes the rates of reactions 2-13. In DE, the

kinetic parameters within $\vec{R}_i$ are determined, whereas in EFMA steady state reaction rates (i.e. fluxes) are quantified.

2.6 Parameter Optimization using Differential Evolution

Reactions were described by zero or higher order kinetics, where for zero order, the rate for reaction *i* is defined as:

$$R_i = v_i \cdot \prod \frac{C_j}{\partial + C_j} \tag{15}$$

where v_i is the reaction rate, C_j is the concentration of each substrate j involved in the reaction, and ∂ is set to a small but positive concentration, 10^{-12} M, to effectively shut down the process in the absence of substrate. Higher order kinetics is described through either a 1st or 2nd order kinetic description for each reaction depending on the number of substrates and is formulated by:

$$R_i = v_i \cdot \prod C_j. \tag{16}$$

where C_j denotes the concentration of each substrate, j, involved in the reaction. Organic matter breakdown (Eqs, 2, 3) is formulated as a zero order reaction as its concentration is assumed to remain constant over the relatively short slurry incubation. For zero order kinetics, reactions 8 and 10 are combined into one net reaction that can proceed in either direction. All other rates/parameters are constrained to be non-negative.

The rational basis of the null space for the stoichiometric matrix involved in zero order kinetics, calculated from the reduced row echelon form, was computed in MATLAB in order to determine if any unique process rates existed (Hazewinkel, 1997). The null space is a set of vectors, x, such that $\mathbf{S}x = 0$. Each vector in x can be used to find columns in the stoichiometric matrix that is linearly dependent upon other columns. The null space therefore provided those

process rates that were linearly dependent upon other reactions, and thus a unique solution would not exist for that process rate.

Rate parameters were obtained via optimization to match the concentrations in the slurry time series, minimizing $\sum_{j,k}\left(\frac{C_{j,k}^{m}-C_{j,k}^{meas}}{\overline{C_j}}\right)^2$, where $C_{j,k}^{m}$ is the model calculated concentration of species *j* at time point *k*, $C_{j,k}^{meas}$ is the experimentally measured concentration at time point *k*, and $\overline{C_j}$ is the average of the experimentally determined concentrations in the slurry over time, used to ensure that species occurring at different concentration levels have a similar contribution to the objective function (OF). Minimization of the OF was accomplished using a differential evolution algorithm (Storn and Price, 1997), with the number of population members set to 50, the step size weight 0.85, the crossover frequency 1, the algorithm strategy left to default/classic, and the initial range of population members constrained between 0 and 10^4.

2.7 Elementary flux mode analysis

EFMA utilizes the stoichiometric matrix of a reaction network, information on the reversibility of reactions, and an assumption that non-terminal species are at steady state to identify each reaction pathway within the reaction network (see e.g. Schuster et al., 1994; Schuster et al., 2000). The program CellNetAnalyzer 2012.1 (Klamt et al., 2007) was used to determine the reaction pathways. Each pathway is assigned a relative weight between 0.1 and 1 (1 indicates a pathway is the only active pathway) in intervals of 0.1, with the constraint that the sum of the weights is 1. Each realization of a reaction network is represented by the combination of a minimum of 1 and a maximum of 10 reaction pathways, with all mathematical combinations of pathways analyzed.

To identify the realizations that are consistent with the observational data, which indicate methane formation from DIC, acetate, and alternative VFAs, only those that involved methane production via all three pathways were used from the millions of realizations determined above. EFMA only provides the relative magnitudes of reaction rates. To compare model results to observations, the measured rates of acetoclastic, hydrogenotrophic, and net methanogenesis were used as follows. First, volumetric reaction rates were determined by setting the computed flux for acetoclastic methanogenesis (MOG), hydrogenotrophic MOG, or total methane production to the measured rates, and all other modeled reaction rates were scaled accordingly. Then, when normalizing to acetoclastic or hydrogenotrophic MOG, only those realizations that led to methane production through hydrogenotrophic or acetoclastic MOG, respectively, to be within a standard deviation of the measured rates were retained. Alternatively, the sum of acetoclastic and hydrogenotrophic methanogenesis and methane production through alternative VFAs was normalized to CH_4 accumulation rates in the slurries. Those realizations that predicted both acetoclastic and hydrogenotrophic methanogenesis to be within one standard deviation were kept as networks that are consistent with the observational data.

Finally, to determine the impact of the change in chemical species concentrations over time observed in the slurries for EFMA, a separate reaction network was created which included additional sources and sinks for each species. The magnitude of the sources were related to the rate of change of each species over the time span of the slurries and reflected whether the concentrations increased or decreased over time.

3. Results/Discussion

3.1 Kinetic based reaction rates

For each of the transformation processes quantified in the breakdown of organic matter, two different rate laws were employed. For zero order kinetics, optimization of reaction parameters lead to an overall reasonable reproduction of the concentration time series measured in the slurry experiments (Fig. 3.3). Hydrogen concentrations were characterized by short residence times and hence are extremely sensitive to small changes in the rates, and model results reproduce the observed general increase over the duration of the incubations. Methane and dissolved iron species increased over time in the slurries whereas VFA concentration decreased. DIC demonstrated little change over time with only a slight decrease observed. Model results match these concentrations for CH_4, Fe^{2+}, VFAs, and DIC reasonably well (Fig. 3.3). However, discrepancies are apparent e.g. for acetate, where model results did not fit the observed decrease and subsequent increase in concentrations over time. This highlights one limitation of zero order kinetics when used to fit data that is non-linear in appearance. Another limitation is the inability to solve for unique process rates as a result of utilizing an underdetermined network, as seen here with 12 process rates to solve for and only 6 unknowns (the constant rate of change for the measured chemicals). Null space analysis of the stoichiometric matrix reveals that each process rate can be expressed as a linear combination of other rates. Therefore, an infinite set of the process rates resulting in the same net rates for each species observed in Fig. 3.3 exists. This limits the ability of this technique to elucidate the rates of the underlying processes involved in OM breakdown.

Some species concentrations clearly do not exhibit a linear change in concentration over time (e.g. acetate, Fig. 3.3), indicating that consumption or production rates change over time.

This leads to the use of higher order (concentration dependent) kinetic descriptions for the process rates. Rate parameters were determined for each reaction and average rates along with their standard deviations (as a measure of rate variation over time) were calculated (Table 3.1, Fig. 3.1). Objective functions obtained from higher order and zero order kinetics are within 10% of each other, indicating that the overall fit of the model concentrations to the slurry data are comparable. However, concentration-dependent rate expressions lead to changes in some species concentrations that more nearly fit the data (Fig. 3.3). For example, estimated acetate concentration decreased to match the concentration observed at the 2nd time point, but unlike zero order kinetics, do not continue to decrease but rather level off. Net rates for methane and DIC are virtually indistinguishable from zero order kinetics, and dissolved iron species are similar with slightly more Fe^{2+} production predicted from higher order kinetics. H_2 dynamics demonstrate a relatively quick initial increase in concentration compared to the linear increase predicted from zero order kinetics. VFA concentrations show a significant difference between zero and concentration dependent kinetics. While the objective function for the VFAs are within 15% of each other, higher order kinetics predicts a quick decrease in the concentration followed by a leveling off compared to the constant decrease predicted from zero order kinetics. The description of the reaction kinetics can have a significant effect on the concentrations predicted, while still fitting the observational data comparably.

3.2 EFMA derived rates

EFMA analysis resulted in 31 unique pathways (modes). Each pathway can be thought of as a group of organisms performing a subsection of the total reaction network; e.g. one pathway involves organic matter degradation to acetate, which is then utilized in acetoclastic

methanogenesis (i.e. reactions 2, 6, and 8 in Fig. 3.2). Another pathway involves OM degradation to acetate, H_2, and DIC, which are then used in iron reduction and DIC incorporation into biomass (i.e. reactions 2, 9, 11, and 12). Combinations of these pathways, considering a minimum contribution of at least 10% to overall metabolic rates, can then represent the totality of organic matter degradation and terminal metabolism occurring. This results in a determination of approximately 500 million network "realizations". Only accepting those realizations where methane production occurs through all of the three possible pathways (i.e. from acetate, alternative VFAs, and H_2), consistent with slurry data, removes about 35% of the realizations and lowers the total to 331,324,876. The fluxes from these realizations were then translated into rates by normalization to either hydrogenotrophic or acetoclastic MOG, or total methane production. Ultimately, this reduced the realizations consistent with the measurements, to 7,394,356, 11,617,237, and 6,747,082 respectively.

While the above procedure does not identify a unique set of process rates, the range of most rates is constrained to a relatively narrow range (Fig. 3.4). For example, reactions are consistently predicted to have an inner quartile range within a factor of 2-3 of the median. Notably, the rates constrained by matching any of the three methane production rates outlined above provided similar results (Fig. 3.4), except that normalization to hydrogenotrophic methanogenesis gave rates with an inner quartile range approximately 30-60% less than the other normalization techniques. This may occur because the standard deviation of the radiotracer acetoclastic MOG rate is smaller than that for hydrogenotrophic MOG. Therefore, when matching rates of acetoclastic MOG, a tighter selection of realizations is performed compared to when matching hydrogenotrophic MOG, evidenced by the approximately 4 million less realizations returned when normalizing to hydrogenotrophic MOG.

EFMA assumes steady state conditions, which contrasts with the observed concentration changes in the slurry experiments. Thus, the impact of the changes in pool sizes determined from slurry experiments was assessed. While the number of possible realizations increased, results showed that this uncertainty does not have a significant impact on the process rates depicted in Fig. 3.4 (results not shown).

3.3 Comparison

Comparison of the EFMA derived rates to results from higher order kinetics (Figures 3.1 and 3.2; Table 3.1) show both differences and similarities in the rates predicted. Acetoclastic and hydrogenotrophic MOG are about 2-2.5 times higher in EFMA. EFMA analysis uses radiotracer measurements of methanogenic processes to constrain the rates, while the parameter optimization approach only utilized concentration changes over time. It is therefore of note that the slurry derived rates are consistent with radiotracer measurements. Similarly, rates for VFA usage in methane production from EFMA and optimization approach fall within a factor of two of each other with larger rates predicted in higher order kinetics. Therefore, the methane production rates are consistent between network descriptions.

Organic matter breakdown into VFAs is also consistent between EFMA and optimization approaches, falling within about a factor of 3 of each other. A difference however is seen in the rates predicted for organic matter breakdown into acetate, DIC, and H_2. While EFMA predicts this rate to be less significant than VFA formation, higher order kinetics determines a rate that is many orders of magnitude less in importance. However, since the reaction describing alternative VFA formation also involves production of acetate (Eq. 3), albeit to a lesser extent, this can shift the overall importance of these two reactions while still producing acetate, H_2, and DIC. VFA

production from OM and subsequent acetate formation from the VFAs through higher order kinetics is 3-5 times lower than predicted from EFMA. The net rate differential between homoacetogenesis and acetate oxidation favors acetate production in higher order kinetics, whereas acetate oxidation is indicated by EFMA.

Iron reduction through acetate oxidation is predicted to be of little importance in the optimization approach compared to iron reduction from H_2. A similar pattern is seen in the EFMA results, with iron reduction from acetate 5-10 times less than the rate predicted from H_2. However, the net rates producing dissolved iron species is about 2-3 times less in the optimization approach versus EFMA derived rates. This is because the former match slurry Fe^{2+} concentrations over time, while the rates predicted from EFMA are not constrained by such data. Barring significant iron sulfide or carbonate precipitation, EFMA thus over predicts dissolved iron accumulation and provides an outlet for increased levels of OM breakdown. This difference in iron reduction rates, but similarity in methane production rates is mirrored in estimates of EFMA-based OM breakdown rates, which exceed those obtained by parameter optimization.

Similarities and differences between rates obtained from the two techniques can also be assessed via rank correlation (Fig. 3.5). Many of the rates between the two methods are dissimilar (Table 3.1). The relative importance of acetoclastic methanogenesis, CO_2 incorporation into biomass, and iron reduction through H_2 is similar as is organic matter degradation into VFAs and subsequently its utilization to produce biomass. Organic matter degradation to acetate and use in iron reduction also fall near the 1:1 line (Fig 3.5). Homoacetogenesis and hydrogenotrophic methanogenesis are ranked higher in the optimization approach whereas acetate incorporation into biomass and acetate oxidation is more significant in the EFMA results, consistent with the large differences seen in these rates.

Measurements in similar freshwater systems for many of the intermediate reactions depicted in Figs 3.1 and 3.2 are sparse. While methane production rate data are relatively abundant, other process rates in comparable systems are not. Rates of hydrogenotrophic methanogenesis obtained from higher order kinetics are generally 3-10 times lower than those rates measured in freshwater lakes at similar temperatures (Zeikus and Winfrey, 1976). However, they are consistent with the range of rates obtained in a freshwater lake by Kelly and Chynoweth (1981). Rates predicted from the optimization method are also consistent with the radiotracer rates measured in these slurries, which are used to parameterize the model subjected to EFMA analysis. For homoacetogenesis, rates obtained from higher order kinetics are about an order of magnitude lower than what is measured in anoxic, profundal, and littoral lake sediment (Lovley and Klug, 1983; Phelps and Zeikus, 1984).

4. Conclusions

Two complimentary, yet fundamentally different techniques were utilized to predict rates of organic matter breakdown in freshwater sediments. These methodologies provide alternative ways to determine process rates based upon the different types of data available. One technique utilizes species concentrations over time (DE), while the other technique requires knowledge of radiotracer-based rates for methanogenesis (EFMA) and to our knowledge is the first time an analysis based on the topology of the reaction network has been applied to quantify rates of biogeochemical reactions in sediments. Notably, even though they use different data, many rates, such as methane production rates are consistent between the methods.

Results from zero and higher order kinetics matched the slurry species concentrations over time reasonably well. However, the time course (i.e. linear vs. non-linear between zero-

order and DE respectively) of species concentrations can differ significantly. Although EFMA utilizes the same reaction network description of OM breakdown, several process rates obtained from EFMA can differ significantly compared to higher order kinetics. These results highlight the critical role that the description of the reaction kinetics utilized plays when estimating the rates underlying organic matter breakdown.

Acknowledgement: This work was supported by the National Science Foundation via award DEB-0717189 to SBJ and CM.

References

Aselmann, I., and Crutzen, P. J.: Global Distribution of Natural Fresh-Water Wetlands and Rice Paddies, Their Net Primary Productivity, Seasonality and Possible Methane Emissions, J Atmos Chem, 8, 307-358, 1989.

Boone, D. R., Johnson, R. L., and Liu, Y.: Diffusion of the Interspecies Electron Carriers H_2 and Formate in Methanogenic Ecosystems and Its Implications in the Measurement of K_m for H_2 or Formate Uptake, Appl Environ Microb, 55, 1735-1741, 1989.

Drake, H. L.: Acetogenesis, Acetogenic Bacteria, and the Acetyl-CoA "Wood/Ljungdahl" Pathway: Past and Current Perspectives, in: Acetogenesis, edited by: Drake, H. L., Chapman and Hall, New York, 3-60, 1995.

Hazewinkel, M.: Encyclopaedia of mathematics. Supplement, Kluwer Academic Publishers, Dordrecht, Boston, 1997.

Hoehler, T. M., Alperin, M. J., Albert, D. B., and Martens, C. S.: Field and laboratory studies of methane oxidation in an anoxic marine sediment: Evidence for a methanogen-sulfate reducer consortium, Global Biogeochem Cy, 8, 451-463, 1994.

IPCC: Climate Change 2001: The Scientific Basis., Cambridge UK and New York, NY USA, 2001.

Kelly, C. A., and Chynoweth, D. P.: The Contributions of Temperature and of the Input of Organic-Matter in Controlling Rates of Sediment Methanogenesis, Limnol Oceanogr, 26, 891-897, 1981.

Klamt, S., Saez-Rodriguez, J., and Gilles, E. D.: Structural and functional analysis of cellular networks with CellNetAnalyzer, Bmc Syst Biol, 1, 2007.

Kotsyurbenko, O. R., Chin, K. J., Glagolev, M. V., Stubner, S., Simankova, M. V., Nozhevnikova, A. N., and Conrad, R.: Acetoclastic and hydrogenotrophic methane production and methanogenic populations in an acidic West-Siberian peat bog, Environ Microbiol, 6, 1159-1173, 2004.

Lovley, D. R., and Klug, M. J.: Methanogenesis from Methanol and Methylamines and Acetogenesis from Hydrogen and Carbon-Dioxide in the Sediments of a Eutrophic Lake, Appl Environ Microb, 45, 1310-1315, 1983.

Lovley, D. R.: Dissimilatory Fe(III) and Mn (IV) reduction, Microbiol Rev, 55, 259-287, 1991.

Megonigal, J. P., Hines, M.E., and Visscher, P.T.: Anaerobic metabolism: linkages to trace gases and aerobic processes., Elsevier-Pergamon, In: Schlesinger, W. H., (Ed.), Treatise on Geochemistry, Oxford, UK, 2004.

Nusslein, B., Chin, K. J., Eckert, W., and Conrad, R.: Evidence for anaerobic syntrophic acetate oxidation during methane production in the profundal sediment of subtropical Lake Kinneret (Israel), Environ Microbiol, 3, 460-470, 2001.

Orcutt, B., Boetius, A., Elvert, M., Samarkin, V., and Joye, S.: Molecular biogeochemistry of sulfate reduction, methanogenesis and the anaerobic oxidation of methane at Gulf of Mexico cold seeps, Geochim Cosmochim Ac, 69, 4267-4281, 2005.

Phelps, T. J., and Zeikus, J. G.: Influence of Ph on Terminal Carbon Metabolism in Anoxic Sediments from a Mildly Acidic Lake, Appl Environ Microb, 48, 1088-1095, 1984.

Schink, B.: Energetics of syntrophic cooperation in methanogenic degradation, Microbiol Mol Biol R, 61, 262-280, 1997.

Schuster, S., Hilgetag, C., and Fell, D.: Detecting elementary modes of functioning in metabolic networks, Mod Tr Biothermokin, 3, 103-105, 1994.

Schuster, S., Fell, D. A., and Dandekar, T.: A general definition of metabolic pathways useful for systematic organization and analysis of complex metabolic networks, Nat Biotechnol, 18, 326-332, 2000.

Segarra, K. E. A., Samarkin, V., King, E. L., Meile, C., and Joye, S.: Seasonal variations of methane fluxes from an unvegetated tidal freshwater mudflat (Hammersmith Creek, GA), Biogeochemistry, 10.1007/s10533-013-9840-6, 2013.

Storn, R., and Price, K.: Differential evolution - A simple and efficient heuristic for global optimization over continuous spaces, J Global Optim, 11, 341-359, 1997.

Thauer, R. K., Jungermann, K., and Decker, K.: Energy conservation in chemotrophic anaerobic bacteria, Bacteriol Rev, 41, 100-180, 1977.

Watson, I. A., Oswald, S. E., Banwart, S. A., Crouch, R. S., and Thornton, S. F.: Modeling the dynamics of fermentation and respiratory processes in a groundwater plume of phenolic contaminants interpreted from laboratory- to field-scale, Environ Sci Technol, 39, 8829-8839, 2005.

Weston, N. B., and Joye, S. B.: Temperature-driven decoupling of key phases of organic carbon degradation in marine sediments, PNAS, 102, 17036-17040, 2005.

Weston, N. B., Dixon, R. E., and Joye, S. B.: Ramifications of increased salinity in tidal freshwater sediments: Geochemistry and microbial pathways of organic matter mineralization, J Geophys Res-Biogeo, 111, G01009, 2006a.

Weston, N. B., Porubsky, W. P., Samarkin, V. A., Erickson, M., Macavoy, S. E., and Joye, S. B.: Porewater stoichiometry of terminal metabolic products, sulfate, and dissolved organic carbon and nitrogen in estuarine intertidal creek-bank sediments, Biogeochemistry, 77, 375-408, 2006b.

Wetzel, R. G.: Gradient-Dominated Ecosystems - Sources and Regulatory Functions of Dissolved Organic-Matter in Fresh-Water Ecosystems, Hydrobiologia, 229, 181-198, 1992.

Zeikus, J. G., and Winfrey, M. R.: Temperature Limitation of Methanogenesis in Aquatic Sediments, Appl Environ Microb, 31, 99-107, 1976.

Zinder, S. H., and Koch, M.: Non-Aceticlastic Methanogenesis from Acetate - Acetate Oxidation by a Thermophilic Syntrophic Coculture, Arch Microbiol, 138, 263-272, 1984.

Table 3.1: Model determined rates from optimization technique and median rates from EFMA. All rates and standard deviations are given in M day^{-1}. Reaction labels follow the equation numbering provided in the methods and Figure 3.1. "Ac", "Hyd", and "Total" refer to those rates from EFMA that were normalized to acetoclastic MOG, hydrogenotrophic MOG, and total methane production rates respectively.

Parameter optimization (higher order kinetics)				**EFMA Rates**		
Reaction	v_i	Avg. rate	Std. dev	Ac	Hyd	Total
2	$4{\cdot}10^{-15}$ M day^{-1}	$4{\cdot}10^{-15}$	$7{\cdot}10^{-30}$	$9{\cdot}10^{-6}$	$7{\cdot}10^{-6}$	$1{\cdot}10^{-5}$
3	$6{\cdot}10^{-6}$ M day^{-1}	$6{\cdot}10^{-6}$	0	$2{\cdot}10^{-5}$	$1{\cdot}10^{-5}$	$2{\cdot}10^{-5}$
4	$7{\cdot}10^{-1}$ day^{-1}	$9{\cdot}10^{-6}$	$1{\cdot}10^{-6}$	$4{\cdot}10^{-6}$	$4{\cdot}10^{-6}$	$7{\cdot}10^{-6}$
5	$5{\cdot}10^{-1}$ day^{-1}	$3{\cdot}10^{-6}$	$1{\cdot}10^{-6}$	$1{\cdot}10^{-5}$	$7{\cdot}10^{-6}$	$1{\cdot}10^{-5}$
6	$5{\cdot}10^{3}$ M^{-1} day^{-1}	$1{\cdot}10^{-6}$	$4{\cdot}10^{-8}$	$2{\cdot}10^{-6}$	$2{\cdot}10^{-6}$	$2{\cdot}10^{-6}$
7	$1{\cdot}10^{0}$ day^{-1}	$8{\cdot}10^{-6}$	$2{\cdot}10^{-6}$	$2{\cdot}10^{-5}$	$2{\cdot}10^{-5}$	$3{\cdot}10^{-5}$
8	$3{\cdot}10^{-9}$ day^{-1}	$2{\cdot}10^{-14}$	$4{\cdot}10^{-15}$	$2{\cdot}10^{-5}$	$1{\cdot}10^{-5}$	$3{\cdot}10^{-5}$
9	$4{\cdot}10^{-2}$ day^{-1}	$4{\cdot}10^{-5}$	$2{\cdot}10^{-6}$	$8{\cdot}10^{-5}$	$6{\cdot}10^{-5}$	$9{\cdot}10^{-5}$
10	$4{\cdot}10^{3}$ M^{-1} day^{-1}	$2{\cdot}10^{-7}$	$4{\cdot}10^{-8}$	0	0	0
11	$6{\cdot}10^{-10}$ day^{-1}	$4{\cdot}10^{-15}$	$8{\cdot}10^{-16}$	$8{\cdot}10^{-6}$	$6{\cdot}10^{-6}$	$1{\cdot}10^{-5}$
12	$4{\cdot}10^{2}$ day^{-1}	$2{\cdot}10^{-5}$	$3{\cdot}10^{-6}$	$5{\cdot}10^{-5}$	$4{\cdot}10^{-5}$	$6{\cdot}10^{-5}$
13	$1{\cdot}10^{-7}$ day^{-1}	$7{\cdot}10^{-13}$	$2{\cdot}10^{-13}$	$2{\cdot}10^{-5}$	$1{\cdot}10^{-5}$	$3{\cdot}10^{-5}$

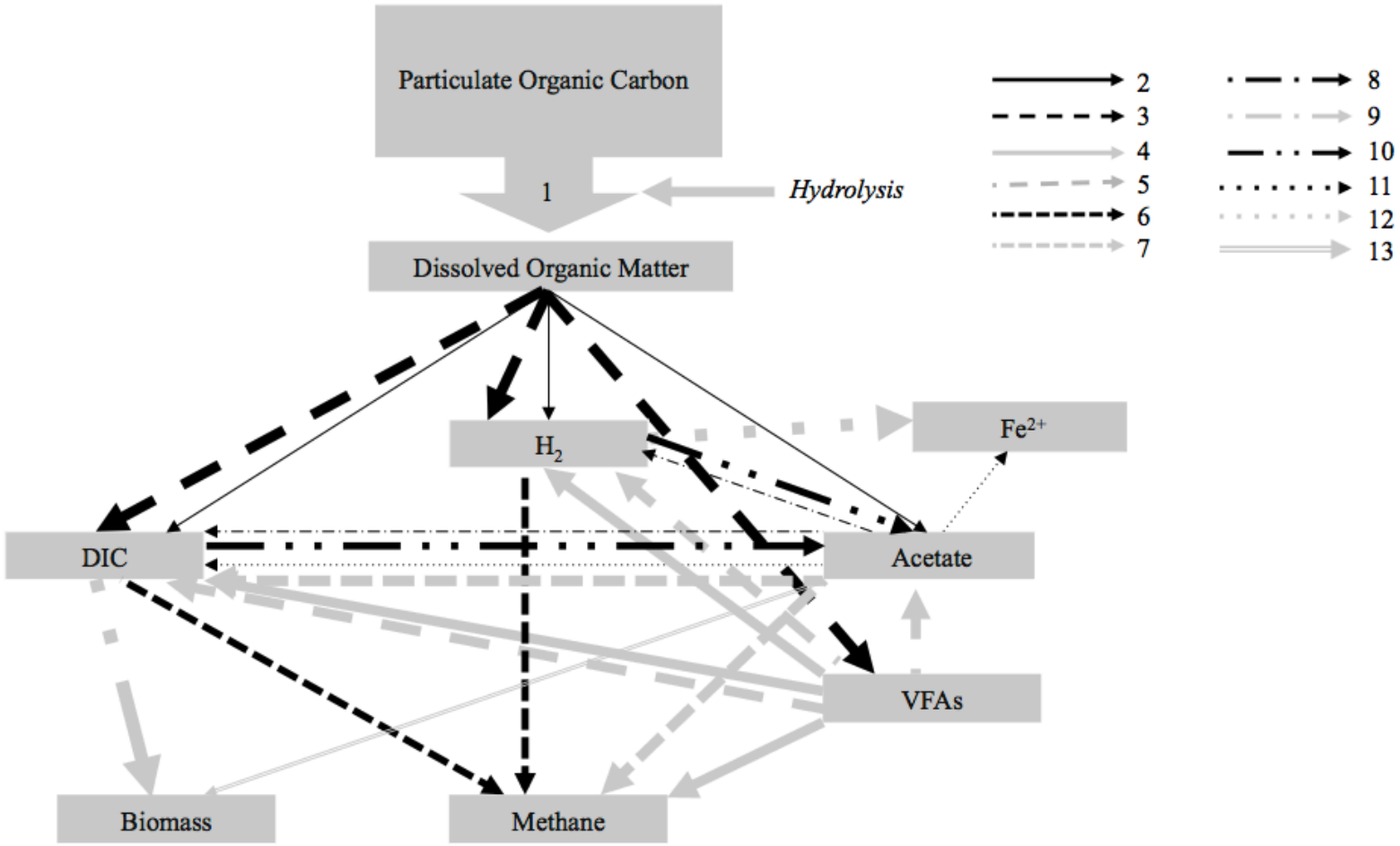

Figure 3.1. Organic matter breakdown rate estimates based on parameter optimization. Sizes of arrows represent the relative magnitude of the rates (Table 3.1). Numbers indicate the reactions detailed in the methods.

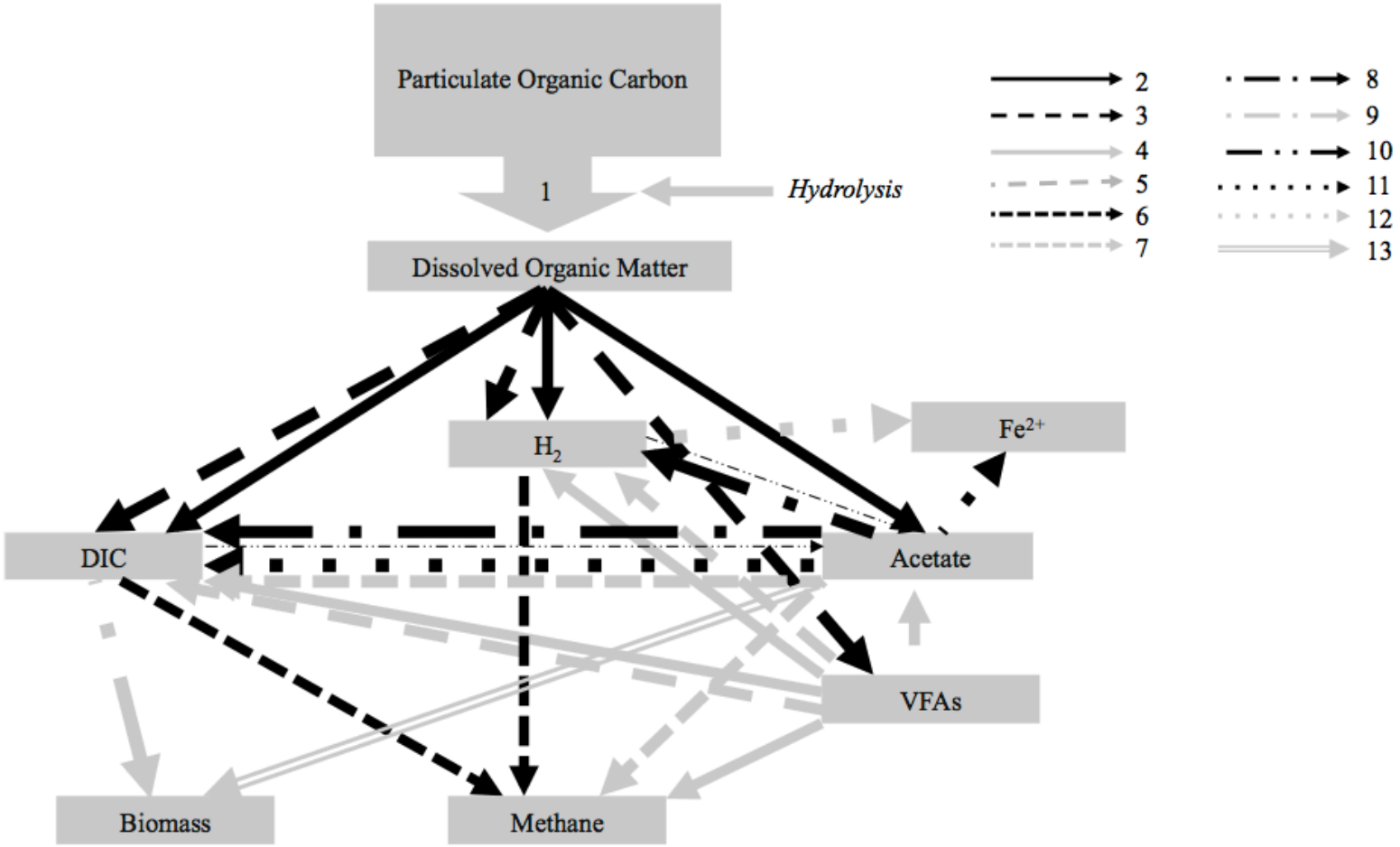

Figure 3.2. Organic matter breakdown rate estimates based on EFMA. See caption for Figure 3.1.

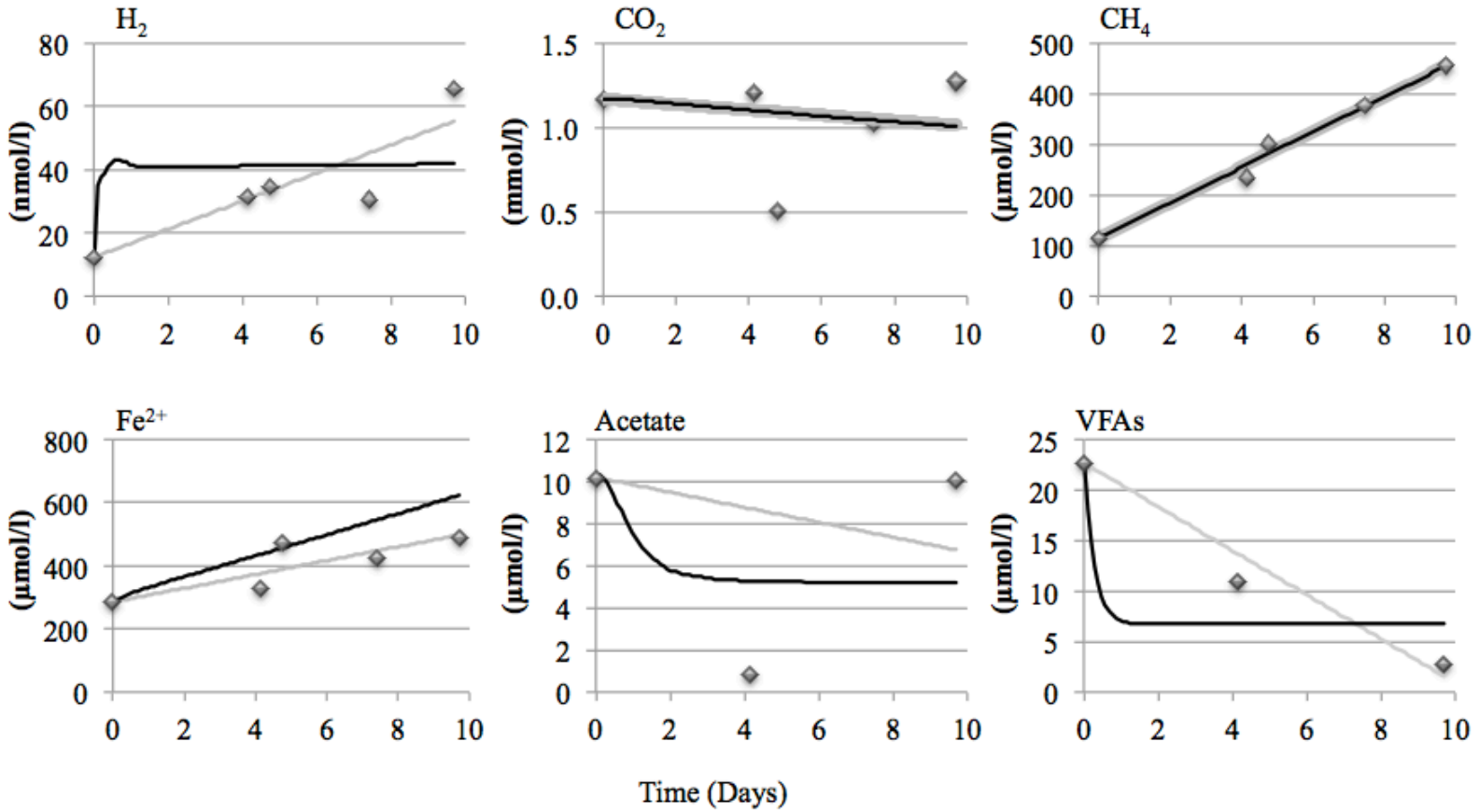

Figure 3.3: Results from zero order (solid grey line) and concentration-dependent reaction kinetics (solid black line) with experimental results (diamonds) for April 2008. VFAs refer to those present other than acetate as indicated in the methods and is quantified in µM carbons.

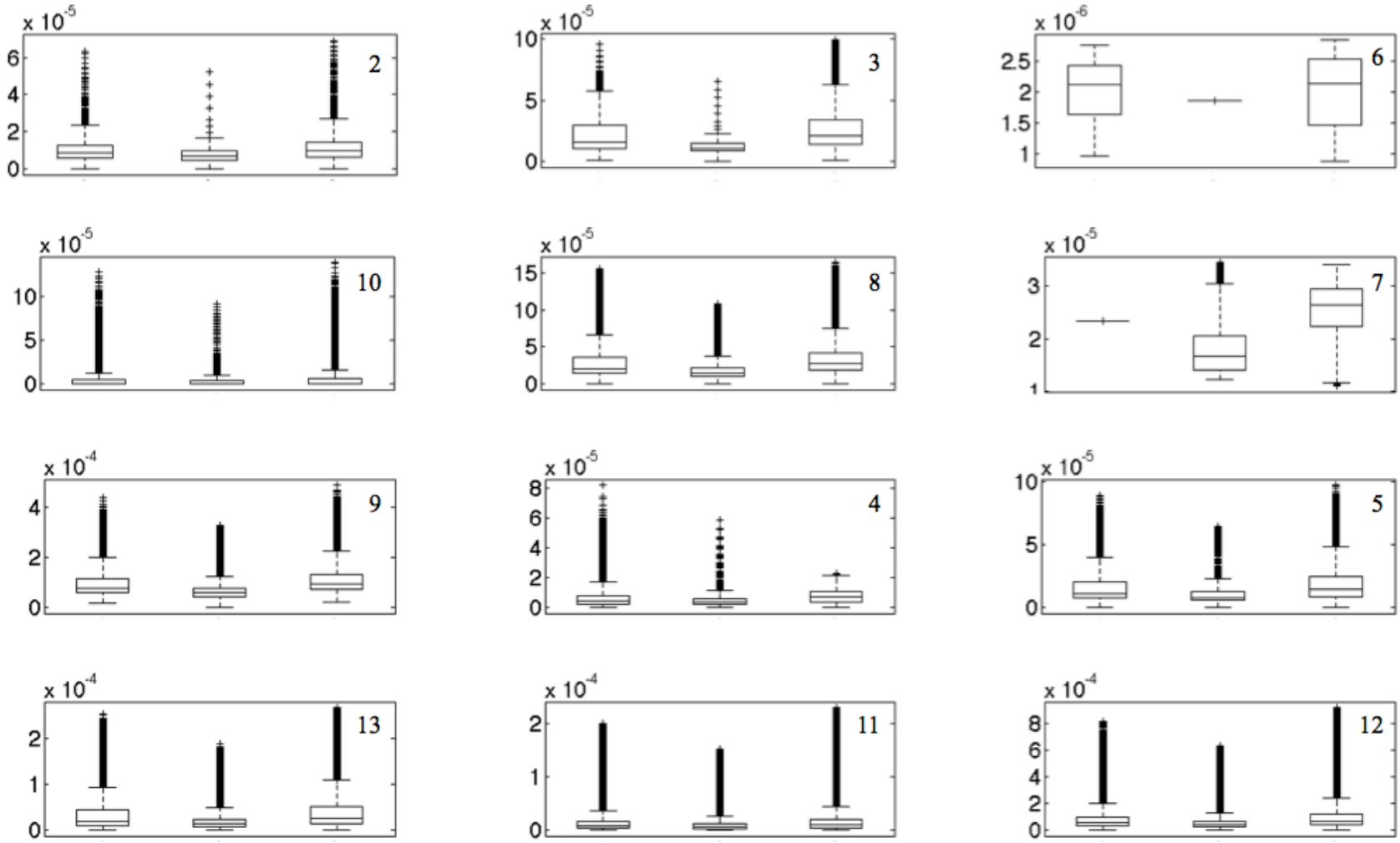

Figure 3.4: Boxplots depicting the range of reaction rates derived from EFMA (M day^{-1}). Realizations are normalized to measured acetoclastic methanogenesis (1st item in each plot), measured hydrogenotrophic methanogenesis (2nd item), and total methane

production in the slurries (3rd item); see methods for a detailed description. Plot numbering represents reaction numbers given in the methods. Rates with a single bar are imposed. On each box, the central mark is the median, the edges of the box are the 1st and 3rd quartiles, the whiskers extend 1.5 times the inner quartile range above and below the 1st and 3rd quartile, and outliers are given in black.

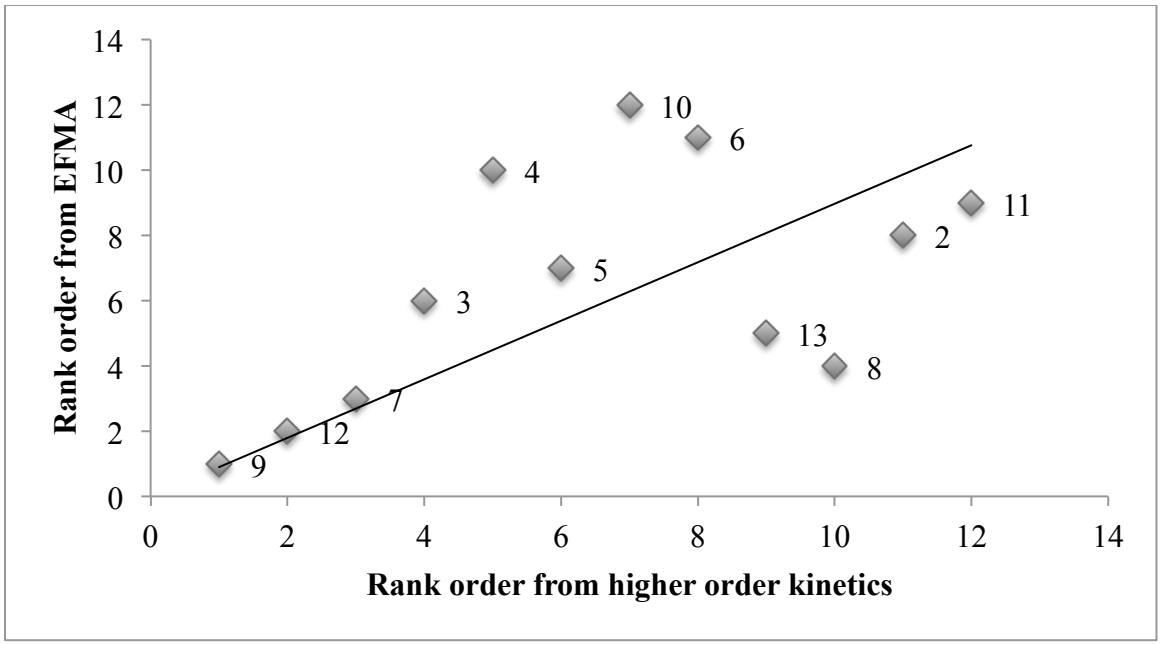

Figure 3.5: Rank correlation for each of the rates between EFMA and optimized kinetics. Labels indicate the reactions numbers from Fig. 3.1 and the methods. Low ranks refer to higher values for the rates. $R^2 = 0.11$ corresponds to the linear fit of the ranks to a line running through the origin.

CHAPTER 4

IN SILICO *GEOBACTER SULFURREDUCENS* METABOLISM AND ITS REPRESENTATION IN REACTIVE TRANSPORT MODELS[5]

[5] Eric Lee King, Kagan Tuncay, Peter Ortoleva, and Christof Meile. 2009. *Applied and Environmental Microbiology*. 75:83-92. Reprinted here with permission of the publisher.

Abstract

Microbial activity governs elemental cycling and the transformation of many anthropogenic substances in aqueous environments. Through the development of a dynamic cell model of the well characterized, versatile and abundant *Geobacter sulfurreducens*, we showed that a kinetic representation of key components of cell metabolism matched microbial growth dynamics observed in chemostat experiments under varying environmental conditions and led to results similar to those from a comprehensive flux balance model. Coupling the kinetic cell model to its environment by expressing substrate uptake rates depending on intra- and extracellular substrate concentrations, 2D reactive transport simulations of an aquifer were performed. They illustrated that a proper representation of growth efficiency as a function of substrate availability is a determining factor for the spatial distribution of microbial populations in a porous medium. It was shown that simplified model representations of microbial dynamics in the subsurface that only depended on extracellular conditions could be derived by properly parameterizing emerging properties of the kinetic cell model.

Introduction

Microbes control the breakdown of organic matter in low temperature subsurface environments. Their activities affect the physico-chemical nature of the local environment, drive elemental cycling, and determine the fate of many contaminants (9, 49). Effects can be direct (for example by altering the local chemical composition through the utilization of substrates and terminal electron acceptors for energy production and growth or co-metabolism) or indirect (for example by affecting the presence and chemical nature of solid iron phases, which determines sorption and co-precipitation of transition metals and contaminants) (4, 6, 17, 51). In addition,

hydrological factors such as groundwater flow patterns and velocities can impact cell metabolism through nutrient delivery, with possible feedbacks through bioclogging (46).

To predict how bacteria regulate their activity and grow *in situ*, it is necessary to quantitatively understand the complex and dynamic interactions between numerous concurrent biogeochemical processes involved, which requires the use of mathematical models. While subsurface reactive transport models generally contain a comparatively sound description of the physical transport processes (3, 34), they often do not explicitly account for the dynamics of microbial populations that mitigate the majority of biogeochemical processes (18, 48). When included, microbes are typically represented as functional groups, with growth dynamics depending linearly on substrate availability or following Monod kinetics (27, 38, 44), an approach that has been successful in describing geochemical contaminant plume dynamics (7). However, lacking a realistic representation of microbial metabolism, such models are limited in their capability of reflecting microbial dynamics and forecasting the response to changing environmental conditions, which restricts their predictive power at the macro-scale and usefulness, for example, in the assessment of conditions that optimize *in situ* bioremediation (22).

With the advent of genome sequencing, over the last decade the biological revolution has led to the characterization of cellular metabolic networks and to the development of mathematical models at the cell scale (41), ranging from descriptions of network topology (20, 45) to constraint-based models for different organisms (13, 33, 42) and fully kinetic approaches (e.g., (2, 30, 50)). Integration of such models of environmentally important groups of bacteria in reactive transport simulations would clearly benefit forecasting biogeochemical responses to changing macroscopic conditions. The γ-proteobacteria *Geobacteracea* constitute such an

abundant and environmentally important group in both pristine and contaminated sediment environments (22). *Geobacter* species are metabolically diverse and can grow with numerous electron donors and acceptors, including acetate or H_2, and Fe(III), fumarate, or malate, respectively (8, 23). They have been shown to be enriched when Fe(III) reduction was promoted in a petroleum contaminated sandy aquifer (39) and to mediate the reduction of U(VI) to U(IV) (25), converting the soluble form to the insoluble form and effectively removing the uranium from the groundwater (51). *Geobacter* shape biogeochemical cycling directly through their metabolic activity, as well as indirectly, such as via the effect of iron (hydro)oxide reduction on the motility of sorbed trace metals and on pH.

In this study, we present a kinetic cell model of *Geobacter sulfurreducens* metabolism and its application in the simulation of a subsurface contaminant plume with the goals (i) to assess the kinetic description of central cellular metabolism and the growth efficiencies emerging under a range of substrate conditions by a comparison to observational data, (ii) to quantify the sensitivity of model results to the parameterization of the enzymatic reactions of the TCA cycle and gluconeogenesis considered here, (iii) to compare and contrast different cell model approaches, (iv) to introduce a coupling approach between cell metabolic expressions and macroscopic reactive transport models and (v) to assess the potential and limits of macroscopic models that parameterize microscopic intracellular processes. Our cell model is validated against growth efficiencies obtained in chemostat experiments (12) and is compared to the flux balance (FB) model developed by Mahadevan et al. (26) who—based on an extensive genome analysis—used a constraint-based modeling approach to estimate steady state intracellular fluxes and metabolite exchange with the environment. To assess the role of microbial dynamics in the environment, an acetate plume is studied in a heterogeneous porous medium, for which

simulations with a full coupling between the environment and the cell model are contrasted with several simplified parameterizations, including commonly used Monod approximations.

Materials and Methods

Dynamic cell model

The dynamic cell model was implemented in the kinetic cell model simulator *Karyote* (31) which divides metabolic reactions into those that occur at equilibrium (fast reactions) or at a finite rate (slow reactions). For example, a single substrate isomerization reaction occurs by the fast formation of an enzyme-substrate complex ($S + E \xleftrightarrow{Q_f} ES$) followed by a slow dissociation ($ES \xleftrightarrow{k,kQ_s} P + E$), where Q_f is the equilibrium constant for the fast reaction and k and kQ_s are the backward and forward rate constants for the slow reactions, respectively.

Under typical natural subsurface conditions, the oxidation of acetate in *Geobacter*—initially activated through the combined action of acetate kinase and phosphate acetyltransferase (10)—is coupled to the reduction of Fe(III) (24), which is believed to take place on the extracellular membrane (21). Thus, the kinetic cell model encompassed the uptake of acetate and its incorporation into biomass via gluconeogenesis or its complete oxidation in the TCA cycle (10, 14) (Fig. 4.1). Two compartments—one extracellular and the other intracellular—were considered. The extracellular compartment accounted for species concentrations that represented environmental conditions while the intracellular one accounted for enzymatic reactions and resource allocation in cellular metabolism. Transformations were formulated as elementary reactions using mass action kinetics

$$\frac{dc_i}{dt} = \sum_l \upsilon_{li} \left(-k_l \prod_{j=1}^{N_p} c_j^{\upsilon_{lj}} + Q_l k_l \prod_{j=1}^{N_r} c_j^{-\upsilon_{lj}} \right), \qquad (1)$$

where c_i is the concentration of species i, Q_l is the equilibrium constant and k_l is the backward rate constant for reaction l, $\upsilon_{l.}$ denote stoichiometric coefficients, and $N_{p,r}$ are the number of products and reactants, respectively. Model parameters were derived from the literature and are given in Table 4.1. As the literature rarely contains enzymatic forward and reverse rate constants, model parameters were typically derived from enzyme turnover numbers, specific activities and substrate affinities. Details of the procedures and sources for model parameterization are given in the Appendix.

Sensitivity Analysis

The effect of the uncertainties in reaction rate parameters k and Q on the predicted growth efficiencies was quantified over a range of extracellular acetate concentrations by performing cell model simulations with perturbed parameter sets. Parameters k and Q were selected at random from a normal distribution centered at the literature-derived base value with a 5.7% standard deviation. Sensitivity coefficients s_j, which constitute a measure of the response of the growth efficiency to a change in parameter j, were determined via a multivariate linear regression using

$$g_{eff}^{i} - g_{eff}^{base} = \sum_{j} s_j \left(p_j^{i} - p_j^{base} \right) \Big/ p_j^{base} \qquad (2)$$

where g_{eff} is the growth efficiency, i indicates the i^{th} random realization, *base* denotes the baseline simulation, and j identifies the parameter p_j, set here to the backward and forward rate constants (k, kQ) and equilibrium constants for fast reactions (Q_f; see Appendix).

Cellular energy dynamics

Cellular energy dynamics were accounted for through reactions utilizing and producing AMP,

ADP and ATP. In addition to the energy used in the phosphorylation of acetate and pyruvate (Fig. 4.1, reactions 2 and 9), ATP is also produced through the reactions of the TCA cycle and consumed through cell growth and reactions required for cell maintenance according to

$$\frac{dATP}{dt} = 0.5 \cdot R_{TCA} \cdot \delta_T - (a \cdot R_g + R_m) \cdot \delta_D, \qquad (3)$$

where R_{TCA} is the overall rate of the TCA cycle, in which every acetate that cycles through will ultimately produce 0.5 ATP molecules (26). R_g is the growth rate, and a converts the rate of growth into ATP usage and is set to 19 mol_{ATP} $mol_{acetate}^{-1}$. It was based on ATP usage in the growth reaction of Mahadevan et al. (26) and modified to exclude the growth reactions explicitly accounted for in the reaction network (Fig. 4.1). R_m represents ATP consumption for cell maintenance, set to 0.45 $mmol_{ATP}$ g_{dw}^{-1} hr^{-1} (26), and δ_T and δ_D reflect the presence of ATP and ADP, respectively (1 if present, 0 otherwise). ATP, ADP, and AMP values were further constrained through a fast exchange of ATP + AMP = 2ADP that mimicked the balance between adenosine phosphates not modeled at the process level (29). Levels of other substances involved in intracellular energy regulation such as NAD/NADH, NADP/NADPH, CO_2 and phosphates (P_i, PP) were assumed to be constant (Fig. 4.1).

Acetate Uptake

Acetate uptake rates for the kinetic cell model were formulated using the four-state model for a facilitated diffusion carrier kinetics (2), in which the flux of acetate across the cell membrane, J_{ac} (mol L^{-1} s^{-1}), is described by

$$J_{ac} = \frac{A \cdot h \cdot (C_{in} - C_{out})}{V}, \qquad (4)$$

where C_{in} and C_{out} are the intracellular and extracellular concentrations (mol L^{-1}) of acetate,

respectively, V is the cellular volume (L), A is the cell surface area (dm^2), and h (dm s^{-1}) describes the transport of acetate across the cell membrane

$$h = \frac{(K_t)^2 Y}{K_t(K_t + C_{in} + C_{out}) + \alpha C_{in} C_{out}}, \qquad (5)$$

where K_t is a half saturation constant (10 μM) (12), Y is the maximum exchange of acetate (dm s^{-1}), and the symmetry index α is set to 0 for symmetric cross-membrane transport of acetate. Cell area was calculated based on *G. sulfurreducens* cell size (37) assuming a cylindrical shape. Maximum acetate exchange (Y = 1.20 x10^{-4} dm s^{-1}) was set to match the results from *Geobacter* chemostat experiments (12).

Growth efficiency was calculated from the acetate uptake flux and the flux of acetate through phosphoenolpyruvate (PEP), $g_{eff} = \alpha_{pep}\beta / J_{ac}$, where α_{pep} is the molar concentration of PEP produced per unit time and β describes the grams dry weight of biomass produced per mol of PEP created. β was calculated from a growth efficiency of 4.4 x10^{-3} g_{dw} $mmol_{acetate}^{-1}$ at a cell-specific growth rate μ of 0.06 hr^{-1} and an acetate flux to gluconeogenesis (Q) of 0.30 $mol_{acetate}$ g_{dw}^{-1} hr^{-1} (26). Taking into account the 2/3 acetate to PEP carbon ratio, $\beta = 2\mu / 3Q$ = 0.3 g_{dw} $mmol_{PEP}^{-1}$.

Flux Balance Model

Cellular metabolic rates under a range of acetate uptake fluxes were calculated using the flux balance model of *G. sulfurreducens* metabolism by Mahadevan et al. (26), which estimated intracellular fluxes and metabolite exchange with the environment for a given acetate uptake. The metabolic fluxes (reaction rates f) were sought that for a network described by a stoichiometric matrix S,

$$S \cdot f = 0 \qquad (6)$$

implying steady state. The fluxes were determined via optimizing a specific objective function, which is subjected to physiological constraints on the magnitude of the fluxes, *lower bound* $\leq f \leq$ *upper bound*. Maximization of biomass production rate was used as an objective function, which had been shown to lead to results in agreement with experimental data (26). The flux balance model was implemented in MATLAB and growth efficiencies were calculated from the ratio of growth rate (f_{growth}) and acetate uptake (f_{ac}) as $g_{eff} = f_{growth} / f_{ac}$.

Coupled Environment and Cell Model

Representations of *Geobacter* metabolism were coupled to simulations of a dynamic environment through incorporation into a reactive transport model. The two models were connected such that the reactive transport model was used to evaluate transport of substrate and biomass while the cell model provided the cell-specific reaction rates under the environmental conditions at a given time and location. These cell-specific rates were then used to compute the reaction rates in the macroscopic reactive-transport model. For dissolved constituents, the governing equation is

$$\phi \frac{\partial C}{\partial t} = \nabla \cdot (D^* \nabla C) - \nabla \cdot (\phi v C) + \phi \sum R, \qquad (7)$$

where ϕ is porosity, t is time, C is concentration, v is pore water velocity, D^* is the dispersion tensor implemented with dependence on v as described by Scheidegger (36), and ΣR is the net reaction rate. Flow velocities were computed from an imposed pressure gradient using a Darcy model (40).

In our implementation, the cell model was driven by the availability of acetate as the substrate, whose spatio-temporal dynamics proceeded via

$$\frac{\partial C_{ac}}{\partial t} = T_{ac} - R_{ac}^{cell} C_{BM} + R_{ferm}$$
$$\frac{\partial C_{BM}}{\partial t} = T_{BM} + g_{eff} R_{ac}^{cell} C_{BM} \quad , \qquad (8a, b)$$

where T_i denotes the transport of acetate (C_{ac}) and biomass (C_{BM}) due to convection and dispersion, g_{eff} is the growth efficiency, R_{ac}^{cell} is the rate of acetate uptake, and R_{ferm} is a source of acetate from the breakdown of high molecular weight organics. The model was solved numerically using sequential non-iterative operator splitting. In each timestep Δt, first the pressure and flow field were solved for, which was then used to calculate the net transport for each of the chemical species. Subsequently, concentration changes due to reactions were evaluated by solving a set of coupled ordinary differential equations at each node. Reaction parameters that depend on the cell model (i.e. g_{eff}, R_{ac}^{cell}) were computed for a given environmental condition and cell state, reflected by the intracellular concentrations, and were assumed constant over a timestep. Cell death was considered through negative growth efficiencies, which were obtained when the ATP produced did not account completely for cell maintenance demands and the existing pool of ATP was insufficient to meet the cellular energy requirements. In that case, use of biomass resources was considered to meet ATP demands ($a \cdot R_g$; see Eq. 3).

Results and Discussion

Model comparison and validation

Experimentally determined growth efficiencies under acetate limiting conditions are on the order of 4 g_{dw} mol^{-1} acetate at uptake fluxes >10 mmol acetate g_{dw}^{-1} hr^{-1}, and decrease to 0 at 0.91 mmol acetate g_{dw}^{-1} hr^{-1} (12). Under replete substrate conditions, growth efficiencies were similar

in the FB model and the kinetic description, yielding results consistent with data at high acetate uptake rates (Fig. 4.2). The fluxes are consistent with those of ^{13}C tracer experiments observed in the isotopic data of Tang et al. (43), which showed that the TCA cycle encompassed ~90% of the acetate uptake flux with an additional ~8% of acetate flowing through the TCA cycle being used for amino acid and lipid production, and the remainder of the acetate uptake flux passed through the pentose-phosphate pathway and gluconeogenesis. Along with the FB model, the kinetic model predicted that for lower acetate uptake rates, acetate is preferentially channeled into the TCA cycle, leading to a low growth efficiency. Both the kinetic and the FB model showed a nearly identical response of the TCA cycle to acetate uptake, with a nearly linear increase in the TCA cycle with increasing acetate uptake rates (not shown). Both models reproduced the general trend in growth efficiencies seen in the literature as a function of the acetate uptake rate (Fig. 4.2), reflecting that at elevated uptake rates, the portion of acetate following the growth reaction pathway increased relative to that for the TCA cycle.

In contrast to the flux balance approach, which does not contain information on intracellular concentrations or provide an explicit connection to extracellular substrate levels, the kinetic model mechanistically relates intracellular process rates to extracellular concentrations of acetate. Its results can therefore be parameterized as a function of acetate availability and provide an explicit link between intracellular processes and extracellular conditions. At low extracellular acetate concentrations (μM levels), acetate uptake responds strongly to changes in substrate availability (inset Fig. 4.2). Assuming Michaelis Menten kinetics, $R_{ac}^{cell} = v_{\max} \frac{[C_{ac}]}{K_m(acetate) + [C_{ac}]}$, and using steady state cell model results, one obtained v_{max} = (19.54±0.0.04) $mmol_{ac}$ gdw^{-1} hr^{-1} and $K_m(acetate)$ = (10.24±0.11) $x10^{-6}$ mol L^{-1}, consistent with half-saturation constants and maximum uptake rates derived from experimental data (12).

The kinetic model also provides estimates of intracellular metabolite concentrations, which can be used as diagnostics to experimentally assess its validity and limitations. Under steady state conditions, the cell model predicted malate concentrations in the mM range, consistent with predictions of high malate concentrations based on the thermodynamics of the malate dehydrogenase reaction (5). Several other substances, including oxaloacetate, citrate, isocitrate, and succinate were predicted—depending on growth conditions—to be present in the micro to millimolar range, and to increase by a factor of 10 to 30 between no growth and maximum growth conditions. Succinyl-CoA was predicted to be relatively constant, while significant variations under changing growth conditions were computed for pyruvate and α-ketoglutarate, with lower concentrations at higher growth rates.

Model sensitivity

The sensitivity analysis based on ≥ 1000 realizations for a given extracellular acetate concentration, which was sufficient to establish the probability distribution of the model response, allowed the identification of the reactions affecting growth efficiency most strongly (Fig. 4.3). The extent to which a parameter affected growth efficiency varies with the acetate uptake rate. For example, at low acetate uptake rates, growth efficiency was most sensitive towards parameters describing the ACT reaction. In general, however growth efficiency, over the range of acetate uptakes, was most sensitive to cell model parameters associated with the activation of acetate to acetyl-P catalyzed by AK (Fig. 4.3), a reaction essential to the use of acetate in biomass production as all acetate incorporated into cell biomass must go through this reaction (26). Increasing the forward rate constant k_f—corresponding to an increase in enzyme concentration (E_T), maximum enzyme activity (v_{max}), or higher substrate affinity (lower K_m)—

involved in the reaction catalyzed by CS decreased growth efficiencies as more acetyl-CoA is shifted to the TCA cycle. For the same reason, increasing the parameters associated with the reaction catalyzed by SDH resulted in a decrease of growth efficiency, and increasing parameters associated with PFO, a reaction involved in growth, resulted in an increase in growth efficiency. The variation in growth efficiency due to small—on the order of 5%—variations in forward and backward reaction rate constants can largely (> 95%) be explained by the linear model (Eq. 2). Uncertainties in E_T, v_{max} and K_m, however, tend to result in larger uncertainties in growth efficiencies due to error propagation, but the same reactions are found to have the most decisive impact (not shown).

Environmental Setting

Reactive transport models often do not—or only in a simplistic manner—reflect microbial population dynamics (22). To assess the importance of dynamically resolving cellular metabolism, where the rates depend on both extracellular and intracellular concentrations, reactive transport simulations with the full kinetic cell model (Model I) were contrasted with three parameterized versions. The first used a lookup table established from steady state runs of the kinetic cell model, so that cell-specific rates were expressed as a function of extracellular conditions, but did not take into account intracellular dynamics and assumed that intracellular metabolite concentrations have reached a steady state. Because computed intracellular metabolite concentrations (at least at the level resolved in the kinetic cell model) adjusted to changes in substrate availability over timescales of seconds, consistent with observed intracellular dynamics in bacteria (e.g. 35), the results from the steady state cell model were virtually indistinguishable from those of Model I and are hence not shown separately. The second implementation (Model

II) simplified the approach further, to a level typically used in reactive transport models, assuming that cell specific growth efficiency (g_{eff}, Eq. 8) is constant, and that acetate uptake (R_{ac}^{cell}, Eq. 8) can be expressed by Monod kinetics, with $K_{m(acetate)}$ = 10.24 μM and v_{max} = 19.54 mmol gdw^{-1} hr^{-1} as derived above. Finally, a third approximation employed both a constant growth efficiency and a constant acetate uptake rate as long as acetate was present (Model III), with a cell specific acetate uptake rate of 9 $x10^{-3}$ $mol_{acetate}$ g_{dw}^{-1} hr^{-1} and a growth efficiency of 3.3 g_{dw} m^{-3}, as given in (12).

In order to quantify the impact of microbial dynamics and substrate dependence of growth efficiencies under environmental conditions, simulations were performed in a domain 10 cm long and 6 cm high. The porous medium consisted of permeable sand (k = 10^{-11} m^2) into which a less permeable section was embedded (k = 10^{-13} m^2) as depicted in Figure 4.4. No flow conditions were set at the upper and lower domain boundaries and a positive pressure gradient was imposed across the horizontal x-direction. The inflowing fluid was set to contain 0.76 μM acetate and 0.03 g_{dw} m^{-3} biomass. After a period of constant input that allowed the establishment of a steady substrate and biomass distribution, the concentrations in the inflowing fluid were ramped up over a duration of 1 hr to an inflow concentration of 1 mM acetate and 0.3 g_{dw} m^{-3} biomass, reflecting a plume of dissolved organic carbon (16), and were held constant at high levels thereafter.

Steady state biomass and acetate distributions under pristine conditions showed distinct differences between the various models. For all representations, relatively low, uniform biomass distributions were observed (Fig. 4.4B,D,F). However, the fixed uptake and growth efficiency formulation (Model III) predicted spatially varying acetate concentrations, with lower levels in the low permeability zone (Fig. 4.4E). This drawdown was caused by the slightly elevated

biomass concentrations in that region (Fig. 4.4F) because this approximation contains no feedback between substrate level and the allocation of acetate to growth versus catabolism that would lower uptake rates at low substrate availability. Results from Model II closely matched Model I (Fig. 4.4A,C; 4B,D), despite that at low acetate concentrations, the Monod approximation and cell model differed in their growth efficiency. This is because at low acetate levels, cell specific acetate uptake rates are low. In addition, the Monod model does not take into account cell death, which when included became important for regulating biomass levels in the pristine setting at cell death rates on the order of 10% the growth rate (not shown).

Steady high substrate input stimulated microbial growth, reflected in the elevated biomass levels in both high and low permeability regions (Fig. 4.4H,J,L). A clear distinction was visible between the results obtained with the dynamic cell model and the Monod approximations when compared to the fixed growth efficiency description. The latter predicted biomass levels ranging from 0.3 to 1.2 g_{dw} m^{-3} in the low permeability zone (Fig. 4.4L), while the kinetic models suggested a region of higher biomass in the low permeability zone adjacent to the more permeable one (Fig. 4.4H,J). In the models that represented the cell in more detail, the maximum growth efficiencies exceeded the constant average value in the "fixed" model, leading to a build up of biomass and depletion of acetate in the low permeability zone. The Monod parameterized model suggested acetate levels that are similar to those for the cell model (Fig. 4.4G,I). The cell model predicted the depletion of biomass in those low permeable regions that exhibited low acetate concentrations (Fig. 4.4H). This pattern was less pronounced in the Monod model, which as a result of the missing feedback of substrate availability on growth efficiencies showed elevated biomass levels even where acetate levels approached zero (Fig. 4.4I,J).

Conclusion

The kinetic representation of *Geobacter sulfurreducens* central metabolism, encompassing its TCA cycle and the use of pyruvate in gluconeogenesis, successfully reproduces measured growth efficiencies with iron as electron acceptor over a wide range of extracellular acetate concentrations. Despite its limited scope, it predicts process rates that are in good agreement with results from a comprehensive flux balance model (26), as it includes feedback between metabolite levels and transformation rates which can accurately regulate the response over a range of substrate conditions.

The two main differences between these two modeling approaches are the extent of the network considered and that the kinetic description provides explicit estimates of intracellular metabolite concentrations. The more comprehensive description inherent in flux balance models—possible because they do not require extensive parameterization—is an advantage as intrinsically, it extends the range of applicability well beyond the acetate limited environmental settings discussed here. However, the computation of metabolite levels in the kinetic approach allows for a mechanistic process description linking intracellular to environmental conditions. In contrast, the flux balance approach requires *a priori* knowledge of uptake fluxes, which may restrict its use to settings where they are constrained by experimental data.

While comparison of the fully coupled reactive transport model with the Monod type simulations show that it is possible to approximate microbial distribution patterns without the explicit incorporation of cell models into reactive transport simulations, the parameterization has to reflect the response of intracellular processes. Process level descriptions of microbial metabolism give rise to emerging properties such as growth efficiencies that are critical in the incorporation of microbial dynamics in reactive transport models. Hence, models aiming at

describing *in situ* microbial functioning and at accounting for environmental feedbacks can benefit substantially from reflecting the growing knowledge on cellular metabolism, which in turn will bolster the predictive power necessary for their broad application.

Acknowledgments.

This work was supported by the Department of Energy Office of Science grant DE-FG02-05ER25676. We would like to thank two anonymous reviewers and the Editor A.M. Sporemann whose comments significantly improved the manuscript.

Appendix 4A

To derive estimates of rate and equilibrium constants required in the model, literature data was mined and converted into the format required for the cell model. Whenever available, enzyme turnover numbers were used as they represent a measurement of kQ_s (s^{-1}). However, this parameter was not often available so kQ_s values were derived from reported *Geobacter* enzymatic specific activities. Specific activity from pure enzyme extract was converted to a forward rate constant, kQ_s (s^{-1}) by:

$$kQ_s = SA_{pure} \cdot MW \qquad \text{(A1)}$$

where SA_{pure} (mol s^{-1} g_{enzyme}^{-1}) is the specific activity measured from the pure enzyme extract and MW is the molecular weight of an enzyme subunit (g mol^{-1}). Specific activity measured from the crude enzyme fraction was converted to an in situ v_{max} (mol L^{-1} s^{-1}) as described by Albe et al. (1).

$$v_{\max} = SA_{crude} \cdot f_{prot} \cdot \frac{g_{bm}}{V_{cell}} \qquad \text{(A2)}$$

where SA_{crude} (mol s^{-1} $g_{protein}^{-1}$) is measured from the crude enzyme fraction, f_{prot} is the fraction of cell biomass that is protein, determined to be 0.46 (26), g_{bm} is the grams dry weight of biomass per cell, determined to be 40 fg, and V_{cell} is the cell volume, determined to be 4.91 $x10^{-16}$ L calculated based on *G. sulfurreducens* cell size (37) assuming a cylindrical shape. This v_{max} value was converted to kQ_s for implementation into *Karyote* (31) according to:

$$kQ_s = \frac{v_{\max}}{E_T} \qquad \text{(A3)}$$

where E_T is the total enzyme concentration. The parameter, kQ_s, was converted into k and Q_s-values for implementation of the slow reaction dynamics into the cell model. Values of Q_s were calculated according to:

$$Q_s = \frac{Q_T}{\prod\prod Q_{fi}} \qquad \text{(A4)}$$

where Q_T is the equilibrium constant for the overall net reaction based on thermodynamic data, obtained from (15), and Q_{fi} is the equilibrium constant for the i^{th} fast reaction in each mechanism. Equilibrium constants for the fast reactions—and slow reactions when no thermodynamic data was available to estimate Q_T—were determined from:

$$Q_i = \prod_k \prod C_k^{\,v_{ik}} \qquad \text{(A5)}$$

where C_k represents the equilibrium concentration of species k in reaction i in the enzyme mechanisms below, and v_{ik} is its stoichiometric coefficient (positive for products, negative for reactants).

Concentrations of enzyme substrate complexes used in equation A5 are not measured directly and were calculated according to each enzyme's mechanism which is separated into several fast and one slow component (32):

Isomerization Reaction $E + S \overset{fast}{\longleftrightarrow} ES \overset{slow}{\longleftrightarrow} E + P$

Bi-Bi Ordered Reaction

$$E + S_1 \overset{fast}{\longleftrightarrow} ES_1$$
$$ES_1 + S_2 \overset{fast}{\longleftrightarrow} ES_2 \overset{slow}{\longleftrightarrow} E + P_1 + P_2$$

Ping Pong Reaction

$$E + S_1 \overset{fast}{\longleftrightarrow} ES_1 \overset{fast}{\longleftrightarrow} ES_2 + P_1$$
$$ES_2 + S_2 \overset{fast}{\longleftrightarrow} ES_3 \overset{slow}{\longleftrightarrow} P_2 + E$$

Tri-Ping Pong Reaction

$$E + S_1 \overset{fast}{\longleftrightarrow} ES_1 \overset{fast}{\longleftrightarrow} ES_2 + P_1$$
$$ES_2 + S_2 \overset{fast}{\longleftrightarrow} ES_3 \overset{fast}{\longleftrightarrow} P_2 + ES_4$$
$$ES_4 + S_3 \overset{fast}{\longleftrightarrow} ES_5 \overset{slow}{\longleftrightarrow} P_3 + E$$

The enzyme substrate concentrations in the slow reactions were calculated following Purich et al. (32):

isomerization reaction $$ES = \frac{E_T \cdot [S]}{Km_1 + [S]}, \qquad \text{(A6)}$$

ordered Bi-Bi reaction mechanism $$ES_2 = \frac{E_T \cdot [S_1] \cdot [S_2]}{Km_1 \cdot Km_2 + [S_1] \cdot Km_2 + [S_1] \cdot [S_2]}, \qquad \text{(A7)}$$

Ping-Pong reaction $$ES_3 = \frac{E_T \cdot [S_1] \cdot [S_2]}{Km_2 \cdot [S_1] + [S_2] \cdot Km_1 + [S_1] \cdot [S_2]}, \qquad \text{(A8)}$$

Tri Ping-Pong reaction

$$ES_5 = \frac{E_T \cdot [S_1] \cdot [S_2] \cdot [S_3]}{Km_1 \cdot [S_2] \cdot [S_3] + Km_2 \cdot [S_1] \cdot [S_3] + Km_3 \cdot [S_1] \cdot [S_2] + [S_1] \cdot [S_2] \cdot [S_3]}, \qquad \text{(A9)}$$

where $[S_1]$, $[S_2]$, and $[S_3]$ are the typical cell concentrations of the 1st, 2nd, and 3rd substrates to bind with the enzyme respectively, and Km_1, Km_2, and Km_3 are the half saturation constants for substrates one, two, and three respectively. The enzyme substrate complexes involved in the fast reactions were then calculated according to equations A10-A16. For enzymes that employ a Bi-Bi ordered mechanism:

$$[ES_1] = \frac{Km_2 \cdot [ES_2]}{[S_2]} \qquad \text{(A10)}$$

For a Ping-Pong Mechanism:

$$[ES_2] = \frac{Km_2 \cdot [ES_3]}{[S_2]} \tag{A11}$$

$$[ES_1] = \frac{([E_T] - [ES_2] - [ES_3]) \cdot [S_1]}{[S_1] + Km_1} \tag{A12}$$

For a Tri Ping-Pong Mechanism:

$$[ES_1] = \frac{[ES_3] \cdot Km_2 \cdot [P_1]}{[S_2] + Km_{p1}} \tag{A13}$$

$$[ES_2] = \frac{Km_2 \cdot [ES_3]}{[S_2]} \tag{A14}$$

$$[ES_3] = \frac{[E_T] - [ES_5] - [ES_4]}{1 + \frac{Km_2}{[S_2]} + \frac{Km_2 \cdot [P_1]}{[S_2] \cdot Km_{p1}} + \frac{Km_2 \cdot [P_1] \cdot Km_1}{[S_2] \cdot Km_{p1} \cdot [S_1]}} \tag{A15}$$

$$[ES_4] = \frac{Km_3 \cdot [ES_5]}{[S_3]} \tag{A16}$$

where *ES* are the enzyme substrate complexes, Km_i is the half saturation constant of the i^{th} substrate, Km_{pi} is the half saturation constant for the i^{th} product released, S_j is the j^{th} substrate in the enzymatic reaction, and P_j is the j^{th} product released. Values used for the parameterization of the reaction network are found in Table 4.1.

References

1. **Albe, K. R., M. H. Butler, and B. E. Wright.** 1990. Cellular concentrations of enzymes and their substrates. J. Theor. Biol. **143:**163-195.
2. **Bakker, B. M., P. A. M. Michels, F. R. Opperdoes, and H. V. Westerhoff.** 1997. Glycolysis in bloodstream form Trypanosoma brucei can be understood in terms of the kinetics of the glycolytic enzymes. J. Biol. Chem. **272:**3207-3215.
3. **Bear, J.** 1972. Dynamics of fluids in porous media. American Elsevier Publishing Company, Inc., New York.
4. **Behrends, T., and P. Van Cappellen.** 2005. Competition between enzymatic and abiotic reduction of uranium(VI) under iron reducing conditions. Chem. Geol. **220:**315-327.
5. **Bond, D. R., T. Mester, C. L. Nesbo, A. V. Izquierdo-Lopez, F. L. Collart, and D. R. Lovley.** 2005. Characterization of citrate synthase from Geobacter sulfurreducens and evidence for a family of citrate synthases similar to those of eukaryotes throughout the Geobacteraceae. Appl. Environ. Microbiol. **71:**3858-3865.
6. **Bradley, P. M., and F. H. Chapelle.** 1996. Anaerobic mineralization of vinyl chloride in Fe(II)-reducing aquifer sediments. Environ. Sci. Technol. **30:**2084-2086.
7. **Brun, A., P. Engesgaard, T. H. Christensen, and D. Rosbjerg.** 2002. Modeling of transport and biogeochemical processes in pollution plumes: Vejen landfill, Denmark. J. Hydrol. **256:**228-247.
8. **Caccavo, F. J., D. Lonergan, D. R. Lovley, M. Davis, J. F. Stolz, and M. J. McInerney.** 1994. Geobacter sulfurreducens sp. nov., a hydrogen- and acetate-oxidizing dissimilatory metal-reducing microorganism. Appl. Environ. Microbiol. **60:**3752-3759.

9. **Canfield, D. E., E. Kristensen, and B. Thamdrup.** 2005. Aquatic geomicrobiology. Elsevier Academic Press.

10. **Champine, J. E., and S. Goodwin.** 1991. Acetate catabolism in the dissimilatory iron-reducing isolate GS-15. J. Bacteriol. **173:**2704-2706.

11. **Chohnan, S., T. Nagata, and Y. Midorikawa.** 1994. Purification and characterization of a novel bifunctional enzyme, cyclic-ribonucleotide phosphomutase-5'-phosphodiesterase, from Aspergillus-niger. Biosci Biotech Bioch **58:**250-255.

12. **Esteve-Núñez, A., M. Rothermich, M. Sharma, and D. R. Lovley.** 2005. Growth of Geobacter sulfurreducens under nutrient-limiting conditions in continuous culture. Environ. Microbiol. **7:**641-648.

13. **Forster, J., I. Famili, P. Fu, B. O. Palsson, and J. Nielsen.** 2003. Genome-scale reconstruction of the Saccharomyces cerevisiae metabolic network. Genome Res. **13:**244-253.

14. **Gebhardt, N. A., R. K. Thauer, D. Linder, P. M. Kaulfers, and N. Pfennig.** 1985. Mechanism of acetate oxidation to CO_2 with elemental sulfur in Desulfuromonas-acetoxidans. Arch Microbiol **141:**392-398.

15. **Goldberg, R. N., Y. B. Tewari, and T. N. Bhat.** 2004. Thermodynamics of enzyme-catalyzed reactions - a database for quantitative biochemistry. Bioinformatics **20:**2874-2877.

16. **Gunten, U. V., and J. Zobrist.** 1993. Biogeochemical changes in groundwater-infiltration systems: Column studies. Geochim. Cosmochim. Ac. **57:**3895-3906.

17. **Herbel, M., and S. Fendorf.** 2006. Biogeochemical processes controlling the speciation and transport of arsenic within iron coated sands. Chem. Geol. **228:**16-32.

18. **Hunter, K. S., Y. Wang, and P. Van Cappellen.** 1998. Kinetic modeling of microbially-driven redox chemistry in subsurface environments: coupling transport, microbial metabolism and geochemistry. J. Hydrol. **209:**53-58.

19. **Jackowski, S., and C. O. Rock.** 1986. Consequences of reduced intracellular coenzyme-a content in Escherichia coli. J. Bacteriol. **166:**866-871.

20. **Jeong, H., B. Tombor, R. Albert, Z. N. Oltavai, and A.-L. Barbasi.** 2000. The large-scale organization of metabolic networks. Nature **407:**651-654.

21. **Leang, C., M. V. Coppi, and D. R. Lovley.** 2003. OmcB, a c-type polyheme cytochrome, involved in Fe(III) reduction in Geobacter sulfurreducens. J. Bacteriol. **185:**2096-2103.

22. **Lovley, D. R.** 2003. Cleaning up with genomics: applying molecular biology to bioremediation. Nat. Rev. Microbiol. **1:**35-44.

23. **Lovley, D. R.** 1993. Dissimilatory metal reduction Annu. Rev. Microbiol. **47:**263-290.

24. **Lovley, D. R., D. E. Holmes, and K. P. Nevin.** 2004. Dissimilatory Fe(III) and Mn(IV) reduction. Adv. Microb. Physiol. **49:**DOI 10.1016/S0065-2911(1004)49005-49005

25. **Lovley, D. R., E. J. P. Phillips, Y. A. Gorby, and E. R. Landa.** 1991. Microbial Reduction of Uranium. Nature **350:**413-416.

26. **Mahadevan, R., D. R. Bond, J. E. Butler, A. Esteve-Nunez, M. V. Coppi, B. O. Palsson, C. H. Schulling, and D. R. Lovley.** 2006. Characterization of metabolism in the Fe(III)-reducing organism Geobacter sulfurreducens by constraint-based modeling. Appl. Environ. Microbiol. **72:**1558-1568.

27. **Mauclaire, L., O. Pelz, M. Thullner, W. R. Abraham, and J. Zeyer.** 2003. Assimilation of toluene carbon along a bacteria-protist food chain determined by C-13-enrichment of biomarker fatty acids. J. Microbiol. Methods. **55:**635-649.

28. **McCleary, W. R., and J. B. Stock.** 1994. Acetyl phosphate and the activation of 2-component response regulators. J. Biol. Chem. **269:**31567-31572.

29. **Methé, B. A., K. E. Nelson, J. A. Eisen, I. T. Paulsen, W. Nelson, J. F. Heidelberg, D. Wu, M. Wu, N. Ward, M. J. Beanan, R. J. dodson, R. Madupu, L. M. Brinkac, S. C. Daugherty, T. R. DeBoy, A. S. Durkin, M. Gwinn, J. F. Dolonay, S. A. Sullivan, D. H. Haft, J. Selengut, T. M. Davidsen, N. Zafar, O. White, B. Tran, C. Romerio, H. A. Forberger, J. Weidman, H. Khouri, T. V. Feldblyum, T. R. Utterback, S. E. Van Aken, D. R. Lovley, and C. M. Fraser.** 2003. Genome of Geobacter sulfurreducens: Metal reduction in subsurface environments. Science **302:**1967-1969.

30. **Navid, A., and P. J. Ortoleva.** 2004. Simulated complex dynamics of glycolysis in the protozoan parasite Trypanosoma brucei. J. Theor. Biol. **228:**449-458.

31. **Ortoleva, P., E. Berry, Y. Brun, J. Fan, M. Fontus, K. Hubbard, K. Jaqaman, L. Jarymowycz, A. Navid, A. Sayyed-Ahmad, Z. Shreif, F. Stanley, K. Tuncay, E. Weitzke, and L.-C. Wu.** 2003. The Karyote physico-chemical genomic, proteomic metabolomic cell modeling system. OMICS **7:**269-283.

32. **Purich, D. L., and R. D. Allison.** 1999. Handbook of biochemical kinetics. Academic Press.

33. **Reed, J. L., T. D. Vo, C. H. Schilling, and B. O. Palsson.** 2003. An expanded genome-scale model of Escherichia coli K-12 (iJR904 GSM/GPR). Genome Bio. **4:**R54.

34. **Rockhold, M. L., R. R. Yarwood, and J. S. Selker.** 2004. Coupled microbial and transport processes in soils. Vadose Zone J. **3:**368-383.

35. **Schaefer, U., W. Boos, R. Takors, and D. Weuster-Botz.** 1999. Automated sampling device for monitoring intracellular metabolite dynamics. Anal. Biochem. **270:**88-96.

36. **Scheidegger, A. E.** 1961. General theory of dispersion in porous media. J. Geophys. Res. **66:**3273-3278.

37. **Seeliger, S., R. Cord-Ruwisch, and B. Schink.** 1998. A periplasmic and extracellular c-type cytochrome of Geobacter sulfurreducens acts as a ferric iron reductase and as an electron carrier to other acceptors or to partner bacteria. J. Bacteriol. **180:**3686-3691.

38. **Seki, K., M. Thullner, and P. Baveye.** 2004. Nutrient uptake kinetics of filamentous microorganisms: Comparison of cubic, exponential, and Monod models. Ann. Microbiol. **54:**181-188.

39. **Snoeyenbos-West, O. L., K. P. Nevin, R. T. Anderson, and D. R. Lovley.** 2000. Enrichment of Geobacter species in response to stimulation of Fe(III) reduction in sandy aquifer sediments. Microb. Ecol. **39:**153-167.

40. **Spiteri, C., C. Slomp, K. Tuncay, and C. Meile.** 2008. Modeling biogeochemical processes in subterranean estuaries: The effect of flow dynamics and redox conditions on submarine groundwater discharge of nutrients. Water Resour. Res. **44:**doi:10.1029/2007WR006071.

41. **Stelling, J.** 2004. Mathematical models in microbial systems biology. Curr. Opin. Microbiol. **7:**513-518.

42. **Stelling, J., S. Klamt, K. Bettenbrock, S. Schuster, and E. D. Gilles.** 2002. Metabolic network structure determines key aspects of functionality and regulation. Nature **420:**190-193.

43. **Tang, Y. J., R. Chakraborty, H. Garcia Martin, J. Chu, T. C. Hazen, and J. D. Keasling.** 2007. Flux analysis of central metabolic pathways in Geobacter metallireducens during reduction of soluble Fe(III)-nitrilotriacetic acid. Appl. Environ. Microbiol. **73:**3859-3864.

44. **Thullner, M., P. Regnier, and P. Van Cappellen.** 2007. Modeling microbially induced carbon degradation in redox-stratified subsurface environments: concepts and open questions. Geomicrobiol. J. **24:**139-155.

45. **Tong, A. H. Y., G. Lesage, G. D. Bader, H. M. Ding, H. Xu, X. F. Xin, J. Young, G. F. Berriz, R. L. Brost, M. Chang, Y. Q. Chen, X. Cheng, G. Chua, H. Friesen, D. S. Goldberg, J. Haynes, C. Humphries, G. He, S. Hussein, L. Z. Ke, N. Krogan, Z. J. Li, J. N. Levinson, H. Lu, P. Menard, C. Munyana, A. B. Parsons, O. Ryan, R. Tonikian, T. Roberts, A. M. Sdicu, J. Shapiro, B. Sheikh, B. Suter, S. L. Wong, L. V. Zhang, H. W. Zhu, C. G. Burd, S. Munro, C. Sander, J. Rine, J. Greenblatt, M. Peter, A. Bretscher, G. Bell, F. P. Roth, G. W. Brown, B. Andrews, H. Bussey, and C. Boone.** 2004. Global mapping of the yeast genetic interaction network. Science **303:**808-813.

46. **Vandevivere, P., and P. Baveye.** 1992. Saturated hydraulic conductivity reduction caused by aerobic-bacteria in sand columns. Soil Sci. Soc. Am. J. **56:**1-13.

47. **Walsh, K., and D. E. Koshland.** 1984. Determination of flux through the branch point of 2 metabolic cycles - the tricarboxylic-acid cycle and the glyoxylate shunt. J. Biol. Chem. **259:**9646-9654.

48. **Watson, I. A., S. E. Oswald, K. U. Mayer, W. Youxian, and S. A. Banwart.** 2003. Modeling kinetic processes controlling hydrogen and acetate concentrations in an aquifer-derived microcosm. Environ. Sci. Technol. **37:**3910-3919.

49. **Weiss, J. V., and I. M. Cozzarelli.** 2008. Biodegradation in contaminated aquifers: Incorporating microbial/molecular methods. Ground Water **46:**305-322.

50. **Weitzke, E. L., and P. J. Ortoleva.** 2003. Simulating cellular dynamics through a coupled transcription, translation, metabolic model. Comput. Biol. Chem. **27:**469-481.

51. **Wilkins, M. J., F. R. Livens, D. J. Vaughan, and J. R. Lloyd.** 2006. The impact of Fe(III)-reducing bacteria on uranium mobility. Biogeochemistry **78:**125-150.

Table 4.1: Values used for parameterization of the reaction network.

Enzyme[α–δ]	Enzyme total (M)	Enzyme activity[a-c]	Km values (M)[d,**]	Q_T [e,**]	k, Q^x
ACO [α]	$1x10^{-6}$ (41)	240 [a,(18)]	$Km_{citrate} = 1x10^{-2}$ (9)	$6.80x10^{-2}$	15f: Q=1.00e2 M^{-1} 6s: Q=6.80e-2 M k=2.20e5 M^{-1} s^{-1}
ACT [γ]	$1x10^{-6}$ (41)	900 [a,(18)]	$Km_{succ-coa} = 1.5x10^{-4}$ (19) $Km_{acetate} = 5x10^{-4}$ (19)	N/A**	21f: Q=6.67e3 M^{-1} 22f: Q=1.96e-3 M^{1} 23f: Q=2.00e3 M^{-1} 9s: Q=1.73e-1 M k=3.25e5 M^{-1} s^{-1}
AK [β]	$2.26x10^{-5}$ (1)	22.8 [a,(13)]	$Km_{ATP} = 7x10^{-5}$ (17) $Km_{Ace} = 3x10^{-1}$ (21)	$8.70x10^{-3}$	1f: Q=7.69 M^{-1} 1s: Q=7.92e-8 M^{2} k=7.69e8 M^{-2} s^{-1} 2f: Q=1.43e4 M^{-1}
CS [β]	$1.73x10^{-4}$ (7)	8.3 [c,(7)]	$Km_{oxaloacetate} = 4.3x10^{-6}$ (7) $Km_{acetyl-CoA} = 1.41x10^{-5}$ (7)	N/A**	13f: Q=2.33e5 M^{-1} 14f: Q=7.09e4 M^{-1} 5s: Q=2.11e-4 M^{2} k=3.94e6 M^{-2} s^{-1}
FUM [α]	$1x10^{-6}$ (41)	320.9 [a,(13)]	$Km_{fumarate} = 2.3x10^{-5}$ (18)	4.43	26f: Q=4.35e4 M^{-1} 11s: Q=1.02e-2 M k=1.97e6 M^{-1} s^{-1}
IDH [β]	$4.74x10^{-5}$ (1)	40.8 [a,(13)]	$Km_{isocitrate} = 8x10^{-4}$ (19) $Km_{nadp} = 1.7x10^{-5}$ (25)	$9.3x10^{-1}$	16f: Q=1.25e3 M^{-1} 17f: Q=5.88e4 M^{-1} 7s: Q=1.26e-6 M^{3} k=4.25e7 M^{-3} s^{-1}
MDH [β]	$1x10^{-6}$ (41)	471.5 [a,(13)]	$Km_{malate} = 5x10^{-3}$ **,(7)	$1.2x10^{-5}$	27f: Q=1.11e3 M^{-1} 28f: Q=2.00e2 M^{-1}

			$Km_{nad} = 9x10^{-4}$ **,(35)		13s: Q=5.40e-9 M^2 k=5.45e12 M^{-2} s^{-1}
AKS γ	$1x10^{-6}$ (41)	52.2 a,(13)	$Km_{akg} = 2x10^{-3}$ (19) $Km_{CoA} = 4x10^{-5}$ (19)	N/A**	18f: Q=5.00e2 M^{-1} 19f: Q=6.35e-4 M 20f: Q=2.50e4 M^{-1} 8s: Q=8.78e-3 M^{-1} k=3.71e5 M^1 s^{-1}
PFO γ	$1x10^{-6}$ (41)	120 a,(19)	$Km_{acetyl\text{-}CoA} = 7x10^{-5}$ (19)	N/A**	5f: Q=1.43e4 M^{-1} 6f: Q=5.61e-4 M 7f: Q=8.33e2 M^{-1} 3s: Q=1.30e-3 M k=5.77e6 M^{-1} s^{-1}
PPD δ	$1x10^{-6}$ (41)	5900 b,(51)	$Km_{ATP} = 2x10^{-4}$ (51) $Km_{AMP} = 6x10^{-6}$ (51) $Km_{Pi} = 8.3x10^{-4}$ (51) $Km_{pyruvate} = 2.7x10^{-5}$ (51)	$1.45x10^{-3}$	8f: Q=3.70e4 M^{-1} 12s: Q=1.43e-4 M k=3.78e6 M^{-1} s^{-1} 9f: Q=5.00e3 M^{-1} 10f: Q=6.00e-6 M 11f: Q=1.20e3 M^{-1} 12f: Q=7.56e-4 M
PTA β	$1x10^{-6}$ (41)	48.0 a,(13)	$Km_{acetyl\text{-}P} = 3x10^{-4}$ **,(38) $Km_{CoA} = 9.36x10^{-5}$ **,(14)	$1.47x10^2$	3f: Q=3.33e3 M^{-1} 4f: Q=1.07e4 M^{-1} 4s: Q=4.13e-4 M^2 k=7.26e6 M^{-2} s^{-1}
SDH α	$8.93x10^{-5}$ (1)	10.2 a,(13)	$Km_{succinate} = 5x10^{-4}$ (19)	N/A**	24f: Q=2.00e3 M^{-1} 10s: Q=8.98e-4 M^2 k=7.94e3 M^{-2} s^{-1}

α–γ Enzyme mechanisms: (α) isomerization, (β) bi-bi, (γ) ping-pong, (δ) tri ping-pong

[a-c] ([a,b]) denote enzyme specific activities from crude ([a]) and pure ([b]) enzyme fraction, SA (nmol min^{-1} $mg_{protein}^{-1}$), ([c]) denotes enzyme turnover numbers, k_{cat} (s^{-1}).

[d] akg: α-ketoglutarate; succ-coa: Succinyl-CoA. See Fig. 4.1 for EC numbers of enzymes.

[e] Q_T denotes the equilibrium constant for the overall net reaction based on thermodynamic data, obtained from (15). N/A indicates that the equilibrium constant for the slow reaction is derived from typical species concentrations

[x] denotes the *Q* and *k* values implemented in the kinetic model. Fast reactions are denoted by "*f*", slow reaction by "*s*". Numbers refer to the reactions labeled in Figure 4.1.

[**] Estimates are based on the following typical substrate concentrations (units: M): Oxaloacetate: $1x10^{-7}$ (5); Malate: $5x10^{-3}$ (5); Acetyl-CoA: $3.5x10^{-4}$ (1); PEP: $9.1x10^{-5}$ (1); Fumarate $3x10^{-5}$ (1), Citrate: $1.3x10^{-2}$ (1); α-ketoglutarate: $4.76x10^{-4}$ (1); ATP: $2.64x10^{-3}$ (1); ADP $8.23x10^{-4}$ (1); AMP: $1.51x10^{-4}$ (1); Pyruvate: $3.9x10^{-4}$ (1); CoA: $9.36x10^{-5}$ (11); Succinate: $1.67x10^{-3}$ (47); Isocitrate: $2.9x10^{-5}$ (47); Acetyl-P: $3x10^{-4}$ (28); Succinyl-CoA: $2.59x10^{-5}$ (19); Acetate: $5x10^{-4}$ (14). These values were also used to estimate Q_f (Eq. A5).

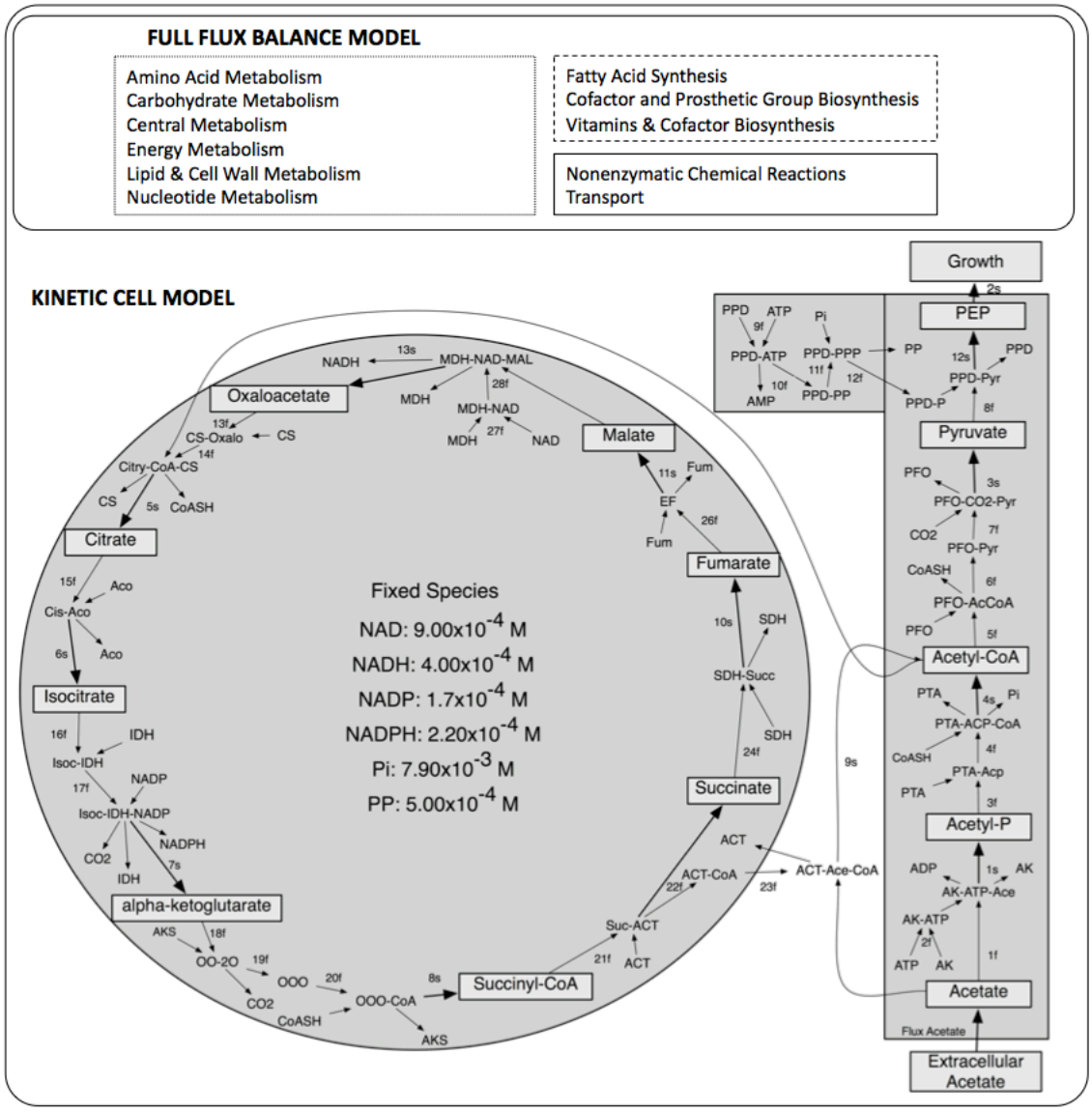

Figure 4.1: Structure of the kinetic cell model and flux balance models. The kinetic model focuses on the fate of acetate in the metabolism of *Geobacter sulfurreducens* through incorporation into biomass from gluconeogenesis or energy production from the TCA cycle. All reactions are assumed to be intrinsically reversible, and the rates are computed using the parameter values listed (for data sources see the Appendix). The flux balance model is described in Mahadevan et al. (26) and encompasses some 500 reactions and species.

Abbreviations (Enzyme Commission numbers, EC): ACO: aconitase (4.2.1.3), ACT: acetate-CoA transferase (2.8.3.8), AK: acetate kinase (2.7.2.1), CS: citrate synthase (2.3.3.1), FUM: Fumarase (4.2.1.2), IDH: isocitrate dehydrogenase (1.1.1.42), MDH: malate dehydrogenase (1.1.1.37), AKS: α-ketoglutarate synthase (1.2.7.3), PFO: pyruvate ferredoxin oxidoreductase (1.2.7.1), PPD: pyruvate phosphate dikinase (2.7.9.1), PTA: phosphate acetyl transferase (2.3.1.8), and SDH: succinate dehydrogenase (1.3.99.1)

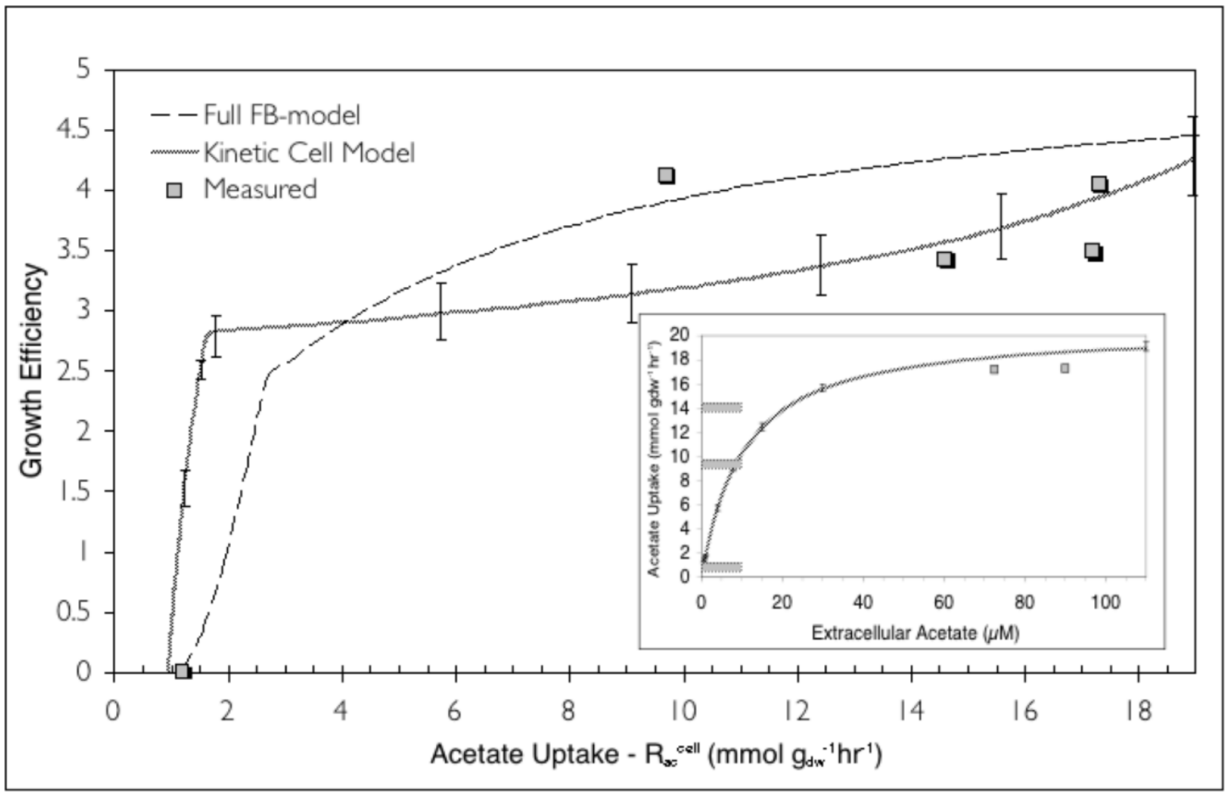

Figure 4.2: Growth efficiency in g_{dw} $mol_{acetate}^{-1}$ at a given acetate uptake rate (R_{ac}^{cell}) for the cell model, flux balance model, and measured chemostat data (12). Error bars for the kinetic cell model represent the 25% and 75% quartile ranges as determined in the sensitivity analysis (see text). Inset: Acetate uptake flux at a given extracellular acetate concentration computed with the kinetic model along with measured data (chemostat data depicted with dashed lines indicates measured acetate concentrations below the detection limit of 10 μM).

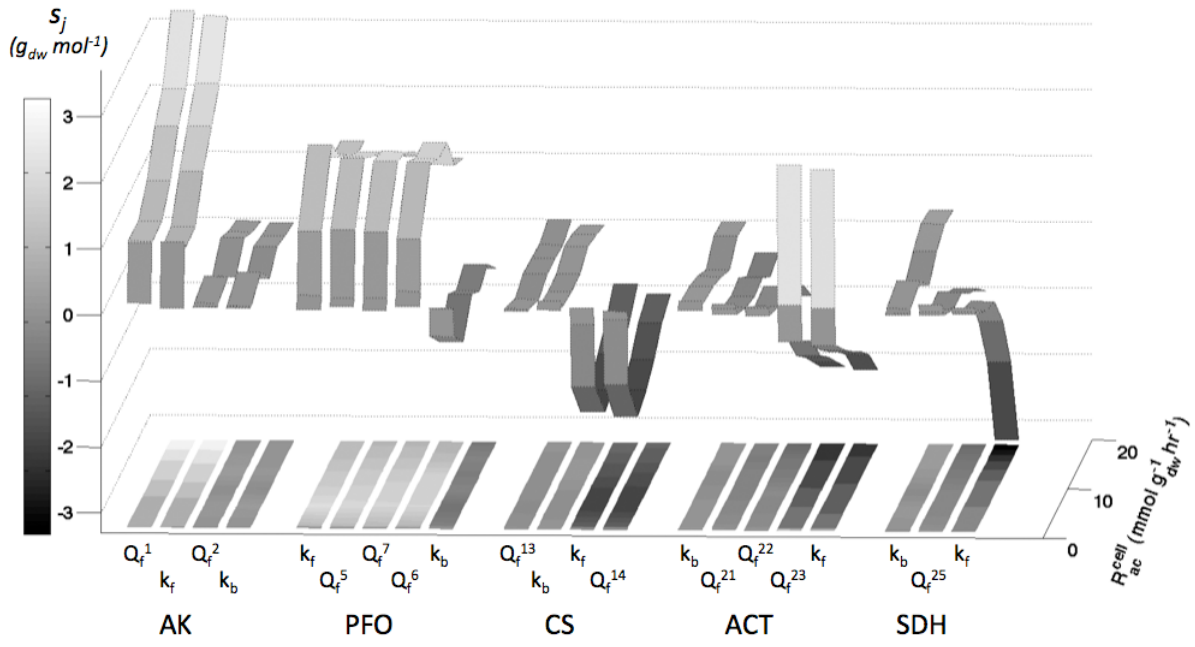

Figure 4.3: Sensitivity, s_j, of growth efficiencies to perturbations in the cell model parameters as a function of acetate uptake rates (Eq. 2). Bold labels along the bottom (AK, CS, ACT, SDH and PFO) denote the reactions promoted by the respective enzymes (see Fig. 4.1). k_b, k_f, and Q values denote the model parameters. Large absolute values of s_j indicate a strong impact of a model parameter on resulting growth efficiencies (see text for details).

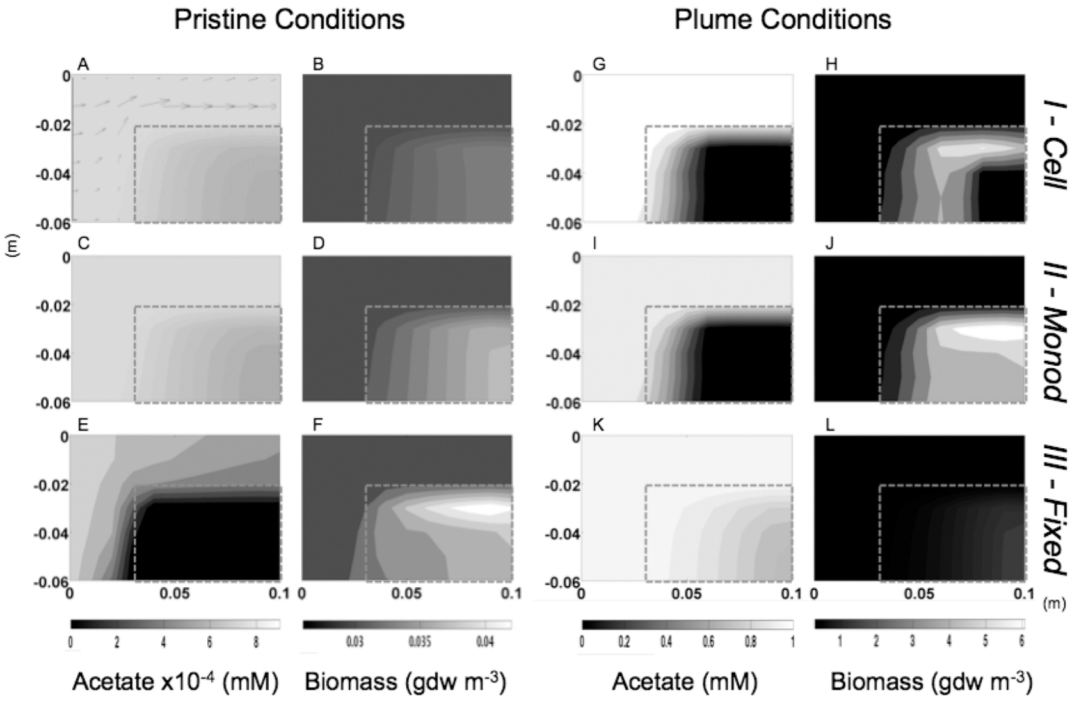

Figure 4.4: Results of reactive simulations utilizing different representation of bacterial growth and acetate uptake. Steady state acetate and biomass distributions under low (A-F; left column) and high (G-L; right column) input conditions, for the dynamic cell model (A,B,G,H), the Monod parameterization (C,D,I,J), and simulations with fixed growth efficiency and acetate uptake rate (E,F,K,L). The low permeability zone is indicated by the dashed boxes and the arrows in panel A indicate the direction and magnitude of flow.

CHAPTER 5

PREDICTING MICROBIAL METABOLISM UNDER VARYING ENVIRONMENTAL CONDITIONS: SIGNIFICANCE OF NEAR OPTIMAL PHENOTYPES[6]

[6] Eric Lee King, Yimeng Shi, and Christof Meile. To be submitted to *BMC Systems Biology*

Abstract:

Background: To elucidate the reactions that govern microbial activities, mathematical models are developed that utilize the intracellular reaction network of an organism. Commonly, as in flux balance analysis (FBA), predicting metabolic networks assumes an organism utilizes the most efficient set of reactions for e.g. growth or ATP production. Here, elementary flux mode analysis (EFMA) was used to determine the reactions occurring in *Geobacter sulfurreducens*. Unlike flux balance models, this technique elucidates all of the possible metabolic networks, or phenotypes, of an organism, allowing for an investigation of near optimal networks, which are phenotypes that do not have the best e.g. growth efficiencies, but can become relevant in variable environmental conditions.

Results: Predicted metabolic networks from elementary flux mode analysis are compared to those from the more commonly used flux balance analysis. While the reactions utilized between EFMA and flux balance analysis are relatively similar, significant differences are seen when comparing reaction rates. In addition, the underlying differences between the phenotypes from EFMA are elucidated. Finally, phenotypes that are a combination of both most optimal for growth as well as minimizing changes in their metabolic machinery between variable environmental conditions are determined and analyzed.

Conclusions: Results show the potential importance of investigating multiple phenotypes for an organism, rather than one that optimizes a goal function. In particular, sub-optimal phenotypes can be elucidated, which can become important in an environment where conditions can vary rapidly. Use of a metabolic network that minimizes the transition cost in the biochemical machinery needed to utilize the substrates found in the different conditions might prevail over a

network that is most optimal under just one environmental condition. Results here provide the means for laboratory tests to validate the potential of these sub-optimal phenotypes.

Background:

Microbially meditated reactions drive all major biogeochemical cycles on Earth [1], and are key to a myriad of societal issues ranging from antibiotic resistance [2] to alternative energy production [3] and bioremediation [4]. Thus, understanding the metabolic functioning of microbes, as well as their adaptations to physico-chemical changes in their surroundings is a central research theme in a wide range of fields. Such adaptations can lead to a shift in microbial populations as well as a reorganization of intracellular processes [5, 6].

When environmental conditions vary, an organism adjusts its enzymatic machinery. If environmental variability is an intrinsic system characteristic, then an optimal metabolic strategy may account for the necessary intracellular reallocation of resources. For example, Mitchell et al. [7] have shown pre-induced genes in *E. coli* such that the cell is best adapted for variable conditions, rather than a constant environmental setting. In addition, Schuetz et al. [8] show *E. coli* utilizing a metabolic network that does not maximize growth alone, but also accounts for adjustment in their enzymatic machinery given changing environmental condition (e.g. alternating between glucose and acetate as carbon sources).

Analysis of experimentally validated in silico cell models can be utilized to predict phenotypic plasticity. These models are generally based on the assumption that cellular metabolites are at a pseudo-steady state since adjustments to the enzymatic machinery occurs on much shorter time scales than both growth and changes in environmental conditions [9]. These models describe potential cellular metabolism via a stoichiometric matrix that captures the

microbial intracellular reaction network. Most commonly, one realized phenotype is determined through flux balance (FB) analysis [9], which optimizes a goal function that may differ under different environmental conditions [10]. Results from these models have been shown to be consistent with experimental data and have been used for predictive purposes.

Instead of identifying a single optimal network, elementary flux mode analysis (EFMA) returns all feasible steady state realizations of the intracellular reaction network. It has been used for many applications; including determining biomass and energy production pathways in E. coli given oxygen limitations [11, 12] and energy flow through microbial communities in hot springs [13]. Adaptations related to allocation of resources under variable environmental conditions were investigated in Carlson [14] who utilized EFMA to look at the investment costs for producing the enzymes related to reaction pathways and determined that E. coli favored less efficient pathways during times when nutrients were scarce, but required less of an investment cost to produce.

In this study, we investigate Geobacter sulfurreducens, a well-studied organism [e.g. 15] that has importance in bioremediation efforts [16] utilizing EFMA. We assess all feasible steady state realizations of a comprehensive *Geobacter* metabolic network with the following goals: (i) investigate the importance of near optimal reaction pathways in the context of different substrate and terminal electron acceptor availabilities; (ii) determine the differences in pathways utilized in near optimal solutions; and (iii) compare results obtained from EFMA to those from a FB model.

Methodology:

Curation of the metabolic network

The *G. sulfurreducens* reaction network (Tables A.1 and A.2) was based on Mahadevan et al. [17], with modifications making it computationally tractable for EFMA. Completely described in

Table A.1, in short, the reactions removed involve heavy metal toxicity mediation and metabolites that were taken up and then not further utilized or subsequently exported. In addition, extracellular exchange of amino acids and nucleotides was modified to prevent use as additional carbon sources by allowing export but not import into the cell. When metabolites had multiple reactions that described uptake into the cell, those that were metabolically more expensive (e.g. utilize ATPases) were removed in favor of reactions that were less so (e.g. involving hydrogen symporter or passive diffusion). Since water and CO_2 are allowed to freely enter and leave the cell through diffusion, they were considered unbalanced metabolites with their uptake reactions removed.

Singular Value Decomposition

To assess topological properties of the metabolic network, singular value decomposition (SVD) was performed on the stoichiometric matrix, *S*, of the curated model using MATLAB. Three matrices were determined $S = U\Sigma V^T$; where *U* contains information about eigen-reactions, the diagonal matrix, Σ, contains singular values, and the matrix V^T contains information about eigen-connectivities [18]. Each eigen-reaction traces back to specific metabolites and each eigen-connectivity was used to investigate the most significant reactions occurring in the model.

Determination of cellular fluxes

The fluxes through the metabolic network of *G. sulfurreducens* were calculated through elementary flux mode analysis (see e.g. [19, 20]). In brief, this type of analysis utilizes the stoichiometric matrix of a cellular reaction network, information on the reversibility of reactions, and an assumption that metabolites within the cell are at steady state to determine all of the

possible elementary modes that exist for a reaction network (here referred to as cellular "phenotypes"). The program CellNetAnalyzer 2012.1 [21] was used to determine the phenotypes of *G. sulfurreducens* with the included algorithm EFMtool [22], with settings adjusted to deal with the large memory requirements (java heap space set to 32GB and using the adjacency and memory settings "rankup-nodpi-outcore" and "sort-out-core" respectively).

Cellular metabolic rates were also calculated using FBA to estimate intracellular fluxes and metabolite exchange with the environment for an imposed acetate uptake rate, given lower and upper bounds and maximization of biomass production.

Analysis of phenotypes

To assess the efficiency of the use of terminal electron acceptors and carbon substrates, the amount of iron, fumarate and acetate utilized per gram dry weight (gdw) of biomass produced was calculated for each phenotype. Fluxes were converted to rates through knowledge that the growth reaction corresponds to grams of new biomass produced gdw^{-1} hr^{-1}. Therefore the ratio of e.g. acetate uptake to growth provides the mmol of acetate gdw^{-1} hr^{-1} needed to sustain growth.

Differences in connectivity patterns between the phenotypes derived from EFMA and the one phenotype from FB analysis [17] were calculated by determining the number of reactions that are distinct in the phenotypes being compared. This was calculated as the sum of the reactions that were utilized in either the FB or the EFMA phenotype but not the other. Fluxes less than 10^{-12} moles gdw^{-1} were considered as a zero rate for that reaction to account for any mathematically insignificant but non-zero fluxes. Connectivity differences were also assessed through the sum of the differences in the reaction rates such that:

$$s_j = \sum_{i=1}^{k} \left(f_a^i - f_b^i\right)^2, \qquad (1)$$

where *f* is the flux through all reactions, *k*, where *a* and *b* refer to the phenotypes from EFMA or FB analysis.

To compare the metabolites and reactions utilized between the different phenotypes, reporter metabolites were determined based upon Patil and Nielson [23], who analyzed the transcriptional response of metabolites' neighboring enzymes under different conditions. Here, fluxes for reactions in the different phenotypes were used in place of changes in transcription levels. Reporter metabolites were therefore computed as the square of the relative change in the fluxes acting upon each metabolite:

$$Z_m = \frac{1}{\sqrt{k,m}} \sum_{i=1}^{k,m} \left(\frac{f_a^i - f_b^i}{1/2 (f_a^i + f_b^i)} \right)^2, \qquad (2)$$

where *k* is the number of reactions connected to metabolite *m*, each with flux *f*, and *a* and *b* refer to the two phenotypes being compared.

The optimality, *N*, of a transition between two phenotypes (or states) follow ideas presented in Schuetz et al. [8]. *N* depends on both a transition cost (i.e. a measure of the adjustments of the metabolic machinery needed) and how efficient the phenotypes are. The efficiency of a phenotype was quantified based upon the amount of iron, fumarate, and acetate needed to produce 1 gdw of biomass for each phenotype. To weight these multiple dimensions, acetate and iron consumption were normalized to those fluxes found in the FB model of Mahadevan et al. [17]. Since fumarate fluxes were not included in the FB model, the maximum fumarate uptake and corresponding growth rates, derived from chemostat experiments, were used to normalize the results; 11.8 gdw $(mol_{fumarate})^{-1}$ [24]. The transition cost was quantified as the sum of the differences in the reaction rates between two EFMA phenotypes divided by the total number of reactions, *k*. *N* is therefore given by:

$$N = \frac{1}{k}\sum_{i=1}^{k}\left(\frac{f_a^i - f_b^i}{1/2(f_a^i + f_b^i)}\right)^2 \cdot \sqrt{Y_{fum,a}^2 + Y_{ac,a}^2 + Y_{fe,a}^2 + Y_{fum,b}^2 + Y_{ac,b}^2 + Y_{fe,b}^2} \qquad (3)$$

where k is the number of reactions and Y is the is the amount of acetate, *ac*, iron, *fe*, and fumarate, *fum*, needed to produced 1 gdw of biomass. To find phenotypes in different clusters that were most optimal, N for each phenotype in one cluster was computed between every phenotype in another cluster.

Results and Discussion:

Network curation

The curated reaction network of *G. sulfurreducens* removes or modifies 34 reactions from the original, full network (Table A.1) to provide a network computationally feasible for EFMA. To confirm that removal of these reactions had minimal effect, a flux balance model was created utilizing the curated network and compared to the fluxes of Mahadevan et al. [17] with indistinguishable results.

Topological properties

To assess the structure of the curated network, analysis of its stoichiometric matrix was performed using singular value decomposition (SVD), which provides information about the relationships of metabolites and reactions in the model [18]. The larger the singular value, the more important the corresponding eigen-reaction or eigen-connectivity, which corresponded to significant or core reactions in the stoichiometric matrix of *Geobacter*.

In general, results show the importance of energy production and consumption. The first eigen-reaction is related with proton and proton-motive force with NADPH and NADP as key metabolites. The next eigen-reaction highlights energy metabolism through ATP synthesis. A

similar pattern is seen over the next three eigen-reactions as ATP, ADP, NADP, and NADPH dominate. In addition, coenzyme A, related to the TCA cycle and acetate transformations, is also shown to be of importance. Eigen-connectivites are dominated by reactions that involve those metabolites determined from the eigen-reactions.

Elementary modes

EFMA provides 4,966,879 elementary modes ("phenotypes") determined for the curated network. Each phenotype utilizes iron, fumarate, or a combination of the two as terminal electron acceptors (Fig. 5.1). Phenotypes arrange themselves into clusters with those within a cluster (e.g. cluster 1) having relatively similar acetate and terminal electron acceptor (TEA) requirements for growth. In contrast, phenotypes between clusters (e.g. a phenotype in cluster 1 vs. cluster 2) have a more significant difference in carbon and TEA requirements.

The FB phenotype derived from Mahadevan et al. [17] falls within those phenotypes from EFMA that utilize iron as TEA. The closer a phenotype is to the origin, the more efficient it is at producing biomass using acetate and iron, and it is therefore evident that the flux balance phenotype is not most optimal at producing biomass. This is a result of the additional constraints that were imposed on the acetate uptake rate for the flux balance model, which limited the uptake of acetate into the cell. Correspondingly, the growth efficiency for the phenotype that is most optimal at producing biomass (i.e. closest to the origin in cluster 1; 4.71 gdw / $mol_{acetate}$) using iron as the TEA is approximately 7% greater than what is seen for the flux balance model for *G. sulfurreducens* (4.4 gdw / $mol_{acetate}$). Consistent with chemostat experiments, those phenotypes utilizing iron as a TEA are generally less efficient at growth on acetate than phenotypes that utilize fumarate [24]. The most efficient phenotype for growth utilizing fumarate as a TEA has a

similar growth efficiency (12.5 gdw / $mol_{acetate}$) compared to the growth efficiencies determined for *G. sulfurreducens* at the highest growth rates investigated in chemostats (11.8 gdw / $mol_{acetate}$).

Elementary mode vs. flux balance phenotype

A comparison of the connectivity patterns between the FB and each of the EFMA phenotypes was determined through calculation of the number of distinct reactions occurring in the two phenotypes being compared. Results indicate that each EFMA phenotype differs in 0 to 51 out of a total of 494 reactions from the FB phenotype. While this assessment of active vs. inactive reactions would indicate that connectivity patterns are relatively similar between the phenotypes, taking into account the differences in reaction rates between the FB and EFMA phenotypes shows more substantial differences (inset, Fig. 5.2). With phenotypes utilizing different amounts of acetate and TEA to produce BM, this result suggests the need to investigate the rates and abundances of enzymes catalyzing a reaction, rather than just determining if a reaction is occurring to elucidate the differences in the metabolic machinery utilized.

Comparison of the phenotypes

EFMA phenotypes organize into 12 distinct clusters based upon the amount of acetate and iron needed for growth (Fig. 5.1). For example, clusters 1 and 2 both use iron as a TEA but are distinct in their growth yields with the two extremes within cluster 1 differing in the amount of acetate needed to produce 1 gdw of biomass by approximately a factor of two. The similarity of the reaction networks for the different phenotypes (Fig. 5.2) was quantified by looking at the rates of the reactions utilized (Eq. 1). As it is computationally prohibitive to quantify the

differences between all phenotypes, every 100th phenotype in each cluster was compared. Similar to what was seen when comparing EFMA phenotypes to the FB network, the closer a phenotype is to each other in linear distance to phenotypes that use the same TEA, generally speaking, the more similar the reaction rates between them (Fig. 5.2).

To further elucidate the differences between the phenotypes, reporter metabolites, which denote significant changes in flow through specific substrates, were determined for the most efficient phenotypes in each of the 12 clusters (66 comparisons, Table A.3). When comparing a phenotype that utilizes iron to one that utilizes fumarate as a TEA, succinate and/or fumarate are among the top five reporter metabolites (see e.g. cluster 1 vs. cluster 3 and cluster 1 vs cluster 11 in Table A.3). Significant changes are seen in the reaction rates associated with these metabolites consistent with experimental observations of fumarate entering the cell through an antiporter with succinate [25].

Comparing the metabolic networks of two phenotypes that both utilize the same TEA, but are not in the same cluster, can help elucidate differences in the reactions utilized between phenotypes with distinctive growth efficiencies. For example, the oxidized and reduced form of a ferrodoxin protein, important in electron transfer for many metabolic reactions, is the most significant reporter metabolite between clusters 1 and 2 followed by alpha-ketoglutarate (AKG), an enzyme involved in the TCA cycle and amino acid production. With more AKG utilized in the TCA cycle as opposed to amino acid production, more ATP is produced allowing for more efficient growth. These results highlight differences between reaction networks that lead to differences in growth efficiencies that can be investigated and experimentally validated.

Near-optimal modes

Phenotypes are arranged into clusters with many nearly overlapping in growth efficiencies (Fig. 5.1). Previous studies have shown that organisms may not maximize biomass production alone or one specific objective function, but exists along a pareto-optimum where multiple objective functions are optimized [8], such that a microbe cannot optimize one objective function without lowering the optimality of another. One goal function applicable to microbes takes into account the transition cost for changing their metabolic machinery when adapting to variable environmental conditions [8]. For example, an organism can simultaneously optimize biomass production while minimizing changes in its intracellular machinery by utilizing reactions that are beneficial to the organism under multiple environmental conditions.

EFMA provides the means to analyze multiple realizations of the reaction network for an organism under one set of environmental conditions. For example, the most optimal phenotype for acetate growth on iron is located in cluster 1 while the most optimal phenotype for growth on fumarate is in cluster 11 (Fig. 5.1). However, an organism subjected to fluctuating conditions may exist in a less, but near-optimal phenotype that simultaneously minimizes the changes in its metabolic machinery between fumarate and iron as a TEA. Therefore, to identify phenotypes that may be best adapted to variable environmental conditions, one can take into account both the optimality and similarity of two phenotypes.

When only one TEA is present, a microbe generally can benefit from a strategy that maximizes biomass production; for example, when *G. sulfurreducens* is found growing on iron, its typical TEA. When there are variations in the presence of fumarate, *G. sulfurreducens* will preferentially utilize it as TEA, requiring a change in its metabolic machinery. When growing in variable conditions, the microbe can optimize *N*, which maximizes growth efficiency while

minimizing the transition cost from one metabolic state to another using different TEAs. The two indicated phenotypes in Figure 5.1 are the most optimal in clusters 1 and 12. Both maximize biomass production on their respective TEA and are also most similar in their reaction networks.

These phenotypes are less efficient than the most optimal phenotypes in their respective clusters as they are not closest to the origin. Therefore, for cluster 1 reporter metabolites were determined for the phenotype with the highest growth efficiency (i.e. closest to the origin) and the phenotype in cluster 1 that optimizes *N* (Table 5.1). For cluster 1, the two phenotypes compared demonstrate differences in acetyl-phosphate usage, which affects if acetate taken up by the cell is used for energy metabolism through the TCA cycle or biomass production. AKG, another key player in the TCA cycle, was utilized differently between phenotypes, though to a lesser extent than when comparing clusters 1 and 2. Similarly, reporter metabolites were determined for the phenotype with the highest growth efficiency and the phenotype predicted to optimize *N* in cluster 12. For these phenotypes utilizing fumarate as TEA, the reactions involved with AKG were most significantly adjusted, followed by folate, which is involved in NADPH production.

Conclusions

EFMA was successfully applied to a full reaction network description of *Geobacter sulfurreducens*, as opposed to a simplified reaction network description, as is more commonly done. This allows for a comparison of all potential metabolic networks determined from EFMA and FBA. Differences in the phenotypes highlight experimentally measureable differences in the reactions and enzymes used, which ultimately correspond to variations in the growth efficiencies predicted.

In a dynamic environment, *Geobacter* may exist at less than optimal phenotypes for growth, but account for changes in the metabolic machinery needed to utilize different terminal electron acceptors. Under fluctuating availability of terminal electron acceptors, our analysis suggests a 7% less efficient growth than the most optimal phenotype, a difference that is difficult to detect in laboratory experiments. However, the predicted phenotypes can be experimentally validated using transcriptomic data. Measurements of mRNA levels, a proxy for enzyme activity, may allow one to constrain the possible phenotypes determined from EFMA, increasing the predictive capability of these metabolic models.

References

1. Falkowski PG, Fenchel T, Delong EF: **The microbial engines that drive Earth's biogeochemical cycles.** *Science* 2008, **320:**1034-1039.
2. Mah TF: **Biofilm-specific antibiotic resistance.** *Future Microbiol* 2012, **7:**1061-1072.
3. Rabaey K, Lissens G, Siciliano SD, Verstraete W: **A microbial fuel cell capable of converting glucose to electricity at high rate and efficiency.** *Biotechnol Lett* 2003, **25:**1531-1535.
4. Wall JD, Krumholz LR: **Uranium reduction.** *Annu Rev Microbiol* 2006, **60:**149-166.
5. Buescher JM, Liebermeister W, Jules M, Uhr M, Muntel J, Botella E, Hessling B, Kleijn RJ, Le Chat L, Lecointe F, et al: **Global Network Reorganization During Dynamic Adaptations of Bacillus subtilis Metabolism.** *Science* 2012, **335:**1099-1103.
6. Jozefczuk S, Klie S, Catchpole G, Szymanski J, Cuadros-Inostroza A, Steinhauser D, Selbig J, Willmitzer L: **Metabolomic and transcriptomic stress response of Escherichia coli.** *Mol Syst Biol* 2010, **6:**364.
7. Mitchell A, Romano GH, Groisman B, Yona A, Dekel E, Kupiec M, Dahan O, Pilpel Y: **Adaptive prediction of environmental changes by microorganisms.** *Nature* 2009, **460:**220-224.
8. Schuetz R, Zamboni N, Zampieri M, Heinemann M, Sauer U: **Multidimensional Optimality of Microbial Metabolism.** *Science* 2012, **336:**601-604.
9. Varma A, Palsson BO: **Metabolic Flux Balancing - Basic Concepts, Scientific and Practical Use.** *Bio-Technol* 1994, **12:**994-998.
10. Schuetz R, Kuepfer L, Sauer U: **Systematic evaluation of objective functions for predicting intracellular fluxes in Escherichia coli.** *Mol Syst Biol* 2007, **3:**119.

11. Carlson R, Srienc F: **Fundamental Escherichia coli biochemical pathways for biomass and energy production: Creation of overall flux states.** *Biotechnol Bioeng* 2004, **86:**149-162.

12. Carlson R, Srienc F: **Fundamental Escherichia coli biochemical pathways for biomass and energy production: Identification of reactions.** *Biotechnol Bioeng* 2004, **85:**1-19.

13. Taffs R, Aston JE, Brileya K, Jay Z, Klatt CG, McGlynn S, Mallette N, Montross S, Gerlach R, Inskeep WP, et al: **In silico approaches to study mass and energy flows in microbial consortia: a syntrophic case study.** *Bmc Syst Biol* 2009, **3:**114.

14. Carlson RP: **Metabolic systems cost-benefit analysis for interpreting network structure and regulation.** *Bioinformatics* 2007, **23:**1258-1264.

15. Zhuang K, Izallalen M, Mouser P, Richter H, Risso C, Mahadevan R, Lovley DR: **Genome-scale dynamic modeling of the competition between Rhodoferax and Geobacter in anoxic subsurface environments.** *Isme J* 2011, **5:**305-316.

16. Lovley DR, Phillips EJP, Gorby YA, Landa ER: **Microbial Reduction of Uranium.** *Nature* 1991, **350:**413-416.

17. Mahadevan R, Bond DR, Butler JE, Esteve-Núñez A, Coppi MV, Palsson BO, Schulling CH, Lovley DR: **Characterization of metabolism in the Fe(III)-reducing organism Geobacter sulfurreducens by constraint-based modeling.** *Appl Environ Microbiol* 2006, **72:**1558-1568.

18. Famili I, Palsson BO: **Systemic metabolic reactions are obtained by singular value decomposition of genome-scale stoichiometric matrices.** *J Theor Biol* 2003, **224:**87-96.

19. Schuster S, Fell DA, Dandekar T: **A general definition of metabolic pathways useful for systematic organization and analysis of complex metabolic networks.** *Nat Biotechnol* 2000, **18:**326-332.

20. Schuster S, Hilgetag C, Fell D: **Detecting elementary modes of functioning in metabolic networks.** *Mod Tr Biothermokin* 1994, **3:**103-105.

21. Klamt S, Saez-Rodriguez J, Gilles ED: **Structural and functional analysis of cellular networks with CellNetAnalyzer.** *Bmc Syst Biol* 2007, **1:**2.

22. Terzer M, Stelling J: **Large-scale computation of elementary flux modes with bit pattern trees.** *Bioinformatics* 2008, **24:**2229-2235.

23. Patil KR, Nielsen J: **Uncovering transcriptional regulation of metabolism by using metabolic network topology.** *P Natl Acad Sci USA* 2005, **102:**2685-2689.

24. Esteve-Núñez A, Rothermich M, Sharma M, Lovley DR: **Growth of Geobacter sulfurreducens under nutrient-limiting conditions in continuous culture.** *Environ Microbiol* 2005, **7:**641-648.

25. Butler JE, Glaven RH, Esteve-Núñez A, Nunez C, Shelobolina ES, Bond DR, Lovley DR: **Genetic characterization of a single bifunctional enzyme for fumarate reduction and succinate oxidation in Geobacter sulfurreducens and engineering of fumarate reduction in Geobacter metallireducens.** *J Bacteriol* 2006, **188:**450-455.

Table 5.1: For clusters 1 and 11 (see Fig. 5.1), reporter metabolites were determined between the phenotype most efficient at growth in that cluster and the phenotype that optimizes *N*. Similarly, cluster 11, which use fumarate as TEA, had reporter metabolites determined between the most efficient phenotype and phenotype that optimizes *N*.

Cluster 1	Cluster 11
nh3	akg
nh4	fol
h	pppi
acser	amp
actp	h
cys-L	for
fol	ctp
pppi	dhf
adp	so4[e]
akg	nh4

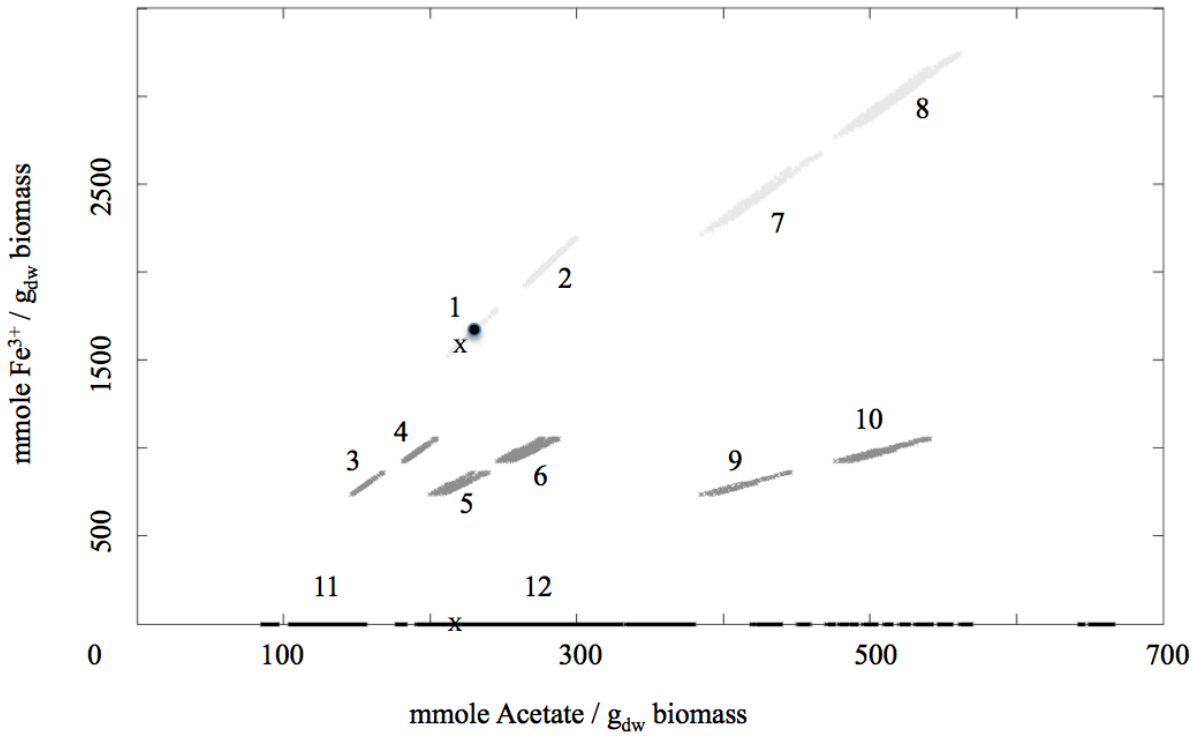

Figure 5.1: Visualization of the EFMA phenotypes. Each circle corresponds to one of the EFMA phenotypes utilizing different TEAs (light grey for iron, black for fumarate, and dark grey for iron and fumarate). The x-axis depicts the mmoles of acetate needed to produce 1 gdw biomass while the y-axis gives the mmoles for Fe^{3+} needed as TEA. Distinct groups of phenotypes are seen with many visually looking close to optimal for each cluster. The phenotypes along the x-axis utilize fumarate as the TEA (i.e. no Fe^{3+}). The black circle corresponds to the reaction network from Mahadevan et al. [17], which is indistinguishable from the flux balance model constructed from the curated network used in EFMA. "X"s correspond to the approximate position of the phenotypes that are a combination of most optimal and similar to each other (see text for complete description). Numbers represent cluster labeling. Note that phenotypes utilizing fumarate that required more than 700 mmol acetate / gdw biomass were omitted.

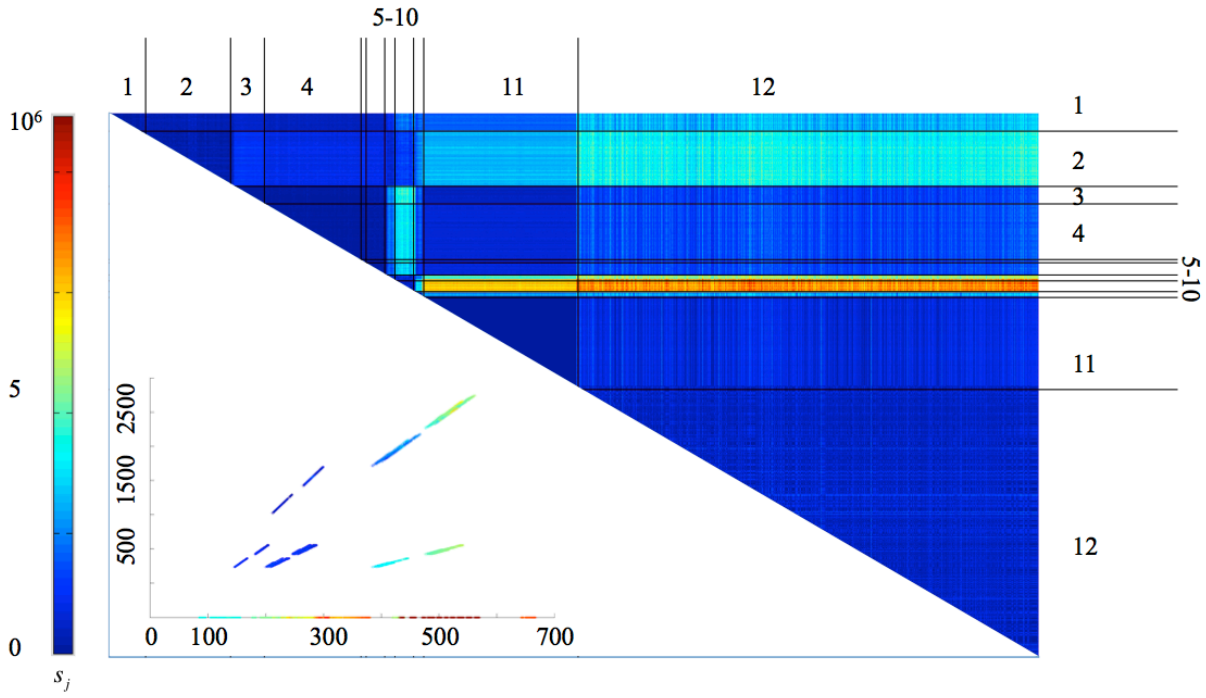

Figure 5.2: Comparison of the magnitudes of the fluxes between each EFMA phenotype. Numbers represent cluster labels as in Fig. 5.1. Note that only every 100th phenotype is compared for computational feasibility. Inset. (bottom left) Difference between the sum of the magnitude of the fluxes between the FB and each EFMA phenotypes. Note that clusters 5-10 contain fewer phenotypes than other clusters.

CHAPTER 6

SUMMARY

The role of microbes in porous media

Microbial metabolism in the environment is central to elemental cycling. However, due to the complexity of the natural environment, the microbial processes, and the vast range of scales connecting individual cells and macroscopic system characteristics, our ability to formulate meaningful models with predictive power is often limited. In an effort to address some of the existing challenges, this thesis focused on several aspects of biogeochemical dynamics in porous media, including ways to formulate microbial metabolism that integrate knowledge gained in Systems Biology and its implementation into reaction transport models. In addition, microbially mediated carbon cycling was studied in two specific environments, one representing a contaminated groundwater setting to investigate the impact of reaction network formulations and the other a freshwater marsh to investigate methane production.

Modeling biogeochemical dynamics

In Chapter 2, the complexity of reaction network formulations, including explicit representations of microbial dynamics, was investigated in models representative of a phenol contaminant plume. We evaluated the importance of pore distribution on organic matter respiration in a porous medium environment by performing spatially explicit simulations of microbial metabolism at the sub-millimeter scale. Models indicated that while some heterogeneity is

observed for flow rates, distributions of microbes and dissolved organic substrates remain relatively homogenous. We also assessed the impact of a comprehensive reaction network description for a phenolic contaminant plume, and compared the findings to a setting describing organic matter breakdown in a coastal marine sediment in the eastern Skagerrak. This comparison revealed the importance of reactions recycling reduced metabolites at redox interfaces, leading to a competition for oxidants. When the spatio-temporal dynamics of microbial groups were accounted for, our simulations showed the importance of the interplay between reaction energetics and nutrient limitations.

We found that a description of subsurface processes may not always require an explicit representation of microbial biomass, particularly in settings characterized by minimal variations in microbial activity. The need to account for a range of feedback mechanisms between microbial activity and environmental conditions suggests that understanding microbial requirements may be central to quantify controls on bioremediation in the field.

In Chapter 3, we used two complimentary, yet fundamentally different techniques to determine rates of organic matter breakdown in freshwater sediments. These methodologies provided alternative ways to determine process rates based upon the different types of data available. One technique utilized species concentrations over time, while the other technique required knowledge on radiotracer-based rates for methanogenesis. Results from different formulations of the reaction kinetics were able to match the time series concentration data. Although they utilize the same reaction network description of OM breakdown, several process rates between the techniques were significantly different, which highlights the importance of having a balanced data set that covers all fluxes in and out of the system of interest.

Formulating a model of microbial metabolism

In Chapter 4, through the development of a dynamic cell model of *Geobacter sulfurreducens*, we showed that a kinetic representation of key components of cell metabolism matched microbial growth dynamics observed in chemostat experiments under varying environmental conditions and led to results similar to those from a comprehensive flux balance model.

Coupling the kinetic cell model to the environment by expressing substrate uptake rates depending on intra- and extracellular substrate concentrations, 2D reactive transport simulations of an aquifer were performed. They illustrated that a proper representation of growth efficiency as a function of substrate availability is a determining factor for the spatial distribution of microbial populations in a porous medium. Also, it was shown that simplified model representations of microbial dynamics in the subsurface that only depended on extracellular conditions could be derived by properly parameterizing emerging properties of the kinetic cell model.

To assess the role of microbial dynamics in the environment, an acetate plume was studied in a heterogeneous porous medium, for which simulations with a full coupling between the environment and the cell model were contrasted with several simplified parameterizations. They illustrated that a proper representation of growth efficiency as a function of substrate availability is a determining factor for the spatial distribution of microbial populations in a porous medium.

In Chapter 5, elementary flux mode analysis was successfully applied to a full reaction network description of *Geobacter sulfurreducens* to predict phenotypic plasticity. All potential phenotypes of the organism were determined, which covered a range of growth efficiencies on iron and fumarate as terminal electron acceptors. In a dynamic environment, results indicated the

potential for *Geobacter* to exist at less than the most efficient phenotype for growth, but rather phenotypes that maximized growth while also minimization the changes in the metabolic machinery needed to utilize different terminal electron acceptors. These phenotypes were analyzed to determine the reactions prevalent in their metabolic networks, which allows for experimental validation of the phenotypes through e.g. linking of microbial growth dynamics to transcriptomic data.

APPENDIX A

PARAMETERIZATION OF THE *GEOBACTER SULFURREDUCENS* MODEL UTILIZING FLUX BALANCE AND ELEMENTARY FLUX MODE ANALYSIS

Introduction:

This purpose of this appendix is to provide the parameterization necessary for the models of *Geobacter sulfurreducens* presented in Chapters 4 and 5. Included are the reactions and metabolites utilized as well as supplementary results from Chapter 5.

Table A.1: Reaction list for the elementary flux mode and flux balance models presented in Chapters 4 and 5. Reactions are originally taken from Mahadevan et al. [1] with modifications described in "Note". "Heavy metal toxicity mediation" reactions were considered unimportant in the environment being investigated and were therefore removed (HM). "Futile Reactions" refer to those reactions that were removed because a substrate is taken up and is no longer utilized or subsequently sent out of the cell. "External metabolite reactions" are those reactions that were removed because only external, unbalanced metabolites were considered (EM). Reactions labeled "Potential alternative carbon sources or electron donors" were either removed to prevent uptake of an alternative carbon source (RAC) or were modified to prevent uptake into the cell with export from the cell allowed (MAC). "Growth associated metabolites" are those reactions that involve simple diffusive uptake of a metabolite, which is only subsequently used in the biomass growth reaction. This reaction was removed and the metabolite was change to external (GR)."Simple uptake of metabolites" are those reactions where metabolites are taken up through simple diffusion. These reactions were removed with the internal metabolites made external. "Unmodified reactions" are those taken directly from Mahadevan et al. [1]

Abbreviation	Reaction Equation	Note	Lower Bound	Upper Bound
Heavy metal toxicity mediation				
COBALTt5	cobalt2[c] <==> cobalt2[e]	HM	-Infinity	Infinity
Coabc	atp[c] + cobalt2[e] + h2o[c] --> adp[c] + cobalt2[c] + h[c] + pi[c]	HM	0	Infinity
Futile Reactions				
Cuabc	atp[c] + cu2[e] + h2o[c] --> adp[c] + cu2[c] + h[c] + pi[c]	F	0	Infinity
ZN2abc1	atp[c] + h2o[c] + zn2[c] --> adp[c] + h[c] + pi[c] + zn2[e]	F	0	Infinity
ZN2abc2	atp[c] + h2o[c] + zn2[e] --> adp[c] + h[c] + pi[c] + zn2[c]	F	0	Infinity
CD2abc1	atp[c] + cd2[c] + h2o[c] --> adp[c] + cd2[e] + h[c] + pi[c]	F	0	Infinity

CD2abc2	atp[c] + cd2[e] + h2o[c] --> adp[c] + cd2[c] + h[c] + pi[c]	F	0	Infinity
Clt	cl[e] <==> cl[c]	F	-Infinity	Infinity
NIabc	atp[c] + h2o[c] + ni2[e] --> adp[c] + h[c] + ni2[c] + pi[c]	F	0	Infinity
NIt5	ni2[c] <==> ni2[e]	F	-Infinity	Infinity
MOBDabc	atp[c] + h2o[c] + mobd[e] --> adp[c] + h[c] + mobd[c] + pi[c]	F	0	Infinity
MNabc	atp[c] + h2o[c] + mn2[e] --> adp[c] + h[c] + mn2[c] + pi[c]	F	0	Infinity
OXFOt4	for[c] + oxa[e] <==> for[e] + oxa[c]	F	-Infinity	Infinity
External metabolite reactions				
PSULF	h2s[e] + s[e] <==> (2) h[e] + ss[e]	EM	-Infinity	Infinity
PSRED3	(2) h[e] + mql7[c] + ss[e] --> (2) h2s[e] + mqn7[c]	EM	0	Infinity
Potential alternative carbon sources or electron donors				
GLNabc	atp[c] + gln-L[e] + h2o[c] --> adp[c] + gln-L[c] + h[c] + pi[c]	RAC	0	Infinity
CITt6	cit[e] + h[e] <==> cit[c] + h[c]	MAC	-Infinity	Infinity
GLYt6	gly[e] + h[e] <==> gly[c] + h[c]	MAC	-Infinity	Infinity
ILEabc	atp[c] + h2o[c] + ile-L[e] --> adp[c] + h[c] + ile-L[c] + pi[c]	RAC	0	Infinity
ILEt6	h[e] + ile-L[e] <==> h[c] + ile-L[c]	MAC	-Infinity	Infinity
L-LACt4	h[e] + lac-L[e] --> h[c] + lac-L[c]	RAC	0	Infinity
LDH_L	[c] : lac-L + nad <==> h + nadh + pyr	RAC	-Infinity	Infinity
LEUabc	atp[c] + h2o[c] + leu-L[e] --> adp[c] + h[c] + leu-L[c] + pi[c]	RAC	0	Infinity
LEUt6	h[e] + leu-L[e] <==> h[c] + leu-L[c]	MAC	-Infinity	Infinity
MALt6	h[e] + mal-L[e] <==> h[c] + mal-L[c]	MAC	-Infinity	Infinity
PROt5	na1[e] + pro-L[e] <==> na1[c] + pro-L[c]	MAC	-Infinity	Infinity
URAt6	h[e] + ura[e] <==> h[c] + ura[c]	MAC	-Infinity	Infinity
VALabc	atp[c] + h2o[c] + val-L[e] --> adp[c] + h[c] + pi[c] + val-L[c]	RAC	0	Infinity
VALt6	h[e] + val-L[e] <==> h[c] + val-L[c]	MAC	-Infinity	Infinity
FORt2	for[e] + h[e] <==> for[c] + h[c]	MAC	-Infinity	Infinity
H2td	h2[c] <==> h2[e]	MAC	-Infinity	Infinity
Growth associated metabolites				
MGt5	mg2[c] <==> mg2[e]	GR	-Infinity	Infinity
Simple uptake of metabolite				
N2t	n2[c] <==> n2[e]	RE	-Infinity	Infinity

H2Ot5	h2o[e] <==> h2o[c]	RE	-Infinity	Infinity
CO2t	co2[e] <==> co2[c]	RE	-Infinity	Infinity
Unmodified reactions				
AACPAT	[c] : accoa + acp --> acacp + coa	U	0	Infinity
ACBIPGT	[c] : adcobap + gtp + h --> adgcoba + ppi	U	0	Infinity
ACCOAC	[c] : accoa + atp + hco3 --> adp + h + malcoa + pi	U	0	Infinity
ACGK	[c] : acglu + atp --> acg5p + adp	U	0	Infinity
ACGS	[c] : accoa + glu-L --> acglu + coa + h	U	0	Infinity
ACHBS	[c] : 2obut + h + pyr --> 2ahbut + co2	U	0	Infinity
ACKr	[c] : ac + atp <==> actp + adp	U	-Infinity	Infinity
ACLS	[c] : h + (2) pyr --> alac-S + co2	U	0	Infinity
ACMAT1	[c] : acacp + h + malacp --> aaacp + acp + co2	U	0	Infinity
ACNPLYS	[c] : acmana + h2o + pep --> acnam + pi	U	0	Infinity
ACONT	[c] : cit <==> icit	U	-Infinity	Infinity
ACOTA	[c] : acorn + akg <==> acg5sa + glu-L	U	-Infinity	Infinity
ACt2	ac[e] + h[e] --> ac[c] + h[c]	U	-Infinity	Infinity
ADCL	[c] : 4adcho --> 4abz + h + pyr	U	0	Infinity
ADCOBAK	[c] : adcoba + atp --> adcobap + adp + h	U	0	Infinity
ADCOBAS	[c] : 1ap2ol + adcobhex --> adcoba + h2o	U	0	Infinity
ADCOBHEXS	[c] : adcobdam + (4) atp + (4) gln-L + (4) h2o --> adcobhex + (4) adp + (4) glu-L + (4) h + (4) pi	U	0	Infinity
ADCS	[c] : chor + gln-L --> 4adcho + glu-L	U	0	Infinity
ADK1	[c] : amp + atp <==> (2) adp	U	-Infinity	Infinity
ADK2	[c] : amp + pppi <==> adp + ppi	U	-Infinity	Infinity
ADNK1	[c] : adn + atp --> adp + amp + h	U	0	Infinity
ADOCBLS	[c] : adgcoba + (0.5) h + (0.5) nad + rdmbzi --> cobamcoa + gmp + (0.5) nadh	U	0	Infinity
ADPT	[c] : ade + prpp --> amp + ppi	U	0	Infinity
ADSK	[c] : aps + atp --> adp + h + paps	U	0	Infinity
ADSL1	[c] : dcamp --> amp + fum	U	0	Infinity
ADSL2	[c] : 25aics --> aicar + fum	U	0	Infinity
ADSS	[c] : asp-L + gtp + imp --> dcamp + gdp + (2) h + pi	U	0	Infinity

AGPAT	[c] : 12dag3p + coa --> 1ag3p + acoa	U	0	Infinity
AGPR	[c] : acg5sa + nadp + pi <==> acg5p + h + nadph	U	-Infinity	Infinity
AHC	[c] : ahcys + h2o <==> adn + hcys-L	U	-Infinity	Infinity
AHCYSNS	[c] : ahcys + h2o --> ade + rhcys	U	0	Infinity
AHMMPS	[c] : air + h2o --> 4ahmmp + gcald + (0.5) o2 + pi	U	0	Infinity
AICART	[c] : 10fthf + aicar <==> fprica + thf	U	-Infinity	Infinity
AIRC	[c] : air + co2 --> 5aizc + h	U	0	Infinity
AKGD	[c] : akg + coa + nad --> co2 + nadh + succoa	U	0	Infinity
ALAALA	[c] : (2) ala-D + atp <==> adp + alaala + h + pi	U	-Infinity	Infinity
ALAD_L	[c] : ala-L + h2o + nad --> h + nadh + nh4 + pyr	U	0	Infinity
ALAR	[c] : ala-L <==> ala-D	U	-Infinity	Infinity
ALATA_L	[c] : akg + ala-L <==> glu-L + pyr	U	-Infinity	Infinity
ALDD2x	[c] : acald + h2o + nad --> ac + (2) h + nadh	U	0	Infinity
AMAA	[c] : acmama + h2o --> acmam + ala-L	U	0	Infinity
AMAOT	[c] : 8aonn + amet <==> amob + dann	U	-Infinity	Infinity
AMMQT8_2	[c] : 2dmmq8 + amet --> ahcys + h + mqn8	U	0	Infinity
ANPRT	[c] : anth + prpp --> ppi + pran	U	0	Infinity
ANS1	[c] : chor + gln-L --> anth + glu-L + h + pyr	U	0	Infinity
AOXS	[c] : ala-L + h + pmcoa <==> 8aonn + co2 + coa	U	-Infinity	Infinity
APAT	[c] : accoa + h2o + thdp <==> acamoxm + coa	U	-Infinity	Infinity
APRAUR	[c] : 5apru + h + nadph --> 5aprbu + nadp	U	0	Infinity
ARGDC	[c] : arg-L + h --> agm + co2	U	0	Infinity
ARGSL	[c] : argsuc <==> arg-L + fum	U	-Infinity	Infinity
ARGSS	[c] : asp-L + atp + citr-L --> amp + argsuc + h + ppi	U	0	Infinity
ASAD	[c] : aspsa + nadp + pi <==> 4pasp + h + nadph	U	-Infinity	Infinity
ASNS1	[c] : asp-L + atp + gln-L + h2o --> amp + asn-L + glu-L + h + ppi	U	0	Infinity
ASP1DC	[c] : asp-L + h --> ala-B + co2	U	0	Infinity
ASPCT	[c] : asp-L + cbp --> cbasp + h + pi	U	0	Infinity
ASPK	[c] : asp-L + atp <==> 4pasp + adp	U	-Infinity	Infinity
ASPO1	[c] : asp-L + nad --> (2) h + iasp + nadh	U	0	Infinity
ASPT	[c] : asp-L --> fum + nh4	U	0	Infinity

ASPTA1	[c] : akg + asp-L <==> glu-L + oaa	U	-Infinity	Infinity
ATO	[c] : ac + succoa --> accoa + succ	U	0	Infinity
ATPM	[c] : atp + h2o --> adp + h + pi	U	0.45	0.45
ATPPRT	[c] : atp + prpp --> ppi + prbatp	U	0	Infinity
ATPS4	adp[c] + (4) h[e] + pi[c] --> atp[c] + (3) h[c] + h2o[c]	U	0	Infinity
BPNT	[c] : h2o + pap --> amp + pi	U	0	Infinity
BTMAT1	[c] : 2beacp + h + nadh --> butacp + nad	U	0	Infinity
BTS	[c] : dtbt + (2) s --> btn + h2s	U	0	Infinity
CA2abc	atp[c] + ca2[e] + h2o[c] --> adp[c] + ca2[c] + h[c] + pi[c]	U	0	Infinity
CA2abc1	atp[c] + ca2[c] + h2o[c] --> adp[c] + ca2[e] + h[c] + pi[c]	U	0	Infinity
CBMK	[c] : atp + cbm --> adp + cbp	U	0	Infinity
CBPS	[c] : (2) atp + gln-L + h2o + hco3 --> (2) adp + cbp + glu-L + (2) h + pi	U	0	Infinity
CDGPT	[c] : cdpdag + glyc3p --> cmp + h + pglyp	U	0	Infinity
CDPDSP	[c] : cdpdag + ser-L --> cmp + h + ps	U	0	Infinity
CDPMEK	[c] : 4c2me + atp --> 2p4c2me + adp + h	U	0	Infinity
CHORM	[c] : chor --> pphn	U	0	Infinity
CHORS	[c] : 3psme --> chor + pi	U	0	Infinity
CLPNS	[c] : cdpdag + pgly --> cdlp + cmp + h	U	0	Infinity
CO1DAMAT	[c] : atp + co1dam + h2o + (0.5) nadh --> adcobdam + (0.5) h + (0.5) nad + pi + ppi	U	0	Infinity
CO2DAMR	[c] : (2) co2dam + nadh --> (2) co1dam + h + nad	U	0	Infinity
COBAT	[c] : cobamcoa + pi + ppi <==> atp + cbl1 + h + (0.5) h2o2	U	-Infinity	Infinity
CODH	[c] : CO + fdxo-4:2 + h2o --> co2 + fdxr-4:2 + (2) h	U	0	Infinity
CPPPGO	[c] : cpppg3 + (2) h + o2 --> (2) co2 + (2) h2o + pppg9	U	0	Infinity
CPPPGOAN	[c] : (2) amet + cpppg3 + (2) fdxo-4:2 + (2) nadph --> (2) co2 + (2) dad-5 + (2) fdxr-4:2 + (2) h + (2) met-L + (2) nadp + pppg9	U	0	Infinity
CRET	[c] : crtn + h2o --> creat	U	0	Infinity
CS	[c] : accoa + h2o + oaa --> cit + coa + h	U	0	Infinity
CTL	[c] : cysth-L + h2o --> 2obut + cys-L + h + nh3	U	0	Infinity
CTPS1	[c] : atp + nh3 + utp --> adp + ctp + h + pi	U	0	Infinity
CTPS2	[c] : atp + gln-L + h2o + utp --> adp + ctp + glu-L + (2) h + pi	U	0	Infinity
CYCPO	[c] : (2) focytc + (2) h + h2o2 --> (2) ficytc + (2) h2o	U	0	Infinity

CYOR1m	(2) ficytc[c] + mql7[c] --> (2) focytc[c] + h[e] + h[c] + mqn7[c]	U	0	Infinity
CYSS	[c] : acser + h2s --> ac + cys-L + h	U	0	Infinity
CYSTL	[c] : cysth-L + h2o --> hcys-L + nh4 + pyr	U	0	Infinity
CYSTS	[c] : hcys-L + ser-L --> cysth-L + h2o	U	0	Infinity
CYTK1	[c] : atp + cmp <==> adp + cdp	U	-Infinity	Infinity
CYTK2	[c] : atp + dcmp <==> adp + dcdp	U	-Infinity	Infinity
DADK	[c] : atp + damp <==> adp + dadp	U	-Infinity	Infinity
DAGK	[c] : 12dgr + atp --> 12dag3p + adp + h	U	0	Infinity
DAHPS	[c] : e4p + h2o + pep --> 2dda7p + pi	U	0	Infinity
DAPDC	[c] : 26dap-M + h --> co2 + lys-L	U	0	Infinity
DAPE	[c] : 26dap-LL <==> 26dap-M	U	-Infinity	Infinity
DB4PS	[c] : ru5p-D --> db4p + for + h	U	0	Infinity
DBTS	[c] : atp + co2 + dann --> adp + dtbt + (3) h + pi	U	0	Infinity
DDMAT5	[c] : 2tddacp + h + nadh --> ddeacp + nad	U	0	Infinity
DEMAT4	[c] : 2tdeacp + h + nadh --> decacp + nad	U	0	Infinity
DGK1	[c] : atp + dgmp <==> adp + dgdp	U	-Infinity	Infinity
DGTPH	[c] : dgtp + h2o --> dgsn + pppi	U	0	Infinity
DHAD1	[c] : 23dhmb --> 3mob + h2o	U	0	Infinity
DHAD2	[c] : 23dhmp --> 3mop + h2o	U	0	Infinity
DHDPRy	[c] : 23dhdp + h + nadph --> nadp + thdp	U	0	Infinity
DHDPS	[c] : aspsa + pyr --> 23dhdp + h + (2) h2o	U	0	Infinity
DHFOR2	[c] : dhf + nadp <==> fol + nadph	U	-Infinity	Infinity
DHFOR3	[c] : fol + h + (2) nadph <==> (2) nadp + thf	U	-Infinity	Infinity
DHFR	[c] : dhf + h + nadph <==> nadp + thf	U	-Infinity	Infinity
DHFS	[c] : atp + dhpt + glu-L --> adp + dhf + h + pi	U	0	Infinity
DHNAOT	[c] : dhna + nad + octdp --> 2dmmq8 + co2 + nadh + ppi	U	0	Infinity
DHORD4	[c] : dhor-S + mqn7 <==> mql7 + orot	U	-Infinity	Infinity
DHORTS	[c] : dhor-S + h2o <==> cbasp + h	U	-Infinity	Infinity
DHPPDA	[c] : 25dhpp + h2o --> 5apru + nh3	U	0	Infinity
DHPS1	[c] : 2ahhmp + 4abz --> dhpt + h2o	U	0	Infinity
DHQD1	[c] : 3dhq <==> 3dhsk + h2o	U	-Infinity	Infinity

DHQS	[c] : 2dda7p --> 3dhq + pi	U	0	Infinity
DMATT	[c] : dmpp + ipdp --> grdp + ppi	U	0	Infinity
DMOCT	[c] : ctp + kdo --> ckdo + ppi	U	0	Infinity
DMPPS	[c] : h + h2mb4p + nadh --> dmpp + h2o + nad	U	0	Infinity
DPCOAK	[c] : atp + dpcoa --> adp + coa + h	U	0	Infinity
DPR	[c] : 2dhp + h + nadph --> nadp + pant-R	U	0	Infinity
DTMPK	[c] : atp + dtmp <==> adp + dtdp	U	-Infinity	Infinity
DUTPDP	[c] : dutp + h2o --> dump + h + ppi	U	0	Infinity
DXPRI	[c] : dxyl5p + h + nadph <==> 2me4p + nadp	U	-Infinity	Infinity
DXPS	[c] : g3p + h + pyr --> co2 + dxyl5p	U	0	Infinity
ENO	[c] : 2pg <==> h2o + pep	U	-Infinity	Infinity
EPPP	[c] : h2o + polypi --> (2) h + pi	U	0	Infinity
FBA	[c] : fdp <==> dhap + g3p	U	-Infinity	Infinity
FBP	[c] : fdp + h2o --> f6p + pi	U	0	Infinity
FCLT	[c] : fe2 + ppp9 --> h + pheme	U	0	Infinity
FDH	[c] : for + nad --> co2 + nadh	U	0	Infinity
FE2abc	atp[c] + fe2[e] + h2o[c] --> adp[c] + fe2[c] + h[c] + pi[c]	U	0	Infinity
FERCYT	fe3[e] + focytc[c] --> fe2[e] + ficytc[c]	U	0	Infinity
FMNAT	[c] : atp + fmn + h --> fad + ppi	U	0	Infinity
FNOR	[c] : fdxr-4:2 + h + nadp <==> fdxo-4:2 + nadph	U	0	Infinity
FOMETR	[c] : 5fothf + h <==> h2o + methf	U	-Infinity	Infinity
FRD5	[c] : mqn7 + succ <==> fum + mql7	U	-Infinity	Infinity
FRTT	[c] : frdp + ipdp --> ggdp + ppi	U	0	Infinity
FUM	[c] : fum + h2o <==> mal-L	U	-Infinity	Infinity
FUMt4	fum[e] + (3) h[e] --> fum[c] + (3) h[c]	U	0	0
G1Dx	[c] : glc-D + nad --> g15lac + h + nadh	U	0	Infinity
G1Dy	[c] : glc-D + nadp --> g15lac + h + nadph	U	0	Infinity
G1PACT	[c] : accoa + gam1p --> acgam1p + coa + h	U	0	Infinity
G1PTMT	[c] : dttp + g1p + h --> dtdpglc + ppi	U	0	Infinity
G1SAT	[c] : glu1sa <==> 5aop	U	-Infinity	Infinity
G3PD1	[c] : glyc3p + nad <==> dhap + h + nadh	U	0	Infinity

G3PD2	[c] : glyc3p + nadp <==> dhap + h + nadph	U	0	Infinity
G3PD4	[c] : glyc3p + mqn7 --> dhap + mql7	U	0	Infinity
G5SADs	[c] : glu5sa <==> 1pyr5c + h + h2o	U	-Infinity	Infinity
G5SD	[c] : glu5p + h + nadph --> glu5sa + nadp + pi	U	0	Infinity
GALT	[c] : gal1p + h + utp <==> ppi + udpgal	U	-Infinity	Infinity
GALU	[c] : g1p + h + utp <==> ppi + udpg	U	-Infinity	Infinity
GAPD	[c] : g3p + nad + pi <==> 13dpg + h + nadh	U	-Infinity	Infinity
GAPDy1	[c] : g3p + h2o + nadp --> 3pg + (2) h + nadph	U	0	Infinity
GARFT	[c] : 10fthf + gar <==> fgam + h + thf	U	-Infinity	Infinity
GCCa	[c] : gly + h + lpro --> alpro + co2	U	0	Infinity
GCCb	[c] : alpro + thf --> dhlpro + mlthf + nh4	U	0	Infinity
GCCc	[c] : dhlpro + nad --> h + lpro + nadh	U	0	Infinity
GCOP	[c] : atp + glycogen + h2o --> adp + g1p + h	U	0	Infinity
GDMANE	[c] : gdpddm <==> gdpofuc	U	-Infinity	Infinity
GDPMD	[c] : gdpman --> gdpddm + h2o	U	0	Infinity
GF6PTA	[c] : f6p + gln-L --> gam6p + glu-L	U	0	Infinity
GGTT	[c] : ggdp + ipdp --> pendp + ppi	U	0	Infinity
GHMT	[c] : ser-L + thf <==> gly + h2o + mlthf	U	-Infinity	Infinity
GK1	[c] : atp + gmp <==> adp + gdp	U	-Infinity	Infinity
GLCS1	[c] : adpglc --> adp + glycogen + h	U	0	Infinity
GLGC	[c] : atp + g1p + h --> adpglc + ppi	U	0	Infinity
GLNS	[c] : atp + glu-L + nh4 --> adp + gln-L + h + pi	U	0	Infinity
GLNSP3	[c] : atp + nh3 + uaagmda --> adp + pi + uaagtmda	U	0	Infinity
GLNTRS	[c] : atp + gln-L + trnagln --> amp + glntrna + h + ppi	U	0	Infinity
GLU5K	[c] : atp + glu-L --> adp + glu5p	U	0	Infinity
GLUDx	[c] : glu-L + h2o + nad <==> akg + h + nadh + nh4	U	-Infinity	0
GLUDy	[c] : glu-L + h2o + nadp <==> akg + h + nadph + nh4	U	-Infinity	0
GLUPRT	[c] : gln-L + h2o + prpp --> glu-L + ppi + pram	U	0	Infinity
GLUR	[c] : glu-D <==> glu-L	U	-Infinity	Infinity
GLUSy	[c] : akg + gln-L + h + nadph --> (2) glu-L + nadp	U	0	Infinity
GLUSz	[c] : akg + fdxr-4:2 + gln-L + (2) h <==> fdxo-4:2 + (2) glu-L	U	-Infinity	Infinity

GLUTRR	[c] : glutrna + (2) h + nadph --> glu1sa + nadp + trnaglu	U	0	Infinity
GLUTRS	[c] : atp + glu-L + trnaglu --> amp + glutrna + h + ppi	U	0	Infinity
GLYD	[c] : h + hpyr + nadh <==> glyc-R + nad	U	-Infinity	Infinity
GLYK	[c] : atp + glyc --> adp + glyc3p + h	U	0	Infinity
GMPS2	[c] : atp + gln-L + h2o + xmp --> amp + glu-L + gmp + (2) h + ppi	U	0	Infinity
GOFUCR	[c] : gdpofuc + h + nadph --> gdpfuc + nadp	U	0	Infinity
GRTT	[c] : grdp + ipdp --> frdp + ppi	U	0	Infinity
GSADH	[c] : glu5sa + h2o + nad --> glu-L + (2) h + nadh	U	0	Infinity
GSHPO	[c] : (2) gthrd + h2o2 --> gthox + (2) h2o	U	0	Infinity
GTPCII	[c] : gtp + (3) h2o --> 25dhpp + for + (2) h + ppi	U	0	Infinity
GTPDPK	[c] : atp + gtp --> amp + gdptp + h	U	0	Infinity
GUAPRT	[c] : gua + prpp --> gmp + ppi	U	0	Infinity
HBUHL1	[c] : 3hbacp --> 2beacp + h2o	U	0	Infinity
HBUR1	[c] : aaacp + h + nadph --> 3hbacp + nadp	U	0	Infinity
HBZOPT	[c] : 4hbz + octdp --> 3ophb + ppi	U	0	Infinity
HCO3E	[c] : co2 + h2o <==> h + hco3	U	-Infinity	Infinity
HDACPHL	[c] : h2o + hdeacp --> acp + h + hdca	U	0	Infinity
HDDHL5	[c] : 3hddacp --> 2tddacp + h2o	U	0	Infinity
HDDR5	[c] : 3oxddacp + h + nadph --> 3hddacp + nadp	U	0	Infinity
HDEHL4	[c] : 3hdeacp --> 2tdeacp + h2o	U	0	Infinity
HDER4	[c] : 3oxdeacp + h + nadph --> 3hdeacp + nadp	U	0	Infinity
HDH	[c] : h2 + nad --> h + nadh	U	0	Infinity
HDH2	(2) h[c] + h2[c] + mqn7[c] --> (2) h[e] + mql7[c]	U	0	Infinity
HDMAT7	[c] : 2thdeacp + h + nadh --> hdeacp + nad	U	0	Infinity
HEMAT2	[c] : 2theacp + h + nadh --> hexacp + nad	U	0	Infinity
HEPTT	[c] : hepdp + ipdp --> octdp + ppi	U	0	Infinity
HEX1	[c] : atp + glc-D --> adp + g6p + h	U	0	Infinity
HEXTT	[c] : hexdp + ipdp --> hepdp + ppi	U	0	Infinity
HGBAMCOC	[c] : atp + cobalt2 + h2o + hgbam + nadh --> adp + co2dam + h + nad + pi	U	0	Infinity
HGBAMS	[c] : (2) atp + (2) gln-L + h2o + hgbyr --> (2) adp + (2) glu-L + h + hgbam + ppi	U	0	Infinity
HGR	[c] : hg2 + nadph <==> h + hg0 + nadp	U	-Infinity	Infinity

HHDHL7	[c] : 3hpaacp --> 2thdeacp + h2o	U	0	Infinity
HHDR7	[c] : 3oxhdacp + h + nadph --> 3hpaacp + nadp	U	0	Infinity
HHYHL2	[c] : 3hhacp --> 2theacp + h2o	U	0	Infinity
HHYR2	[c] : 3oxhacp + h + nadph --> 3hhacp + nadp	U	0	Infinity
HIBD	[c] : 3hmp + nad --> 2mop + h + nadh	U	0	Infinity
HISTD	[c] : h2o + histd + (2) nad --> (3) h + his-L + (2) nadh	U	0	Infinity
HISTP	[c] : h2o + hisp --> histd + pi	U	0	Infinity
HMBS	[c] : h2o + (4) ppbng --> hmbil + (4) nh4	U	0	Infinity
HMPK1	[c] : 4ahmmp + atp --> 4ampm + adp + h	U	0	Infinity
HMPK2	[c] : 4ahmmp + ctp --> 4ampm + cdp + h	U	0	Infinity
HMPK3	[c] : 4ahmmp + utp --> 4ampm + h + udp	U	0	Infinity
HMPK4	[c] : 4ahmmp + gtp --> 4ampm + gdp + h	U	0	Infinity
HOCHL3	[c] : 3hocacp --> 2toceacp + h2o	U	0	Infinity
HOCR3	[c] : 3oxocacp + h + nadph --> 3hocacp + nadp	U	0	Infinity
HODHL8	[c] : 3hocdacp --> 2tocdacp + h2o	U	0	Infinity
HODR8	[c] : 3oxocdacp + h + nadph --> 3hocdacp + nadp	U	0	Infinity
HP5CD	[c] : 1p3h5c + (2) h2o + nad --> 4hglu + h + nadh	U	0	Infinity
HPOD	[c] : Lhpro + fad --> 1p3h5c + fadh2 + h	U	0	Infinity
HPPK	[c] : 2ahhmp + atp --> 2ahhmd + amp + h	U	0	Infinity
HSAT	[c] : accoa + hom-L <==> achms + coa	U	-Infinity	Infinity
HSDy	[c] : hom-L + nadp <==> aspsa + h + nadph	U	-Infinity	Infinity
HSK	[c] : atp + hom-L --> adp + h + phom	U	0	Infinity
HSTPT	[c] : glu-L + imacp --> akg + h + hisp	U	0	Infinity
HTDHL6	[c] : 3htdacp --> 2ttdeacp + h2o	U	0	Infinity
HTDR6	[c] : 3oxtdacp + h + nadph --> 3htdacp + nadp	U	0	Infinity
HXPRT	[c] : hxan + prpp --> imp + ppi	U	0	Infinity
ICDHy	[c] : icit + nadp <==> akg + co2 + nadph	U	-Infinity	Infinity
ICHORSi	[c] : chor --> ichor	U	0	Infinity
ICHORT	[c] : h2o + ichor --> 23ddhb + pyr	U	0	Infinity
IG3PS	[c] : gln-L + prlp --> aicar + eig3p + glu-L + (2) h	U	0	Infinity
IGPDH	[c] : eig3p + h --> h2o + imacp	U	0	Infinity

IGPS	[c] : 2cpr5p + h --> 3ig3p + co2 + h2o	U	0	Infinity
ILETA	[c] : akg + ile-L <==> 3mop + glu-L	U	-Infinity	Infinity
IMPC	[c] : h2o + imp <==> fprica	U	-Infinity	Infinity
IMPD	[c] : h2o + imp + nad --> h + nadh + xmp	U	0	Infinity
IPDPS	[c] : h + h2mb4p + nadh --> h2o + ipdp + nad	U	0	Infinity
IPMD	[c] : 3c2hmp + nad --> 3c4mop + h + nadh	U	0	Infinity
IPPMIa	[c] : 3c2hmp <==> 2ippm + h2o	U	-Infinity	Infinity
IPPMIb	[c] : 2ippm + h2o <==> 3c3hmp	U	-Infinity	Infinity
IPPS	[c] : 3mob + accoa + h2o --> 3c3hmp + coa + h	U	0	Infinity
KARA1	[c] : 23dhmb + nadp <==> alac-S + h + nadph	U	-Infinity	Infinity
KARA2	[c] : 2ahbut + h + nadph <==> 23dhmp + nadp	U	-Infinity	Infinity
KAS1	[c] : (14) h + ibcoa + (5) malcoa + (10) nadph --> (5) co2 + (6) coa + fa1 + (4) h2o + (10) nadp	U	0	Infinity
KAS17	[c] : accoa + (22) h + (8) malcoa + (15) nadph --> (8) co2 + (9) coa + (7) h2o + (15) nadp + ocdcea	U	0	Infinity
KAS3	[c] : (14) h + ivcoa + (5) malcoa + (10) nadph --> (5) co2 + (6) coa + fa3 + (4) h2o + (10) nadp	U	0	Infinity
KAS4	[c] : 2mbcoa + (14) h + (5) malcoa + (10) nadph --> (5) co2 + (6) coa + fa4 + (4) h2o + (10) nadp	U	0	Infinity
KAS7	[c] : accoa + (19) h + (7) malcoa + (13) nadph --> (7) co2 + (8) coa + (6) h2o + hdcea + (13) nadp	U	0	Infinity
KAS9	[c] : (16) h + ivcoa + (6) malcoa + (11) nadph --> (6) co2 + (7) coa + fa9 + (5) h2o + (11) nadp	U	0	Infinity
KDOPS	[c] : ara5p + h2o + pep --> kdo8p + pi	U	0	Infinity
Kt6	h[e] + k[e] <==> h[c] + k[c]	U	0	Infinity
Ktabc	atp[c] + h2o[c] + k[e] --> adp[c] + h[e] + k[c] + pi[c]	U	0	Infinity
LEUD	[c] : h2o + leu-D + nad --> 4mop + h + nadh + nh4	U	0	Infinity
LEUTA	[c] : akg + leu-L <==> 4mop + glu-L	U	-Infinity	Infinity
LGTHL	[c] : gthrd + mthgxl --> lgt-S	U	0	Infinity
LPADSS	[c] : lipidX + u23ga --> h + lipidAds + udp	U	0	Infinity
LYSt3	h[e] + lys-L[c] --> h[c] + lys-L[e]	U	0	Infinity
MACPMT	[c] : acp + malcoa --> coa + malacp	U	0	Infinity

MAN1PT1	[c] : gtp + h + man1p --> gdpman + ppi	U	0	Infinity
MAN6PI	[c] : man6p <==> f6p	U	-Infinity	Infinity
MCMAT2	[c] : butacp + h + malacp --> 3oxhacp + acp + co2	U	0	Infinity
MCMAT3	[c] : h + hexacp + malacp --> 3oxocacp + acp + co2	U	0	Infinity
MCMAT4	[c] : h + malacp + octacp --> 3oxdeacp + acp + co2	U	0	Infinity
MCMAT5	[c] : decacp + h + malacp --> 3oxddacp + acp + co2	U	0	Infinity
MCMAT6	[c] : ddeacp + h + malacp --> 3oxtdacp + acp + co2	U	0	Infinity
MCMAT7	[c] : h + malacp + tdeacp --> 3oxhdacp + acp + co2	U	0	Infinity
MCMAT8	[c] : h + hdeacp + malacp --> 3oxocdacp + acp + co2	U	0	Infinity
MDH	[c] : mal-L + nad <==> h + nadh + oaa	U	-Infinity	Infinity
ME1x	[c] : mal-L + nad --> co2 + nadh + pyr	U	0	Infinity
ME2	[c] : mal-L + nadp --> co2 + nadph + pyr	U	0	Infinity
MECDPDH	[c] : 2mecdp + nadh --> h2mb4p + h2o + nad	U	0	Infinity
MECDPS	[c] : 2p4c2me --> 2mecdp + cmp	U	0	Infinity
MEPCT	[c] : 2me4p + ctp + h --> 4c2me + ppi	U	0	Infinity
METACH	[c] : achms + h2s <==> ac + h + hcys-L	U	-Infinity	Infinity
METAT	[c] : atp + h2o + met-L --> amet + pi + ppi	U	0	Infinity
METS	[c] : 5mthf + hcys-L --> h + met-L + thf	U	0	Infinity
MMCD	[c] : h + mmcoa-S --> co2 + ppcoa	U	0	Infinity
MMM	[c] : mmcoa-R --> succoa	U	0	Infinity
MOHMT	[c] : 3mob + h2o + mlthf --> 2dhp + thf	U	0	Infinity
MTAN	[c] : 5mta + h2o --> 5mtr + ade	U	0	Infinity
MTAP	[c] : 5mta + pi --> 5mdr1p + ade	U	0	Infinity
MTHFC	[c] : h2o + methf <==> 10fthf + h	U	-Infinity	Infinity
MTHFD	[c] : mlthf + nadp <==> methf + nadph	U	-Infinity	Infinity
MTHFR	[c] : fadh2 + h + mlthf --> 5mthf + fad	U	0	Infinity
MTHFR1	[c] : (2) h + mlthf + nadph --> 5mthf + nadp	U	0	Infinity
NACCYT	[c] : acnam + ctp --> cmpacna + ppi	U	0	Infinity
NADH5	(3) h[c] + mqn7[c] + nadh[c] --> (2) h[e] + mql7[c] + nad[c]	U	0	Infinity
NADK	[c] : atp + nad --> adp + h + nadp	U	0	Infinity
NADPH5	(3) h[c] + mqn7[c] + nadph[c] --> (2) h[e] + mql7[c] + nadp[c]	U	0	Infinity

NADS1	[c] : atp + dnad + nh4 --> amp + h + nad + ppi	U	0	Infinity
NAt7	h[e] + na1[c] <==> h[c] + na1[e]	U	0	Infinity
NDPK1	[c] : atp + gdp <==> adp + gtp	U	-Infinity	Infinity
NDPK2	[c] : atp + udp <==> adp + utp	U	-Infinity	Infinity
NDPK3	[c] : atp + cdp <==> adp + ctp	U	-Infinity	Infinity
NDPK4	[c] : atp + dtdp <==> adp + dttp	U	-Infinity	Infinity
NDPK5	[c] : atp + dgdp <==> adp + dgtp	U	-Infinity	Infinity
NDPK6	[c] : atp + dudp <==> adp + dutp	U	-Infinity	Infinity
NDPK7	[c] : atp + dcdp <==> adp + dctp	U	-Infinity	Infinity
NDPK8	[c] : atp + dadp <==> adp + datp	U	-Infinity	Infinity
NH4DIS	[c] : nh4 <==> h + nh3	U	-Infinity	Infinity
NH4OHD	[c] : h + nh4oh <==> h2o + nh4	U	-Infinity	Infinity
NH4t3	k[c] + nh4[e] --> k[e] + nh4[c]	U	0	Infinity
NIT2	[c] : (8) atp + (4) fdxr-4:2 + (2) h + (8) h2o + n2 --> (8) adp + (4) fdxo-4:2 + h2 + (2) nh4 + (8) pi	U	0	Infinity
NNAM	[c] : h2o + ncam --> nac + nh4	U	0	Infinity
NNAT	[c] : atp + h + nicrnt --> dnad + ppi	U	0	Infinity
NNDMBRT	[c] : dmbzid + nicrnt --> 5prdmbz + h + nac	U	0	Infinity
NNDMBRT2	[c] : ribflv --> dmbzid + unknown1	U	0	Infinity
NNDPR	[c] : (2) h + prpp + quln --> co2 + nicrnt + ppi	U	0	Infinity
NPHS	[c] : sbzcoa --> coa + dhna	U	0	Infinity
NTRIRfc	[c] : (6) focytc + (8) h + no2 --> (6) ficytc + (2) h2o + nh4	U	0	Infinity
NTRIRy	[c] : (4) h + (3) nadph + no2 --> h2o + (3) nadp + nh4oh	U	0	Infinity
OCBT	[c] : cbp + orn-L <==> citr-L + h + pi	U	-Infinity	Infinity
OCDMAT8	[c] : 2tocdacp + h + nadh --> nad + ocdacp	U	0	Infinity
OCMAT3	[c] : 2toceacp + h + nadh --> nad + octacp	U	0	Infinity
OCTDPS	[c] : frdp + (5) ipdp --> octdp + (5) ppi	U	0	Infinity
OCTT	[c] : ipdp + octdp --> nondp + ppi	U	0	Infinity
ODACPHL	[c] : h2o + ocdacp --> acp + h + ocdca	U	0	Infinity
OIVD1	[c] : 4mop + coa + nad <==> co2 + ivcoa + nadh	U	-Infinity	Infinity
OIVD2	[c] : 3mob + coa + nad --> co2 + ibcoa + nadh	U	0	Infinity

OIVD3	[c] : 3mop + coa + nad --> 2mbcoa + co2 + nadh	U	0	Infinity
OMCDC	[c] : 3c4mop + h --> 4mop + co2	U	0	Infinity
OMPDC	[c] : h + orot5p --> co2 + ump	U	0	Infinity
OOR	[c] : akg + coa + fdxo-4:2 --> co2 + fdxr-4:2 + h + succoa	U	0	Infinity
OPHBDC	[c] : 3ophb + h --> 2oph + co2	U	0	Infinity
ORNTAC	[c] : acorn + glu-L <==> acglu + orn-L	U	-Infinity	Infinity
ORPT	[c] : orot5p + ppi <==> orot + prpp	U	-Infinity	Infinity
OXGDC2	[c] : akg + (2) h + thmpp --> co2 + ssaltpp	U	0	Infinity
P5CD	[c] : 1pyr5c + (2) h2o + nad --> glu-L + h + nadh	U	0	Infinity
P5CR	[c] : 1pyr5c + (2) h + nadph --> nadp + pro-L	U	0	Infinity
PANTS	[c] : ala-B + atp + pant-R --> amp + h + pnto-R + ppi	U	0	Infinity
PAPPT3	[c] : udcpp + ugmda --> uagmda + ump	U	0	Infinity
PAPSR2	[c] : (2) h + pap + so3 + trdox --> paps + trdrd	U	-Infinity	Infinity
PC	[c] : atp + hco3 + pyr --> adp + h + oaa + pi	U	0	Infinity
PC11M	[c] : amet + pre4 --> ahcys + h + pre5	U	0	Infinity
PC17M	[c] : amet + pre3b --> ahcys + (3) h + pre4	U	0	Infinity
PC20M	[c] : amet + shcl --> ahcys + h + pre3a	U	0	Infinity
PC3BS	[c] : h + (0.5) o2 + pre3a --> pre3b	U	0	Infinity
PC6AR	[c] : h + nadph + pre6a --> nadp + pre6b	U	0	Infinity
PC6YM	[c] : (2) amet + pre6b --> (2) ahcys + co2 + (2) h + pre8	U	0	Infinity
PC8XM	[c] : h + pre8 --> hgbyr	U	0	Infinity
PDH	[c] : coa + nad + pyr --> accoa + co2 + nadh	U	0	Infinity
PFK	[c] : atp + f6p --> adp + fdp + h	U	0	Infinity
PFL	[c] : coa + pyr <==> accoa + for	U	-Infinity	Infinity
PGAMT	[c] : gam1p <==> gam6p	U	-Infinity	Infinity
PGCD	[c] : 3pg + nad --> 3php + h + nadh	U	0	Infinity
PGI	[c] : g6p <==> f6p	U	-Infinity	Infinity
PGK	[c] : 13dpg + adp <==> 3pg + atp	U	-Infinity	Infinity
PGLUSYN	[c] : atp + glu-D --> adp + h + pi + polglu	U	0	Infinity
PGLYCP	[c] : 2pglyc + h2o --> glyclt + pi	U	0	Infinity
PGM	[c] : 3pg <==> 2pg	U	-Infinity	Infinity

PGMT	[c] : g1p <==> g6p	U	-Infinity	Infinity
PGPPH	[c] : h2o + pglyp --> pgly + pi	U	0	Infinity
PHCYT	[c] : 12dag3p + ctp + h --> cdpdag + ppi	U	0	Infinity
PHETA1	[c] : akg + phe-L <==> glu-L + phpyr	U	-Infinity	Infinity
PIabc	atp[c] + h2o[c] + pi[e] --> adp[c] + h[c] + (2) pi[c]	U	0	Infinity
PIt6	h[e] + pi[e] <==> h[c] + pi[c]	U	-Infinity	Infinity
PIt7	(3) na1[e] + pi[e] <==> (3) na1[c] + pi[c]	U	-Infinity	Infinity
PMANM	[c] : man1p <==> man6p	U	-Infinity	Infinity
PMDPHT	[c] : 5aprbu + h2o --> 4r5au + pi	U	0	Infinity
PMPK	[c] : 4ampm + atp --> 2mahmp + adp	U	0	Infinity
PNTEH	[c] : h2o + ptth --> cysam + pnto-R	U	0	Infinity
PNTK	[c] : atp + pnto-R --> 4ppan + adp + h	U	0	Infinity
POR	[c] : coa + fdxo-4:2 + pyr <==> accoa + co2 + fdxr-4:2 + h	U	-Infinity	Infinity
PPA	[c] : h2o + ppi --> h + (2) pi	U	0	Infinity
PPA_1	h2o[c] + ppi[c] --> h[e] + (2) pi[c]	U	0	Infinity
PPBNGS	[c] : (2) 5aop --> h + (2) h2o + ppbng	U	0	Infinity
PPCDC	[c] : 4ppcys + h --> co2 + pan4p	U	0	Infinity
PPCK	[c] : atp + oaa --> adp + co2 + pep	U	0	Infinity
PPDK	[c] : atp + pi + pyr --> amp + h + pep + ppi	U	0	Infinity
PPIK	[c] : atp + ppi --> adp + pppi	U	0	Infinity
PPNCL	[c] : 4ppan + ctp + cys-L --> 4ppcys + cdp + h + pi	U	0	Infinity
PPND	[c] : nad + pphn --> 34hpp + co2 + nadh	U	0	Infinity
PPNDH	[c] : h + pphn --> co2 + h2o + phpyr	U	0	Infinity
PPPGO	[c] : (1.5) o2 + pppg9 --> (3) h2o + ppp9	U	0	Infinity
PPS	[c] : atp + h2o + pyr --> amp + (2) h + pep + pi	U	0	Infinity
PPTGS2	[c] : uaagtmdga --> (2) h + pptg1 + udcpdp	U	0	Infinity
PPTT	[c] : ipdp + pendp --> hexdp + ppi	U	0	Infinity
PRAGS	[c] : atp + gly + pram --> adp + gar + h + pi	U	0	Infinity
PRAI	[c] : pran <==> 2cpr5p	U	-Infinity	Infinity
PRAIS	[c] : atp + fpram --> adp + air + h + pi	U	0	Infinity
PRAMPC	[c] : h + h2o + prbamp --> prfp	U	0	Infinity

PRASCS	[c] : 5aizc + asp-L + atp <==> 25aics + adp + h + pi	U	-Infinity	Infinity
PRATPP	[c] : h2o + prbatp --> h + ppi + prbamp	U	0	Infinity
PRE6AS	[c] : amet + h2o + pre5 --> ac + ahcys + h + pre6a	U	0	Infinity
PRFGS	[c] : atp + fgam + gln-L + h2o --> adp + fpram + glu-L + (2) h + pi	U	0	Infinity
PRMICI	[c] : prfp <==> prlp	U	-Infinity	Infinity
PRPPS	[c] : atp + r5p <==> amp + h + prpp	U	-Infinity	Infinity
PSCVT	[c] : pep + skm5p <==> 3psme + pi	U	-Infinity	Infinity
PSERT	[c] : 3php + glu-L --> akg + pser-L	U	0	Infinity
PSP_L	[c] : h2o + pser-L --> pi + ser-L	U	0	Infinity
PTAr	[c] : accoa + pi <==> actp + coa	U	-Infinity	Infinity
PTHPS	[c] : ahdt --> 6pthp + pppi	U	0	Infinity
PTPAT	[c] : atp + h + pan4p <==> dpcoa + ppi	U	-Infinity	Infinity
PYK	[c] : adp + h + pep --> atp + pyr	U	0	Infinity
PYRZAM	[c] : h2o + malm --> male + nh4	U	0	Infinity
QULNS	[c] : dhap + iasp --> (2) h2o + pi + quln	U	0	Infinity
RBFK	[c] : atp + ribflv --> adp + fmn + h	U	0	Infinity
RBFSa	[c] : 4r5au + db4p --> dmlz + (2) h2o + pi	U	0	Infinity
RBFSb	[c] : (2) dmlz --> 4r5au + ribflv	U	0	Infinity
RBK	[c] : atp + rib-D --> adp + h + r5p	U	0	Infinity
RBZP	[c] : 5prdmbz + h2o --> pi + rdmbzi	U	0	Infinity
RNDR1	[c] : adp + trdrd --> dadp + h2o + trdox	U	0	Infinity
RNDR2	[c] : gdp + trdrd --> dgdp + h2o + trdox	U	0	Infinity
RNDR3	[c] : cdp + trdrd --> dcdp + h2o + trdox	U	0	Infinity
RNDR4	[c] : trdrd + udp --> dudp + h2o + trdox	U	0	Infinity
RPE	[c] : ru5p-D <==> xu5p-D	U	-Infinity	Infinity
RPI	[c] : r5p <==> ru5p-D	U	-Infinity	Infinity
SADT2	[c] : atp + gtp + h2o + so4 --> aps + gdp + pi + ppi	U	0	Infinity
SBDH	[c] : nadp + sbt6p --> h + nadph + srb1p	U	0	Infinity
SDPDS	[c] : h2o + sl26da --> 26dap-LL + succ	U	0	Infinity
SDPTA	[c] : akg + sl26da <==> glu-L + sl2a6o	U	-Infinity	Infinity
SERAT	[c] : accoa + ser-L <==> acser + coa	U	-Infinity	Infinity

SERD_L	[c] : ser-L --> nh4 + pyr	U	0	Infinity
SHCHCS2	[c] : ichor + ssaltpp --> 2shchc + h + pyr + thmpp	U	0	Infinity
SHCHD	[c] : nadp + shcl --> (2) h + nadph + srch	U	0	Infinity
SHCHF	[c] : fe2 + srch --> (2) h + sheme	U	0	Infinity
SHK3D	[c] : 3dhsk + h + nadph <==> nadp + skm	U	-Infinity	Infinity
SHKK	[c] : atp + skm --> adp + h + skm5p	U	0	Infinity
SO4t2	h[e] + so4[e] --> h[c] + so4[c]	U	0	Infinity
SOD	[c] : (2) h + (2) o2- --> h2o2 + o2	U	0	Infinity
SPMS	[c] : ametam + ptrc --> 5mta + h + spmd	U	0	Infinity
SUCBZL	[c] : atp + coa + sucbz --> amp + ppi + sbzcoa	U	0	Infinity
SUCBZS	[c] : 2shchc --> h2o + sucbz	U	0	Infinity
SUCFUMtdc	fum[e] + succ[c] <==> fum[c] + succ[e]	U	-Infinity	Infinity
SUCOAS	[c] : atp + coa + succ <==> adp + pi + succoa	U	0	Infinity
SULR	[c] : (3) h2o + h2s + (3) nadp <==> (5) h + (3) nadph + so3	U	-Infinity	Infinity
SULabc	atp[c] + h2o[c] + so4[e] --> adp[c] + h[c] + pi[c] + so4[c]	U	0	Infinity
TADSK	[c] : atp + h2o + lipidA --> adp + h + lipid4 + pi	U	0	Infinity
TAL	[c] : g3p + s7p <==> e4p + f6p	U	-Infinity	Infinity
TDACPHL	[c] : h2o + tdeacp --> acp + h + myrt	U	0	Infinity
TDMAT6	[c] : 2ttdeacp + h + nadh --> nad + tdeacp	U	0	Infinity
TDPDRR	[c] : dtdp6dm + nadp <==> dtdpddm + h + nadph	U	-Infinity	Infinity
TDPGDH	[c] : dtdpglc --> dtdpddg + h2o	U	0	Infinity
THDPS	[c] : h2o + succoa + thdp --> coa + sl2a6o	U	0	Infinity
THPDH	[c] : nad + phthr --> amopbut-L + h + nadh	U	0	Infinity
THRA	[c] : thr-L <==> acald + gly	U	-Infinity	Infinity
THRD_L	[c] : thr-L --> 2obut + nh4	U	0	Infinity
THRLAD	[c] : thr-LA --> acald + gly	U	0	Infinity
THRS	[c] : h2o + phom --> pi + thr-L	U	0	Infinity
TKT1	[c] : r5p + xu5p-D <==> g3p + s7p	U	-Infinity	Infinity
TKT2	[c] : e4p + xu5p-D <==> f6p + g3p	U	-Infinity	Infinity
TMDK1	[c] : atp + thymd --> adp + dtmp + h	U	0	Infinity
TMDS	[c] : dump + mlthf --> dhf + dtmp	U	0	Infinity

TMPK	[c] : atp + thmmp --> adp + thmpp	U	0	Infinity
TMPPP	[c] : 2mahmp + 4mpetz + h --> ppi + thmmp	U	0	Infinity
TPI	[c] : dhap <==> g3p	U	-Infinity	Infinity
TRDR	[c] : h + nadph + trdox --> nadp + trdrd	U	0	Infinity
TRE6PP	[c] : h2o + tre6p --> pi + tre	U	0	Infinity
TRPS1	[c] : 3ig3p + ser-L --> g3p + h2o + trp-L	U	0	Infinity
TYRTA	[c] : akg + tyr-L <==> 34hpp + glu-L	U	-Infinity	Infinity
UAAGDS	[c] : 26dap-M + atp + uamag --> adp + h + pi + ugmd	U	0	Infinity
UACAT	[c] : 3htdacp + uacgam --> acp + u3aga	U	0	Infinity
UAG2E	[c] : uacgam <==> uacmam	U	-Infinity	Infinity
UAG2EMA	[c] : h2o + uacgam <==> acmana + h + udp	U	-Infinity	Infinity
UAGCVT	[c] : pep + uacgam --> pi + uaccg	U	0	Infinity
UAGDP	[c] : acgam1p + h + utp --> ppi + uacgam	U	0	Infinity
UAGPT3	[c] : uacgam + uagmda --> h + uaagmda + udp	U	0	Infinity
UAGT3	[c] : (5) gly + uaagtmda --> (5) h2o + uaagtmdga	U	0	Infinity
UAMAGS	[c] : atp + glu-D + uama --> adp + h + pi + uamag	U	0	Infinity
UAMAS	[c] : ala-L + atp + uamr --> adp + h + pi + uama	U	0	Infinity
UAPGR	[c] : h + nadph + uaccg --> nadp + uamr	U	0	Infinity
UDCPDP	[c] : h2o + udcpdp --> h + pi + udcpp	U	0	Infinity
UDCPK	[c] : atp + udcp --> adp + h + udcpp	U	0	Infinity
UDPDPS	[c] : decdp + ipdp --> ppi + udcpdp	U	0	Infinity
UDPG4E	[c] : udpg <==> udpgal	U	-Infinity	Infinity
UDPGD	[c] : h2o + (2) nad + udpg <==> (3) h + (2) nadh + udpglcur	U	-Infinity	Infinity
UGMDDS	[c] : alaala + atp + ugmd --> adp + h + pi + ugmda	U	0	Infinity
UGSAT	[c] : acp + h + u23ga <==> 3htdacp + u3hga	U	-Infinity	Infinity
UHGADA	[c] : h2o + u3aga --> ac + u3hga	U	0	Infinity
UPP3MT	[c] : (2) amet + uppg3 --> (2) ahcys + h + shcl	U	0	Infinity
UPP3S	[c] : hmbil --> h2o + uppg3	U	0	Infinity
UPPDC1	[c] : (4) h + uppg3 --> (4) co2 + cpppg3	U	0	Infinity
UPPRT	[c] : prpp + ura --> ppi + ump	U	0	Infinity
URIDK1	[c] : atp + ump --> adp + udp	U	0	Infinity

URIDK2	[c] : atp + dump --> adp + dudp	U	0	Infinity
VALTA	[c] : akg + val-L <==> 3mob + glu-L	U	-Infinity	Infinity
agg_GS13m	[c] : (0.022284123) 26dap-M + (0.0177014) 3pg + (0.021845986) akg + (0.022284123) ala-D + (0.372353) ala-L + (0.20157662) arg-L + (0.164274185) asn-L + (0.164274) asp-L + (18.218804) atp + (0.000940527) ca2 + (0.040129178) ctp + (0.062409843) cys-L + (0.020714) datp + (0.020714656) dctp + (0.020714656) dgtp + (0.020714656) dttp + (0.001307) fa1 + (0.062391063) fa3 + (0.002733323) fa4 + (0.011170971) fa9 + (0.191964286) g3p + (0.026552099) g6p + (0.17933863) gln-L + (0.022284123) glu-D + (0.17933863) glu-L + (0.417500331) gly + (0.925925926) glycogen + (0.064652564) gtp + (13.07392627) h2o + (0.225997835) hdca + (0.276897481) hdcea + (0.064561907) his-L + (0.197989848) ile-L + (0.221964448) k + (0.307027735) leu-L + (0.233857574) lys-L + (0.10473376) met-L + (0.031977929) mg2 + (0.021391222) myrt + (0.0177014) nad + (0.056687258) nadph + (0.061393371) nh4 + (0.003862304) ocdca + (0.023114403) ocdcea + (0.0177014) pep + (0.126254396) phe-L + (0.28381802) ppi + (0.150644449) pro-L + (0.0177014) r5p + (0.471859373) ser-L + (0.17288244) thr-L + (0.038737144) trp-L + (0.093973442) tyr-L + (0.034085056) uacgam + (0.022284123) uamr + (0.011800933) udpg + (0.043314033) utp + (0.288376518) val-L --> (18.166254) adp + (18.20524) h + (0.0177014) nadh + (0.056687) nadp + (18.214415) pi	U	-Infinity	Infinity
EX_h(e)	[e] : h <==>	U	-Infinity	Infinity
EX_fe2(e)	[e] : fe2 <==>	U	-Infinity	Infinity
EX_co2(e)	[e] : co2 <==>	U	-Infinity	Infinity
EX_so4(e)	[e] : so4 <==>	U	-Infinity	Infinity
EX_pi(e)	[e] : pi <==>	U	-Infinity	Infinity
EX_nh4(e)	[e] : nh4 <==>	U	-Infinity	Infinity
EX_mg2(e)	[e] : mg2 <==>	U	-Infinity	Infinity
EX_k(e)	[e] : k <==>	U	-Infinity	Infinity
EX_h2o(e)	[e] : h2o <==>	U	-Infinity	Infinity
EX_fe3(e)	[e] : fe3 <==>	U	-Infinity	Infinity
EX_ac(e)	[e] : ac <==>	U	-Infinity	Infinity
EX_zn2(e)	[e] : zn2 <==>	U	-Infinity	Infinity
EX_val-L(e)	[e] : val-L <==>	U	0	Infinity

EX_ura(e)	[e] : ura <==>	U	0	Infinity
EX_succ(e)	[e] : succ <==>	U	0	Infinity
EX_ss(e)	[e] : ss <==>	U	0	Infinity
EX_s(e)	[e] : s <==>	U	0	Infinity
EX_pro-L(e)	[e] : pro-L <==>	U	0	Infinity
EX_oxa(e)	[e] : oxa <==>	U	0	Infinity
EX_ni2(e)	[e] : ni2 <==>	U	-Infinity	Infinity
EX_na1(e)	[e] : na1 <==>	U	-Infinity	Infinity
EX_n2(e)	[e] : n2 <==>	U	-Infinity	Infinity
EX_mobd(e)	[e] : mobd <==>	U	-Infinity	Infinity
EX_mn2(e)	[e] : mn2 <==>	U	-Infinity	Infinity
EX_mal-L(e)	[e] : mal-L <==>	U	0	Infinity
EX_lys-L(e)	[e] : lys-L <==>	U	0	Infinity
EX_leu-L(e)	[e] : leu-L <==>	U	0	Infinity
EX_lac-L(e)	[e] : lac-L <==>	U	0	Infinity
EX_ile-L(e)	[e] : ile-L <==>	U	0	Infinity
EX_h2s(e)	[e] : h2s <==>	U	0	Infinity
EX_h2(e)	[e] : h2 <==>	U	0	Infinity
EX_gly(e)	[e] : gly <==>	U	0	Infinity
EX_gln-L(e)	[e] : gln-L <==>	U	0	Infinity
EX_fum(e)	[e] : fum <==>	U	0	Infinity
EX_for(e)	[e] : for <==>	U	0	Infinity
EX_cu2(e)	[e] : cu2 <==>	U	-Infinity	Infinity
EX_cobalt2(e)	[e] : cobalt2 <==>	U	-Infinity	Infinity
EX_cl(e)	[e] : cl <==>	U	-Infinity	Infinity
EX_cit(e)	[e] : cit <==>	U	0	Infinity
EX_cd2(e)	[e] : cd2 <==>	U	-Infinity	Infinity
EX_ca2(e)	[e] : ca2 <==>	U	-Infinity	Infinity

Table A.2: Metabolites utilized in the *Geobacter sulfurreducens* models presented in Chapters 4 and 5. Abbreviations are provided and "Type" refers to whether a metabolite is a balanced (i.e. "Cytosol") or an unbalanced, external metabolite ("Extracellular").

Abbreviation	Type	Full name
10fthf	Cytosol	10-Formyltetrahydrofolate
12dag3p	Cytosol	1,2-Diacyl-sn-glycerol 3-phosphate
12dgr	Cytosol	1,2-Diacylglycerol
13dpg	Cytosol	3-Phospho-D-glyceroyl phosphate
1ag3p	Cytosol	1-Acyl-sn-glycerol 3-phosphate
1ap2ol	Cytosol	1-Aminopropan-2-ol
1p3h5c	Cytosol	L-1-Pyrroline-3-hydroxy-5-carboxylate
1pyr5c	Cytosol	1-Pyrroline-5-carboxylate
23ddhb	Cytosol	2,3-Dihydro-2,3-dihydroxybenzoate
23dhdp	Cytosol	2,3-Dihydrodipicolinate
23dhmb	Cytosol	(R)-2,3-Dihydroxy-3-methylbutanoate
23dhmp	Cytosol	(R)-2,3-Dihydroxy-3-methylpentanoate
25aics	Cytosol	(S)-2-[5-Amino-1-(5-phospho-D-ribosyl)imidazole-4-carboxamido]succinate
25dhpp	Cytosol	2,5-Diamino-6-hydroxy-4-(5'-phosphoribosylamino)-pyrimidine
26dap-LL	Cytosol	LL-2,6-Diaminoheptanedioate
26dap-M	Cytosol	meso-2,6-Diaminoheptanedioate
2ahbut	Cytosol	(S)-2-Aceto-2-hydroxybutanoate
2ahhmd	Cytosol	2-Amino-4-hydroxy-6-hydroxymethyl-7,8-dihydropteridine diphosphate
2ahhmp	Cytosol	2-Amino-4-hydroxy-6-hydroxymethyl-7,8-dihydropteridine
2beacp	Cytosol	But-2-enoyl-[acyl-carrier protein]
2cpr5p	Cytosol	1-(2-Carboxyphenylamino)-1-deoxy-D-ribulose 5-phosphate
2dda7p	Cytosol	2-Dehydro-3-deoxy-D-arabino-heptonate 7-phosphate
2dhp	Cytosol	2-Dehydropantoate
2dmmq8	Cytosol	2-Demethylmenaquinone 8
2ippm	Cytosol	2-Isopropylmaleate
2mahmp	Cytosol	2-Methyl-4-amino-5-hydroxymethylpyrimidine diphosphate

2mbcoa	Cytosol	2-Methylbutanoyl-CoA
2me4p	Cytosol	2-C-methyl-D-erythritol 4-phosphate
2mecdp	Cytosol	2-C-methyl-D-erythritol 2,4-cyclodiphosphate
2mop	Cytosol	2-Methyl-3-oxopropanoate
2obut	Cytosol	2-Oxobutanoate
2oph	Cytosol	2-Octaprenylphenol
2p4c2me	Cytosol	2-phospho-4-(cytidine 5'-diphospho)-2-C-methyl-D-erythritol
2pg	Cytosol	D-Glycerate 2-phosphate
2pglyc	Cytosol	2-Phosphoglycolate
2shchc	Cytosol	2-Succinyl-6-hydroxy-2,4-cyclohexadiene-1-carboxylate
2tddacp	Cytosol	trans-Dodec-2-enoyl-[acyl-carrier protein]
2tdeacp	Cytosol	trans-Dec-2-enoyl-[acyl-carrier protein]
2thdeacp	Cytosol	trans-Hexadec-2-enoyl-[acyl-carrier protein]
2theacp	Cytosol	trans-Hex-2-enoyl-[acp]
2tocdacp	Cytosol	trans-Octadec-2-enoyl-[acyl-carrier-protein]
2toceacp	Cytosol	trans-Oct-2-enoyl-[acp]
2ttdeacp	Cytosol	trans-Tetradec-2-enoyl-[acyl-carrier protein]
34hpp	Cytosol	3-(4-Hydroxyphenyl)pyruvate
3c2hmp	Cytosol	3-Carboxy-2-hydroxy-4-methylpentanoate
3c3hmp	Cytosol	3-Carboxy-3-hydroxy-4-methylpentanoate
3c4mop	Cytosol	3-Carboxy-4-methyl-2-oxopentanoate
3dhq	Cytosol	3-Dehydroquinate
3dhsk	Cytosol	3-Dehydroshikimate
3hbacp	Cytosol	(3R)-3-Hydroxybutanoyl-[acyl-carrier protein]
3hddacp	Cytosol	(R)-3-Hydroxydodecanoyl-[acyl-carrier protein]
3hdeacp	Cytosol	(3R)-3-Hydroxydecanoyl-[acyl-carrier protein]
3hhacp	Cytosol	(R)-3-Hydroxyhexanoyl-[acp]
3hmp	Cytosol	3-Hydroxy-2-methylpropanoate
3hocacp	Cytosol	(R)-3-Hydroxyoctanoyl-[acyl-carrier protein]
3hocdacp	Cytosol	(3R)-3-Hydroxyoctadecanoyl-[acyl-carrier protein
3hpaacp	Cytosol	(3R)-3-Hydroxypalmitoyl-[acyl-carrier protein]

3htdacp	Cytosol	(3R)-3-Hydroxytetradecanoyl-[acyl-carrier protein]
3ig3p	Cytosol	C'-(3-Indolyl)-glycerol 3-phosphate
3mob	Cytosol	3-Methyl-2-oxobutanoate
3mop	Cytosol	(S)-3-Methyl-2-oxopentanoate
3ophb	Cytosol	3-Octaprenyl-4-hydroxybenzoate
3oxddacp	Cytosol	3-Oxododecanoyl-[acyl-carrier protein]
3oxdeacp	Cytosol	3-Oxodecanoyl-[acyl-carrier protein]
3oxhacp	Cytosol	3-Oxohexanoyl-[acyl-carrier protein]
3oxhdacp	Cytosol	3-Oxohexadecanoyl-[acp]
3oxocacp	Cytosol	3-Oxooctanoyl-[acyl-carrier protein]
3oxocdacp	Cytosol	3-Oxooctadecanoyl-[acp]
3oxtdacp	Cytosol	3-Oxotetradecanoyl-[acyl-carrier protein]
3pg	Cytosol	3-Phospho-D-glycerate
3php	Cytosol	3-Phosphohydroxypyruvate
3psme	Cytosol	5-O-(1-Carboxyvinyl)-3-phosphoshikimate
4abz	Cytosol	4-Aminobenzoate
4adcho	Cytosol	4-amino-4-deoxychorismate
4ahmmp	Cytosol	4-Amino-5-hydroxymethyl-2-methylpyrimidine
4ampm	Cytosol	4-Amino-2-methyl-5-phosphomethylpyrimidine
4c2me	Cytosol	4-(cytidine 5'-diphospho)-2-C-methyl-D-erythritol
4hbz	Cytosol	4-Hydroxybenzoate
4hglu	Cytosol	4-Hydroxy-L-glutamate
4mop	Cytosol	4-Methyl-2-oxopentanoate
4mpetz	Cytosol	4-Methyl-5-(2-phosphoethyl)-thiazole
4pasp	Cytosol	4-Phospho-L-aspartate
4ppan	Cytosol	D-4'-Phosphopantothenate
4ppcys	Cytosol	N-((R)-4-Phosphopantothenoyl)-L-cysteine
4r5au	Cytosol	4-(1-D-Ribitylamino)-5-aminouracil
5aizc	Cytosol	5-amino-1-(5-phospho-D-ribosyl)imidazole-4-carboxylate
5aop	Cytosol	5-Amino-4-oxopentanoate
5aprbu	Cytosol	5-Amino-6-(5'-phosphoribitylamino)uracil

5apru	Cytosol	5-Amino-6-(5'-phosphoribosylamino)uracil
5fothf	Cytosol	5-Formyltetrahydrofolate
5mdr1p	Cytosol	5-Methylthio-5-deoxy-D-ribose 1-phosphate
5mta	Cytosol	5-Methylthioadenosine
5mthf	Cytosol	5-Methyltetrahydrofolate
5mtr	Cytosol	5-Methylthio-D-ribose
5prdmbz	Cytosol	N1-(5-Phospho-alpha-D-ribosyl)-5,6-dimethylbenzimidazole
6pthp	Cytosol	6-Pyruvoyl-5,6,7,8-tetrahydropterin
8aonn	Cytosol	8-Amino-7-oxononanoate
CO	Cytosol	Carbon monoxide
Lhpro	Cytosol	L-Hydroxyproline
aaacp	Cytosol	Acetoacetyl-[acyl-carrier protein]
ac	Extracellular	Acetate
ac[e]	Cytosol	Acetate
acacp	Cytosol	Acetyl-[acyl-carrier protein]
acald	Cytosol	Acetaldehyde
acamoxm	Cytosol	N-Acetyl-L-2-amino-6-oxopimelate
accoa	Cytosol	Acetyl-CoA
acg5p	Cytosol	N-Acetyl-L-glutamyl 5-phosphate
acg5sa	Cytosol	N-Acetyl-L-glutamate 5-semialdehyde
acgam1p	Cytosol	N-Acetyl-D-glucosamine 1-phosphate
acglu	Cytosol	N-Acetyl-L-glutamate
achms	Cytosol	O-Acetyl-L-homoserine
acmam	Cytosol	N-Acetyl-D-muramoate
acmama	Cytosol	N-Acetyl-D-muramoyl-L-alanine
acmana	Cytosol	N-Acetyl-D-mannosamine
acnam	Cytosol	N-Acetylneuraminate
acoa	Cytosol	Acyl-CoA
acorn	Cytosol	N2-Acetyl-L-ornithine
acp	Cytosol	Acyl-carrier Protein
acser	Cytosol	O-Acetyl-L-serine

actp	Cytosol	Acetyl phosphate
adcoba	Cytosol	Adenosyl cobinamide
adcobap	Cytosol	Adenosyl cobinamide phosphate
adcobdam	Cytosol	Adenosyl cobyrinate diamide
adcobhex	Cytosol	adenosyl-cobyric acid
ade	Cytosol	Adenine
adgcoba	Cytosol	Adenosine-GDP-cobinamide
adn	Cytosol	Adenosine
adp	Cytosol	ADP
adpglc	Cytosol	ADPglucose
agm	Cytosol	Agmatine
ahcys	Cytosol	S-Adenosyl-L-homocysteine
ahdt	Cytosol	2-Amino-4-hydroxy-6-(erythro-1,2,3-trihydroxypropyl)dihydropteridine triphosphate
aicar	Cytosol	5-Amino-1-(5-Phospho-D-ribosyl)imidazole-4-carboxamide
air	Cytosol	5-amino-1-(5-phospho-D-ribosyl)imidazole
akg	Cytosol	2-Oxoglutarate
ala-B	Cytosol	beta-Alanine
ala-D	Cytosol	D-Alanine
ala-L	Cytosol	L-Alanine
alaala	Cytosol	D-Alanyl-D-alanine
alac-S	Cytosol	(S)-2-Acetolactate
alpro	Cytosol	S-Aminomethyldihydrolipoylprotein
amet	Cytosol	S-Adenosyl-L-methionine
ametam	Cytosol	S-Adenosylmethioninamine
amob	Cytosol	S-Adenosyl-4-methylthio-2-oxobutanoate
amopbut-L	Cytosol	2-Amino-3-oxo-4-phosphonooxybutyrate
amp	Cytosol	AMP
anth	Cytosol	Anthranilate
aps	Cytosol	Adenosine 5'-phosphosulfate
ara5p	Cytosol	D-Arabinose 5-phosphate
arg-L	Cytosol	L-Arginine

argsuc	Cytosol	N(omega)-(L-Arginino)succinate
asn-L	Cytosol	L-Asparagine
asp-L	Cytosol	L-Aspartate
aspsa	Cytosol	L-Aspartate 4-semialdehyde
atp	Cytosol	ATP
btn	Cytosol	Biotin
butacp	Cytosol	Butyryl-[acyl-carrier protein]
ca2	Extracellular	Calcium
ca2[e]	Cytosol	Calcium
cbasp	Cytosol	N-Carbamoyl-L-aspartate
cbl1	Cytosol	Cob(I)alamin
cbm	Cytosol	Carbamate
cbp	Cytosol	Carbamoyl phosphate
cd2	Extracellular	Cadmium
cd2[e]	Cytosol	Cadmium
cdlp	Cytosol	Cardiolipin
cdp	Cytosol	CDP
cdpdag	Cytosol	CDPdiacylglycerol
chor	Cytosol	Chorismate
cit	Extracellular	Citrate
cit[e]	Cytosol	Citrate
citr-L	Cytosol	L-Citrulline
ckdo	Cytosol	CMP-3-deoxy-D-manno-octulosonate
cl	Extracellular	Chloride
cl[e]	Cytosol	Chloride
cmp	Cytosol	CMP
cmpacna	Cytosol	CMP-N-acetylneuraminate
co1dam	Cytosol	Cob(I)yrinate a,c diamide
co2	Extracellular	CO2
co2[e]	Cytosol	CO2
co2dam	Cytosol	Cob(II)yrinate a,c diamide

coa	Cytosol	Coenzyme A
cobalt2	Extracellular	Co2+
cobalt2[e]	Cytosol	Co2+
cobamcoa	Cytosol	Cobamide coenzyme
cpppg3	Cytosol	Coproporphyrinogen III
creat	Cytosol	Creatine
crtn	Cytosol	Creatinine
ctp	Cytosol	CTP
cu2	Extracellular	Cu2+
cu2[e]	Cytosol	Cu2+
cys-L	Cytosol	L-Cysteine
cysam	Cytosol	Cysteamine
cysth-L	Cytosol	L-Cystathionine
dad-5	Cytosol	5'-Deoxyadenosine
dadp	Cytosol	dADP
damp	Cytosol	dAMP
dann	Cytosol	7,8-Diaminononanoate
datp	Cytosol	dATP
db4p	Cytosol	3,4-dihydroxy-2-butanone 4-phosphate
dcamp	Cytosol	N6-(1,2-Dicarboxyethyl)-AMP
dcdp	Cytosol	dCDP
dcmp	Cytosol	dCMP
dctp	Cytosol	dCTP
ddeacp	Cytosol	Dodecanoyl-[acyl-carrier protein]
decacp	Cytosol	Decanoyl-[acyl-carrier protein]
decdp	Cytosol	all-trans-Decaprenyl diphosphate
dgdp	Cytosol	dGDP
dgmp	Cytosol	dGMP
dgsn	Cytosol	Deoxyguanosine
dgtp	Cytosol	dGTP
dhap	Cytosol	Dihydroxyacetone phosphate

dhf	Cytosol	7,8-Dihydrofolate
dhlpro	Cytosol	Dihydrolipolprotein
dhna	Cytosol	1,4-Dihydroxy-2-naphthoate
dhor-S	Cytosol	(S)-Dihydroorotate
dhpt	Cytosol	Dihydropteroate
dmbzid	Cytosol	5,6-Dimethylbenzimidazole
dmlz	Cytosol	6,7-Dimethyl-8-(1-D-ribityl)lumazine
dmpp	Cytosol	Dimethylallyl diphosphate
dnad	Cytosol	Deamino-NAD+
dpcoa	Cytosol	Dephospho-CoA
dtbt	Cytosol	Dethiobiotin
dtdp	Cytosol	dTDP
dtdp6dm	Cytosol	dTDP-6-deoxy-L-mannose
dtdpddg	Cytosol	dTDP-4-dehydro-6-deoxy-D-glucose
dtdpddm	Cytosol	dTDP-4-dehydro-6-deoxy-L-mannose
dtdpglc	Cytosol	dTDPglucose
dtmp	Cytosol	dTMP
dttp	Cytosol	dTTP
dudp	Cytosol	dUDP
dump	Cytosol	dUMP
dutp	Cytosol	dUTP
dxyl5p	Cytosol	1-deoxy-D-xylulose 5-phosphate
e4p	Cytosol	D-Erythrose 4-phosphate
eig3p	Cytosol	D-erythro-1-(Imidazol-4-yl)glycerol 3-phosphate
f6p	Cytosol	D-Fructose 6-phosphate
fa1	Cytosol	Fatty acid (Iso-C14:0)
fa3	Cytosol	Fatty acid (Iso-C15:0)
fa4	Cytosol	Fatty acid (Anteiso-C15:0)
fa9	Cytosol	Fatty acid (Iso-C17:1)
fad	Cytosol	FAD
fadh2	Cytosol	FADH2

fdp	Cytosol	D-Fructose 1,6-bisphosphate
fdxo-4:2	Cytosol	ferrodoxin (oxidized form 4:2)
fdxr-4:2	Cytosol	ferrodoxin (reduced form 4:2)
fe2	Extracellular	Fe2+
fe2[e]	Extracellular	Fe2+
fe3[e]	Cytosol	Fe3+
fgam	Cytosol	N2-Formyl-N1-(5-phospho-D-ribosyl)glycinamide
ficytc	Cytosol	Ferricytochrome c
fmn	Cytosol	flavin mononucleotide
focytc	Cytosol	Ferrocytochrome c
fol	Cytosol	Folate
for	Extracellular	Formate
for[e]	Cytosol	Formate
fpram	Cytosol	2-(Formamido)-N1-(5-phospho-D-ribosyl)acetamidine
fprica	Cytosol	5-Formamido-1-(5-phospho-D-ribosyl)imidazole-4-carboxamide
frdp	Cytosol	Farnesyl diphosphate
fum	Extracellular	Fumarate
fum[e]	Cytosol	Fumarate
g15lac	Cytosol	D-Glucono-1,5-lactone
g1p	Cytosol	D-Glucose 1-phosphate
g3p	Cytosol	Glyceraldehyde 3-phosphate
g6p	Cytosol	D-Glucose 6-phosphate
gal1p	Cytosol	alpha-D-Galactose 1-phosphate
gam1p	Cytosol	D-Glucosamine 1-phosphate
gam6p	Cytosol	D-Glucosamine 6-phosphate
gar	Cytosol	N1-(5-Phospho-D-ribosyl)glycinamide
gcald	Cytosol	Glycolaldehyde
gdp	Cytosol	GDP
gdpddm	Cytosol	GDP-4-dehydro-6-deoxy-D-mannose
gdpfuc	Cytosol	GDP-L-fucose
gdpman	Cytosol	GDP-D-mannose

gdpofuc	Cytosol	GDP-4-oxo-L-fucose
gdptp	Cytosol	Guanosine 3'-diphosphate 5'-triphosphate
ggdp	Cytosol	Geranylgeranyl diphosphate
glc-D	Cytosol	D-Glucose
gln-L	Extracellular	L-Glutamine
gln-L[e]	Cytosol	L-Glutamine
glntrna	Cytosol	L-Glutaminyl-tRNA(Gln)
glu-D	Cytosol	D-Glutamate
glu-L	Cytosol	L-Glutamate
glu1sa	Cytosol	L-Glutamate 1-semialdehyde
glu5p	Cytosol	L-Glutamate 5-phosphate
glu5sa	Cytosol	L-Glutamate 5-semialdehyde
glutrna	Cytosol	L-Glutamyl-tRNA(Glu)
gly	Extracellular	Glycine
gly[e]	Cytosol	Glycine
glyc	Cytosol	Glycerol
glyc-R	Cytosol	(R)-Glycerate
glyc3p	Cytosol	sn-Glycerol 3-phosphate
glyclt	Cytosol	Glycolate
glycogen	Cytosol	glycogen
gmp	Cytosol	GMP
grdp	Cytosol	Geranyl diphosphate
gthox	Cytosol	Oxidized glutathione
gthrd	Cytosol	Reduced glutathione
gtp	Cytosol	GTP
gua	Cytosol	Guanine
h	Cytosol	H+
h2	Extracellular	H2
h2[e]	Cytosol	H2
h2mb4p	Cytosol	1-hydroxy-2-methyl-2-(E)-butenyl 4-diphosphate
h2o	Cytosol	H2O

h2o2	Extracellular	Hydrogen peroxide
h2o[e]	Cytosol	H2O
h2s	Extracellular	Hydrogen sulfide
h2s[e]	Extracellular	Hydrogen sulfide
h[e]	Cytosol	H+
hco3	Cytosol	Bicarbonate
hcys-L	Cytosol	L-Homocysteine
hdca	Cytosol	Hexadecanoate (n-C16:0)
hdcea	Cytosol	hexadecenoate (n-C16:1)
hdeacp	Cytosol	Hexadecanoyl-[acyl-carrier protein]
hepdp	Cytosol	all-trans-Heptaprenyl diphosphate
hexacp	Cytosol	Hexanoyl-[acyl-carrier protein]
hexdp	Cytosol	all-trans-Hexaprenyl diphosphate
hg0	Cytosol	Mercury (uncharged)
hg2	Cytosol	Mercury (charged +2)
hgbam	Cytosol	Hydrogenobyrinate a,c diamide
hgbyr	Cytosol	Hydrogenobyrinate
his-L	Cytosol	L-Histidine
hisp	Cytosol	L-Histidinol phosphate
histd	Cytosol	L-Histidinol
hmbil	Cytosol	Hydroxymethylbilane
hom-L	Cytosol	L-Homoserine
hpyr	Cytosol	Hydroxypyruvate
hxan	Cytosol	Hypoxanthine
iasp	Cytosol	Iminoaspartate
ibcoa	Cytosol	Isobutyryl-CoA
ichor	Cytosol	Isochorismate
icit	Cytosol	Isocitrate
ile-L	Extracellular	L-Isoleucine
ile-L[e]	Cytosol	L-Isoleucine
imacp	Cytosol	3-(Imidazol-4-yl)-2-oxopropyl phosphate

imp	Cytosol	IMP
ipdp	Cytosol	Isopentenyl diphosphate
ivcoa	Cytosol	Isovaleryl-CoA
k	Extracellular	K+
k[e]	Cytosol	K+
kdo	Cytosol	3-Deoxy-D-manno-2-octulosonate
kdo8p	Cytosol	3-Deoxy-D-manno-octulosonate 8-phosphate
lac-L	Extracellular	L-Lactate
lac-L[e]	Cytosol	L-Lactate
leu-D	Cytosol	D-Leucine
leu-L	Extracellular	L-Leucine
leu-L[e]	Cytosol	L-Leucine
lgt-S	Cytosol	(R)-S-Lactoylglutathione
lipid4	Cytosol	2,3,2'3'-Tetrakis(3-hydroxytetradecanoyl)-D-glucosaminyl-1,6-beta-D-glucosamine 1,4'-bisphosphate
lipidA	Cytosol	2,3-Bis(3-hydroxytetradecanoyl)-D-glucosaminyl-1,6-beta-D-2,3-bis(3-hydroxytetradecanoyl)-beta-D-glucosaminyl 1-phosphate
lipidAds	Cytosol	Lipid A Disaccharide
lipidX	Cytosol	2,3-Bis(3-hydroxytetradecanoyl)-beta-D-glucosaminyl 1-phosphate
lpro	Cytosol	Lipoylprotein
lys-L	Extracellular	L-Lysine
lys-L[e]	Cytosol	L-Lysine
mal-L	Extracellular	L-Malate
mal-L[e]	Cytosol	L-Malate
malacp	Cytosol	Malonyl-[acyl-carrier protein]
malcoa	Cytosol	Malonyl-CoA
male	Cytosol	Maleate
malm	Cytosol	Maleamate
man1p	Cytosol	D-Mannose 1-phosphate
man6p	Cytosol	D-Mannose 6-phosphate
met-L	Cytosol	L-Methionine
methf	Cytosol	5,10-Methenyltetrahydrofolate

mg2	Extracellular	Mg
mg2[e]	Cytosol	Mg
mlthf	Cytosol	5,10-Methylenetetrahydrofolate
mmcoa-R	Cytosol	(R)-Methylmalonyl-CoA
mmcoa-S	Cytosol	(S)-Methylmalonyl-CoA
mn2	Extracellular	Mn2+
mn2[e]	Cytosol	Mn2+
mobd	Extracellular	Molybdate
mobd[e]	Cytosol	Molybdate
mql7	Cytosol	Menaquinol 7
mqn7	Cytosol	Menaquinone 7
mqn8	Cytosol	Menaquinone 8
mthgxl	Cytosol	Methylglyoxal
myrt	Cytosol	Myristate; Fatty acid (n-C14:0) fa2
n2	Extracellular	N2
n2[e]	Cytosol	N2
na1	Extracellular	Sodium
na1[e]	Cytosol	Sodium
nac	Cytosol	Nicotinate
nad	Cytosol	Nicotinamide adenine dinucleotide
nadh	Cytosol	Nicotinamide adenine dinucleotide - reduced
nadp	Cytosol	Nicotinamide adenine dinucleotide phosphate
nadph	Cytosol	Nicotinamide adenine dinucleotide phosphate - reduced
ncam	Cytosol	Nicotinamide
nh3	Cytosol	Ammonia
nh4	Extracellular	Ammonium
nh4[e]	Cytosol	Ammonium
nh4oh	Cytosol	Ammonium hydroxide
ni2	Extracellular	Ni2+
ni2[e]	Cytosol	Ni2+
nicrnt	Cytosol	Nicotinate D-ribonucleotide

no2	Cytosol	Nitrite
nondp	Cytosol	all-trans-Nonaprenyl diphosphate
o2	Cytosol	O2
o2-	Cytosol	Superoxide
oaa	Cytosol	Oxaloacetate
ocdacp	Cytosol	Octadecanoyl-[acyl-carrier protein]
ocdca	Cytosol	octadecanoate (n-C18:0)
ocdcea	Cytosol	octadecenoate (n-C18:1)
octacp	Cytosol	Octanoyl-[acyl-carrier protein]
octdp	Cytosol	all-trans-Octaprenyl diphosphate
orn-L	Cytosol	L-Ornithine
orot	Cytosol	Orotate
orot5p	Cytosol	Orotidine 5'-phosphate
oxa	Extracellular	Oxalate
oxa[e]	Cytosol	Oxalate
pan4p	Cytosol	Pantetheine 4'-phosphate
pant-R	Cytosol	(R)-Pantoate
pap	Cytosol	Adenosine 3',5'-bisphosphate
paps	Cytosol	3'-Phosphoadenylyl sulfate
pendp	Cytosol	all-trans-Pentaprenyl diphosphate
pep	Cytosol	Phosphoenolpyruvate
pgly	Cytosol	Phosphatidylglycerol
pglyp	Cytosol	Phosphatidylglycerophosphate
phe-L	Cytosol	L-Phenylalanine
pheme	Cytosol	Protoheme
phom	Cytosol	O-Phospho-L-homoserine
phpyr	Cytosol	Phenylpyruvate
phthr	Cytosol	O-Phospho-4-hydroxy-L-threonine
pi	Extracellular	Phosphate
pi[e]	Cytosol	Phosphate
pmcoa	Cytosol	Pimeloyl-CoA

pnto-R	Cytosol	(R)-Pantothenate
polglu	Cytosol	Poly-gamma-D-glutamate
polypi	Cytosol	Polyphosphate
ppbng	Cytosol	Porphobilinogen
ppcoa	Cytosol	Propanoyl-CoA
pphn	Cytosol	Prephenate
ppi	Cytosol	Diphosphate
ppp9	Cytosol	Protoporphyrin
pppg9	Cytosol	Protoporphyrinogen IX
pppi	Cytosol	Inorganic triphosphate
pptg1	Cytosol	Peptidoglycan subunit
pram	Cytosol	5-Phospho-beta-D-ribosylamine
pran	Cytosol	N-(5-Phospho-D-ribosyl)anthranilate
prbamp	Cytosol	1-(5-Phosphoribosyl)-AMP
prbatp	Cytosol	1-(5-Phosphoribosyl)-ATP
pre3a	Cytosol	Precorrin 3 A
pre3b	Cytosol	Precorrin 3B
pre4	Cytosol	Precorrin 4
pre5	Cytosol	Precorrin 5
pre6a	Cytosol	Precorrin 6A
pre6b	Cytosol	Precorrin 6B
pre8	Cytosol	Precorrin 8
prfp	Cytosol	1-(5-Phosphoribosyl)-5-[(5-phosphoribosylamino)methylideneamino]imidazole-4-carboxamide
prlp	Cytosol	5-[(5-phospho-1-deoxyribulos-1-ylamino)methylideneamino]-1-(5-phosphoribosyl)imidazole-4-carboxamide
pro-L	Extracellular	L-Proline
pro-L[e]	Cytosol	L-Proline
prpp	Cytosol	5-Phospho-alpha-D-ribose 1-diphosphate
ps	Cytosol	Phosphatidylserine
pser-L	Cytosol	O-Phospho-L-serine
ptrc	Cytosol	Putrescine

ptth	Cytosol	Pantetheine
pyr	Cytosol	Pyruvate
quln	Cytosol	Quinolinate
r5p	Cytosol	alpha-D-Ribose 5-phosphate
rdmbzi	Cytosol	N1-(alpha-D-ribosyl)-5,6-dimethylbenzimidazole
rhcys	Cytosol	S-Ribosyl-L-homocysteine
rib-D	Cytosol	D-Ribose
ribflv	Cytosol	Riboflavin
ru5p-D	Cytosol	D-Ribulose 5-phosphate
s	Cytosol	Sulfur
s7p	Extracellular	Sedoheptulose 7-phosphate
s[e]	Cytosol	Sulfur
sbt6p	Cytosol	D-Sorbitol 6-phosphate
sbzcoa	Cytosol	O-Succinylbenzoyl-CoA
ser-L	Cytosol	L-Serine
shcl	Cytosol	Sirohydrochlorin
sheme	Cytosol	Siroheme
skm	Cytosol	Shikimate
skm5p	Cytosol	Shikimate 5-phosphate
sl26da	Cytosol	N-Succinyl-LL-2,6-diaminoheptanedioate
sl2a6o	Cytosol	N-Succinyl-2-L-amino-6-oxoheptanedioate
so3	Cytosol	Sulfite
so4	Extracellular	Sulfate
so4[e]	Cytosol	Sulfate
spmd	Cytosol	Spermidine
srb1p	Cytosol	Sorbose 1-phosphate
srch	Extracellular	Sirochlorin
ss[e]	Cytosol	Disulfide
ssaltpp	Cytosol	Succinate semialdehyde-thiamin diphosphate anion
sucbz	Cytosol	o-Succinylbenzoate
succ	Extracellular	Succinate

succ[e]	Cytosol	Succinate
succoa	Cytosol	Succinyl-CoA
tdeacp	Cytosol	Tetradecanoyl-[acyl-carrier protein]
thdp	Cytosol	2,3,4,5-Tetrahydrodipicolinate
thf	Cytosol	5,6,7,8-Tetrahydrofolate
thmmp	Cytosol	Thiamin monophosphate
thmpp	Cytosol	Thiamine diphosphate
thr-L	Cytosol	L-Threonine
thr-LA	Cytosol	L-Allo-threonine
thymd	Cytosol	Thymidine
trdox	Cytosol	Oxidized thioredoxin
trdrd	Cytosol	Reduced thioredoxin
tre	Cytosol	Trehalose
tre6p	Cytosol	alpha,alpha'-Trehalose 6-phosphate
trnagln	Cytosol	tRNA(Gln)
trnaglu	Cytosol	tRNA (Glu)
trp-L	Cytosol	L-Tryptophan
tyr-L	Cytosol	L-Tyrosine
u23ga	Cytosol	UDP-2,3-bis(3-hydroxytetradecanoyl)glucosamine
u3aga	Cytosol	UDP-3-O-(3-hydroxytetradecanoyl)-N-acetylglucosamine
u3hga	Cytosol	UDP-3-O-(3-hydroxytetradecanoyl)-D-glucosamine
uaagmda	Cytosol	Undecaprenyl-diphospho-N-acetylmuramoyl-(N-acetylglucosamine)-L-alanyl-D-glutamyl-meso-2,6-diaminopimeloyl-D-alanyl-D-alanine
uaagtmda	Cytosol	Undecaprenyl-diphospho-N-acetylmuramoyl-(N-acetylglucosamine)-L-alanyl-D-glutaminyl-meso-2,6-diaminopimeloyl-D-alanyl-D-alanine
uaagtmdga	Cytosol	Undecaprenyl-diphospho-N-acetylmuramoyl-(N-acetylglucosamine)-L-alanyl-D-glutaminyl-meso-2,6-diaminopimeloyl-(glycyl)5-D-alanyl-D-alanine
uaccg	Cytosol	UDP-N-acetyl-3-O-(1-carboxyvinyl)-D-glucosamine
uacgam	Cytosol	UDP-N-acetyl-D-glucosamine
uacmam	Cytosol	UDP-N-acetyl-D-mannosamine
uagmda	Cytosol	Undecaprenyl-diphospho-N-acetylmuramoyl-L-alanyl-D-glutamyl-meso-2,6-diaminopimeloyl-D-

		alanyl-D-alanine
uama	Cytosol	UDP-N-acetylmuramoyl-L-alanine
uamag	Cytosol	UDP-N-acetylmuramoyl-L-alanyl-D-glutamate
uamr	Cytosol	UDP-N-acetylmuramate
udcp	Cytosol	Undecaprenol
udcpdp	Cytosol	Undecaprenyl diphosphate
udcpp	Cytosol	Undecaprenyl phosphate
udp	Cytosol	UDP
udpg	Cytosol	UDPglucose
udpgal	Cytosol	UDPgalactose
udpglcur	Cytosol	UDP-D-glucuronate
ugmd	Cytosol	UDP-N-acetylmuramoyl-L-alanyl-D-gamma-glutamyl-meso-2,6-diaminopimelate
ugmda	Cytosol	UDP-N-acetylmuramoyl-L-alanyl-D-glutamyl-meso-2,6-diaminopimeloyl-D-alanyl-D-alanine
ump	Cytosol	UMP
unknown1	Cytosol	Unknown Product
uppg3	Cytosol	Uroporphyrinogen III
ura	Extracellular	Uracil
ura[e]	Cytosol	Uracil
utp	Cytosol	UTP
val-L	Extracellular	L-Valine
val-L[e]	Cytosol	L-Valine
xmp	Cytosol	Xanthosine 5'-phosphate
xu5p-D	Cytosol	D-Xylulose 5-phosphate
zn2	Extracellular	Zinc

Table A.3: Reporter metabolites for a comparison between the most efficient phenotype in each of the clusters depicted in Figure 5.1. Only the top ten metabolites are shown. E,g, "1-2" refers to the reporter metabolites determined for the comparison between clusters 1 and 2. Abbreviations as given in Table A.2.

1-2	1-3	1-4	1-5	1-6	1-7	1-8	1-9	1-10
Metabolite	Metabolite	Metabolite	Metabolite	Metabolite	Metabolite	Metabolite	Metabolite	Metabolite
h	coa	h	h	h	h	h	h	h
akg	h	pi	coa	nh4	akg	coa	akg	coa
h2o	co2	pyr	akg	h2o	glu-L	h2o	coa	akg
nh4	akg	akg	glu-L	akg	nadp	akg	glu-L	pi
glu-L	succ	glu-L	succ	glu-L	nadph	nh4	co2	h2o
nad	succoa	h[e]	nadp	nadp	h[e]	pi	nadp	adp
nadh	accoa	h2o	nadph	nadph	h2o	glu-L	nadph	atp
pi	fdxo-4:2	nadp	accoa	fdxo-4:2	coa	accoa	fdxo-4:2	nh4
co2	fdxr-4:2	nadph	h[e]	fdxr-4:2	accoa	nadp	fdxr-4:2	glu-L
coa	mql7	mql7	mql7	h[e]	for	nadph	h[e]	fdxo-4:2

1-11	1-12	2-3	2-4	2-5	2-6	2-7	2-8	2-9
Metabolite	Metabolite	Metabolite	Metabolite	Metabolite	Metabolite	Metabolite	Metabolite	Metabolite
succ	mql7	h	h	h	h	h	h	h
mql7	mqn7	pi	pi	coa	coa	coa	coa	pi
mqn7	fum	h2o	atp	pi	akg	akg	akg	adp
fum	succ	adp	h2o	adp	co2	pi	adp	atp
h	h	atp	coa	atp	nad	nad	atp	glu-L
nadp	glu-L	glu-L	pyr	akg	nadh	nadh	pi	gln-L
nadph	h2o	nh4	akg	accoa	glu-L	co2	accoa	h2o
coa	nadp	akg	h[e]	co2	gln-L	fdxo-4:2	co2	nh4
accoa	nadph	succ	co2	nad	h[e]	fdxr-4:2	succoa	coa

h[e]	h[e]	nadp	nad	nadh	mql7	adp	glu-L	accoa

2-10 Metabolite	2-11 Metabolite	2-12 Metabolite	3-4 Metabolite	3-5 Metabolite	3-6 Metabolite	3-7 Metabolite	3-8 Metabolite	3-9 Metabolite
h	succ	mql7	h	h	coa	coa	h	coa
coa	mql7	mqn7	pi	akg	h	h	akg	h
accoa	mqn7	h	coa	coa	akg	akg	h2o	accoa
h[e]	fum	fum	akg	co2	h2o	accoa	nad	akg
mql7	h	succ	pyr	nad	nh4	nad	nadh	glu-L
mqn7	coa	pi	atp	nadh	pi	nadh	coa	h2o
succ	nadp	glu-L	h2o	accoa	accoa	co2	nh4	pyr
pyr	nadph	adp	accoa	h2o	succoa	succ	co2	nad
akg	akg	atp	co2	glu-L	nad	succoa	accoa	nadh
nad	pi	h2o	succoa	pyr	nadh	glu-L	glu-L	actp

3-10 Metabolite	3-11 Metabolite	3-12 Metabolite	4-5 Metabolite	4-6 Metabolite	4-7 Metabolite	4-8 Metabolite	4-9 Metabolite	4-10 Metabolite
h	h	h	pi	pi	h	pi	h	h
h2o	co2	coa	h	h	pi	h	pi	pi
nh4	coa	akg	atp	h2o	pyr	atp	coa	atp
pi	nadp	glu-L	coa	atp	fum	h2o	pyr	coa
glu-L	nadph	nad	pyr	pep	succ	succ	co2	adp
akg	nad	nadh	actp	pyr	amp	adp	akg	h2o
adp	nadh	co2	adp	amp	atp	pep	succoa	succoa
atp	accoa	h2o	amp	h2	pep	coa	amp	h[e]
accoa	pyr	adp	pep	nh4	pi[e]	pyr	atp	pyr
coa	akg	atp	pi[e]	pi[e]	h[e]	h[e]	pep	nh4

4-11 Metabolite	4-12 Metabolite	5-6 Metabolite	5-7 Metabolite	5-8 Metabolite	5-9 Metabolite	5-10 Metabolite	5-11 Metabolite	5-12 Metabolite
h	h	pi	succ	h	coa	h	h	h

pi	pi	adp	coa	h2o	succoa	pi	nadp	coa
nadp	pyr	atp	fum	succ	co2	h2o	nadph	glu-L
nadph	glu-L	coa	actp	fum	akg	coa	akg	adp
atp	h[e]	actp	adp	h2	h	adp	nad	atp
h2o	atp	h2	atp	nh4	accoa	atp	nadh	pi
h[e]	h2o	nh4	pi	pi	actp	nh4	glu-L	accoa
coa	mql7	h2o	accoa	nad	adp	fdxo-4:2	h2o	succ
akg	mqn7	h	mql7	nadh	atp	fdxr-4:2	h[e]	h[e]
nad	amp	accoa	mqn7	mql7	pi	co2	for	mql7

6-7 Metabolite	6-8 Metabolite	6-9 Metabolite	6-10 Metabolite	6-11 Metabolite	6-12 Metabolite	7-8 Metabolite	7-9 Metabolite	7-10 Metabolite
fum	succ	h	h	h	h	pi	coa	h
succ	coa	coa	coa	nadp	glu-L	adp	co2	pi
h2o	h	fdxo-4:2	adp	nadph	h2o	atp	akg	adp
h2	fum	fdxr-4:2	atp	h2o	pi	h	fum	atp
nh4	actp	co2	pi	nh4	fdxo-4:2	coa	succ	coa
pi	adp	akg	succoa	pi	fdxr-4:2	actp	succoa	succ
h	atp	succoa	co2	akg	h[e]	h2	h	succoa
mql7	h2	h2o	akg	coa	adp	nh4	mql7	h2o
mqn7	pi	h2	accoa	adp	atp	h2o	mqn7	nh4
fdxo-4:2	accoa	nh4	actp	atp	mql7	accoa	fdxo-4:2	mql7

7-11 Metabolite	7-12 Metabolite	8-9 Metabolite	8-10 Metabolite	8-11 Metabolite	8-12 Metabolite	9-10 Metabolite	9-11 Metabolite	9-12 Metabolite
succ	fum	coa	h	h	succ	pi	h	h
fum	succ	pi	mql7	succ	fum	h	coa	coa
mql7	mql7	h	mqn7	fum	mql7	adp	akg	akg
mqn7	mqn7	adp	coa	mql7	mqn7	atp	nadp	glu-L
h	h	atp	co2	mqn7	h	h2o	nadph	co2
nadp	glu-L	succ	nad	nadp	pi	nh4	co2	fdxo-4:2

nadph	h[e]	succoa	nadh	nadph	coa	coa	nad	fdxr-4:2
coa	coa	nad	akg	h2o	adp	actp	nadh	h[e]
akg	accoa	nadh	adp	nad	atp	ctp	succoa	accoa
nad	akg	fdxo-4:2	atp	nadh	glu-L	h2	accoa	nad

10-11 Metabolite	10-12 Metabolite	11-12 Metabolite
h	h	h
h2o	pi	nadp
akg	coa	nadph
nadp	adp	glu-L
nadph	atp	coa
nh4	glu-L	h2o
co2	h2o	nad
glu-L	akg	nadh
coa	fdxo-4:2	akg
pi	fdxr-4:2	adp

References

1. Mahadevan R, Bond DR, Butler JE, Esteve-Nunez A, Coppi MV, Palsson BO, Schulling CH, Lovley DR: **Characterization of metabolism in the Fe(III)-reducing organism Geobacter sulfurreducens by constraint-based modeling.** *Appl Environ Microbiol* 2006, **72:**1558-1568.